5-2017

Fabrication and Characterization of Silicon Carbide Epoxy Composites

James Townsend
Clemson University, jatowns@clemson.edu

FABRICATION AND CHARACTERIZATION OF SILICON CARBIDE EPOXY COMPOSITES

A Dissertation
Presented to
the Graduate School of
Clemson University

In Partial Fulfilment
of the Requirement of the Degree
Doctor of Philosophy
Materials Science and Engineering

---

by
James Townsend
May 2017

Accepted by:
Dr. Igor Luzinov, Committee Chair
Dr. Olin Mefford
Dr. Marian Kennedy
Dr. Christopher Kitchens

ABSTRACT

Nanoscale fillers can significantly enhance the performance of composites by increasing the extent of filler-to-matrix interaction. Thus far, the embedding of nanomaterials into composites has been achieved, but the directional arrangement has proved to be a challenging task. Even with advances in *in-situ* and shear stress induced orientation, these methods are both difficult to control and unreliable. Therefore, the fabrication of nanomaterials with an ability to orient along a magnetic field is a promising pathway to create highly controllable composite systems with precisely designed characteristics. To this end, the goal of this dissertation is to develop magnetically active nanoscale whiskers and study the effect of the whiskers orientation in a polymer matrix on the nanocomposite's behavior.

Namely, we report the surface modification of silicon carbide whiskers (SiCWs) with magnetic nanoparticles and fabrication of SiC/epoxy composite materials. The magnetic nanoparticles attachment to the SiCWs was accomplished using polyelectrolyte polymer-to-polymer complexation. The "grafting to" and adsorption techniques were used to attach the polyelectrolytes to the surface of the SiCWs and magnetic nanoparticles. The anchored polyelectrolytes were polyacrylic acid (PAA) and poly(2-vinylpyridine) (P2VP).

Next, the SiC/epoxy composites incorporating randomly oriented and magnetically oriented whiskers were fabricated. The formation of the composite was studied to determine the influence of the whiskers' surface composition on the epoxy curing reaction. After curing, the composites' thermal and thermo-mechanical properties

were studied. These properties were related to the dispersion and orientation of the fillers in the composite samples. The obtained results indicated that the thermal and thermo-mechanical properties could be improved by orienting magnetically-active SiCWs inside the matrix.

Silanization, “grafting to”, adsorption, and complexation were used to modify the surface of SiCWs to further investigate the epoxy nanocomposite system. The process of composites formation was studied to evaluate the effects of the surface modification on the epoxy curing reaction. The obtained composites were tested and analyzed to assess their thermal and thermo-mechanical properties. These properties were related to the dispersion and surface chemical composition of the fillers in the nanocomposites. It was determined that magnetically modified SiCWs have lower ability for interfacial stress transfer in the composite systems under consideration.

The final portion of this work was focused on reinforcing the magnetic layer of the SiCWs. This was accomplished by structurally toughening the magnetic layer with poly(glycidyl methacrylate) (PGMA) layer. As a result, the thermal and mechanical properties of the magnetic composite system were improved significantly.

DEDICATION

I dedicate this dissertation to my parents Jack and Helen Townsend. They have always believed in me and pushed me to become the best version of myself. Their love has always been the backbone of my success.

Thank you for your sacrifices and compassion throughout this journey, I love you more than words can say.

I also dedicate this dissertation to my brothers Bear, Light, and Colin.

Without you, I would be lost in this world.

ACKNOWLEDGMENTS

First, I would like to acknowledge my advisor, Dr. Igor Luzinov, for giving me this opportunity and for his mentorship. His patience, appreciation, empathy, support, and laughter provided me with strength throughout my time here at Clemson University. I will always remember his wise words.

Thank you to Drs. O. Thompson Mefford, Marian Kennedy, and Christopher Kitchens for agreeing to serve on my committee. I am grateful for the time and effort they have put into me and my research.

In addition, I am most appreciative of the time Dr. Ruslan Burtovyy has spent mentoring me throughout these five years. I greatly appreciate his patience and helpful suggestions with my research and life.

A debt of gratitude is owed to my friends Dr. Bradley Schultz and Benoit Faugas. We have made some great memories and will make even more to come. *Thank you for making these some of the best years of my life.*

My friends and group members, Michael Seeber, Yuri Galabura, James Giammarco, Fehime Vatansever, Tugba Demir, Anna Paola Soliani, Mykhaylo Savchak, Nickolay Borodinov**,** and Liying Wei, are acknowledged for their support and encouragement. These years would have been dull without them.

I would also like to acknowledge Dr. Yu Gu and Pavel Aprelev for their guidance and friendship. A special thanks to Dr. Kornev and Pavel for helping me with magnetic measurements and improving my understanding of magnetic concepts.

I owe my Sundays, and a part of my happiness here, to Mr. Bob Bowen. *Thank you for your kindness and laughter.*

In kind, the Drs. Deborah and Gary Lickfield were very influential in my decision to come back to Clemson after the death of my brother. *Thank you for all the great memories, kindness, and conversations.*

A special thanks goes out to Ms. Kimberly Ivey for the support and affection she has shown me throughout my years. She has always been there for me when I needed a pick me up or a conversation. *Thank you for all your mentorship and creativity.*

Dr. Michael Ellison has also been a great friend and mentor. *I deeply appreciate those days out on the farm and your kindness.*

I also would like to thank Dr. Taghi Darroudi, Mr. Donald Mulwee, and Mr. Dayton Cash for their help at the Electron Microscopy Laboratory.

I thank everyone from Materials Science and Engineering from Clemson University for making this a memorable experience.

And most importantly, I am very thankful for all my friends and family who have been there to support, love, and encourage me throughout my life.

TABLE OF CONTENTS

Page

LIST OF FIGURES

TABLES

CHAPTER ONE

INTRODUCTION

In comparison to metals, ceramics, and polymers, composite materials have not been fabricated and studied nearly as long[1-2]. Nevertheless, nowadays composites are widely used in the aerospace, energy, and transportation industries due to an increased demand for greater strength, stiffness, and fatigue resistance per weight of manufactured components[1].

It is recognized that composites with nanoscale fillers can drive the performance of emerging and traditional materials to new heights by increasing the extent of the filler-to-matrix interaction[3] in comparison with traditionally used micron-scale fillers. Thus far, the embedding of nanomaterials into composites has been achieved, but directional arrangement has proved to be a challenging task[4]. Despite the advances with *in-situ* and shear induced orientation methods[4], the alignment of nanoparticulates is difficult to control and unreliable, hampering nanocomposite improvements. Thus, the implementation of nanomaterials with the ability of being oriented along magnetic fields can create a highly controllable system with precisely designed properties.

To this end, the goal of the work reported in this dissertation is to develop magnetically active nanoscale whiskers and study the effect of whiskers' orientation in a polymer matrix on nanocomposite's behavior. The work was conducted as follows. First, the methodology for the preparation of magnetically active silicon carbide whisker (SiCW) nanofillers was developed. Next, their magnetic orientation in a polymer matrix

was studied. Then, nanocomposite materials were fabricated and their structure-property relationships were investigated.

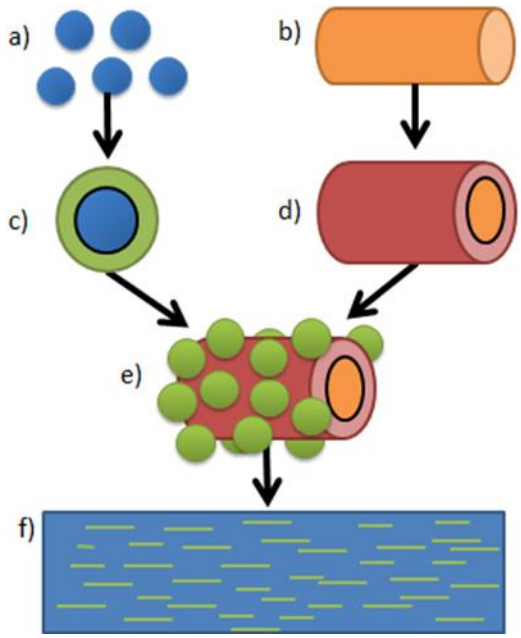

Figure 1.1: Diagram representation of the approach employed by this project: a) and b) the selection and synthesis of nanoparticles and SiCWs; c) and d) surface modification of the nanomaterials; e) the attachment of the nanoparticles to the whiskers; f) fabrication of composites with oriented nanofillers

Specifically, Figure 1.1 shows the workflow for the fabrication of the composite materials. Figure 1.1a and Figure 1.1b represent the synthesis and selection of the nickel nanoparticles (NiNPs), iron oxide nanoparticles (MagNPs), and SiCWs. Figure 1.1c and Figure 1.1d represent the modification of the nanomaterials to achieve preferable interactions between them. Figure 1.1e illustrates the functionalization of the modified SiCWs through mixing with modified magnetic nanoparticles to create magnetically modified SiCWs. Figure 1.1f depicts the fabrication of the magnetically oriented nanocomposites. At each step, the morphology, structure, and properties of the materials were characterized using transmission electron microscopy (TEM), scanning electron

microscopy (SEM), thermal gravimetric analysis (TGA), differential scanning calorimetry (DSC), dynamic mechanical analysis (DMA), and Fourier transform infrared spectroscopy (FTIR).

This dissertation is structured as follows:

- **Chapter 2** is a literature review of the materials, their properties, and methods used to modify the surface of the SiCWs and fabricate nanocomposite materials.
- **Chapter 3** describes the surface modification of SiCWs, NiNPs, and model nickel and silica surfaces. Additionally, this chapter includes the fabrication and study of the SiCWs modified with NiNPs (NiSiCWs) by polymer-polymer complexation.
- **Chapter 4** focuses on the surface modification of MagNPs. Furthermore, this chapter discusses the fabrication and study of SiCWs modified with MagNPs (MagSiCWs) by polymer-polymer complexation.
- **Chapter 5** describes the orientation of MagSiCWs in a magnetic field during the curing of the epoxy matrix. It includes studies of the curing process of the neat epoxy.
- **Chapter 6** is devoted to the influence of the MagSiCWs on the formation of the epoxy cross-linked network and the effect of MagSiCWs on the properties of the epoxy nanocomposite. This chapter also discusses methodologies applied to achieve the magnetic orientation of the MagSiCWs and the impact of MagSiCWs orientation on the composite's properties.
- **Chapter 7** focuses on the modification of the SiC-epoxy interfacial region in the composite materials. Specifically, hydroxyl functional groups, epoxy silane,

poly(2-vinylpyridine) (P2VP), and polyacrylic acid (PAA) were used to modify the surface of the SiCWs, which were later dispersed into the epoxy matrix. Thus, this chapter describes the effect of each surface modification on the formation and properties of the nanocomposites.

- **Chapter 8** concentrates on the reinforcement of the MagSiCWs' magnetic nanoparticle layer with poly(glycidyl methacrylate) (PGMA). Specifically, the PGMA reinforcement is used to increase the rigidity of the interphase to create more thermally and mechanically sound composite material.
- **Chapter 9** concludes this work by summarizing the key findings in course of this study**.**
- **Chapter 10** briefly outlines possible future work.

References

1. Chawla, K. K., *Composite materials. Science and engineering*. 3rd ed.; Springer Science: New York, 2012.

2. Plueddemann, E. P., *Interfaces in polymer matrix composites,*. Composite materials, Academic Press: New York, 1974; Vol. 6, p 294.

3. Hull, D.; Clyne, T. W., *An introduction to composite materials*. 2nd ed.; Cambridge Univeristy Press: Cambridge, 1996.

4. Keledi, G.; Hari, J.; Pukanszky, B., Polymer nanocomposites: structure, interaction, and functionality. *Nanoscale* **2012,** *4* (6), 1919-38.

CHAPTER TWO

LITERATURE REVIEW

This chapter covers the main scientific topics discussed within this dissertation. The background is broken into four major sections. The first section (Section 2.1) presents an overview of epoxy nanocomposite materials. Next, Section 2.2 contains principles of surface modification of nanomaterials. Then, the fabrication of composites with oriented fillers are presented in Section 2.3. Finally, Section 2.4 contains a concise description of nanocomposite materials' properties.

2.1: Epoxy Nanocomposite Materials

In general, a composite can be defined as a phase-separated material with characteristics defined by the combination of the characteristics of the individual components[1]. Composite materials is not a new concept. Nature has many examples of composite structures[2-4]. In the search for stronger and lighter materials, various structures resembling natural composites have been used to create cross-ply laminates, particulate dispersed, and fiber-reinforced composite materials[5]. Modern history denotes the first significant use of composites occurring during World War II that was aimed to decrease the weight of planes and extend flight distance. Nowadays, macro-scale composites are the backbone of the commercial aerospace industry. Specifically, in comparison to their aluminum counterparts, continuous carbon fiber composites deliver savings in weight and gains in strength[1]. Recently, new types of advanced composites, such as nanocomposites, biocomposites, self-reinforced composites, and self-healing composites, have been emerging[1].

Nanocomposite is defined as a composite material with one component that has at least one dimension in the nanometer range[1]. In general, these composites are comprised of a nanofiller (nanofibers, nanowhiskers, nanoplatelets, or nanoparticles) dispersed into a polymeric, metallic, or ceramic matrix. The polymer matrix is more common[6-8]. The first nanocomposites produced industrially were polymer nanoclay materials[9-11]. Chemically, these clays are composed of layered magnesium aluminum silicates that have a thickness of 1 nm and width ranging from 70 nm to 150 nm and are typically used at 2–3 wt. % within the matrix[1]. These clays are not easily dispersible into a non-polar polymer matrix. Thus, surface modification was used to create better surface interactions between the polymers and the nanoclays. In general, from carbon nanotubes to nanoscale rubber toughening particulates, the dispersibility is a very important factor for the nanocomposite industry. As a result, the chemical functionalization of nanofillers' surfaces is an active area of research for the nanocomposites[12-14].

2.1.1: Epoxy Thermoset Resins

In general, polymer chains in thermosetting matrices are connected into networked structure[15] (Figure 2.1). Of all the thermosetting polymers for composite technologies, epoxies are one of the most versatile and widely used[16].

The epoxy functional group, also known as an oxirane, is a three-member cyclic ether ring[17]. It is shown in Figure 2.2 as the group attached to R_1. This cyclic ether behaves differently from other cyclic ethers, like tetrahydrofuran (THF), due to the high strain within the three-member ring[17]. When epoxy is polymerized, no reactant

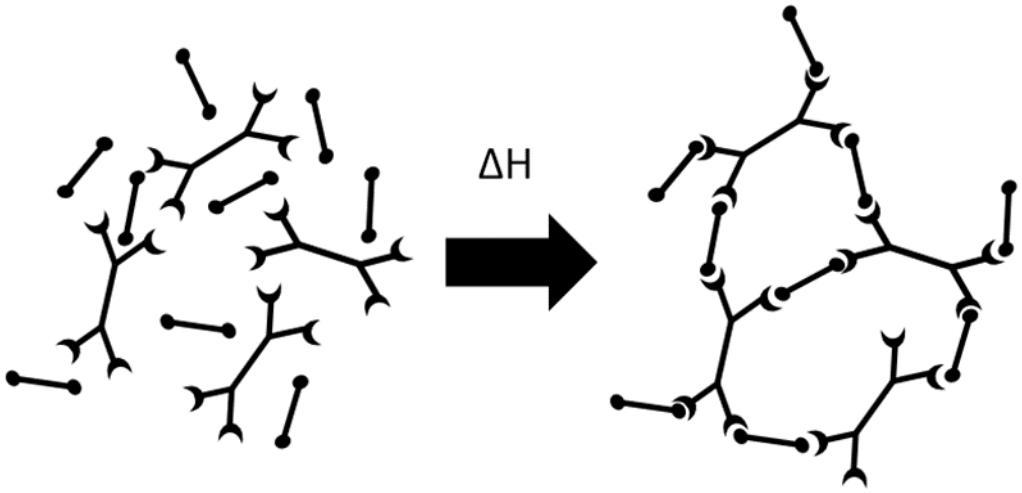

Figure 2.1: Conceptual diagram of the thermoset formation.

byproducts are formed (Figure 2.2). This is very beneficial for the composite system, as the presence of reactant byproducts may cause degradation of material's properties[18]. Additionally, the epoxy group can react with a large number of functional groups[19]. For instance, Figure 2.2 shows the reaction of the epoxy with a hydroxyl group and carboxylic acid. The reaction results in the opening of the epoxy ring producing an ether or ester linkage[17].

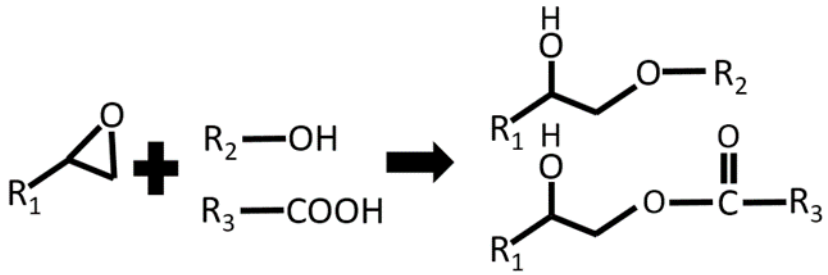

Figure 2.2: The schematic representation of the reaction of the epoxy functional group with hydroxyl and carboxylic functional groups.

In this work Araldite 6005 diglycidyl ether of bisphenol A (DGEBA) (Figure 2.3) is used as an epoxy material. It is a liquid resin modified with mono-functional reactive

diluents[19]. This epoxy resin is one of the most used commercially. It has good moisture resistance, lower shrinkage during curing (2–3 %), and a higher thermal stability than

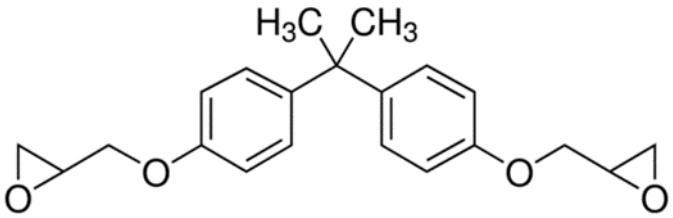

Figure 2.3: The chemical structure of DGEBA.

many other thermosetting resins[1].

The anhydride curing agent used in this work is one of the most commercially used reactants for the fabrication of epoxy based composite materials[20]. We chose to use dodecyl succinic anhydride (DDSA) (Figure 2.4) as a hardener system to keep the viscosity of the resin low. DDSA is used in many industrial applications, and the properties of epoxy systems cured with DDSA are well known[21-22].

2.1.2: Silicon Carbide Whiskers

For this research, SiCWs were selected to be high aspect ratio reinforcing agents with an easily modifiable surface. The modification is designed to increase surface interactions and modify the whiskers with magnetic particulates for the purpose of orientating them within the matrix. Several experimental procedures have been published

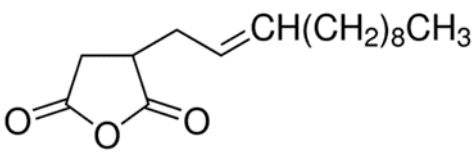

Figure 2.4: The chemical structure of DDSA.

to create magnetic whiskers, rods, and fibers[13, 23-28]. In this work, the attachment of magnetic nanoparticles was chosen as a route to make the SiCWs magnetically active.

The attached magnetic nanoparticles can be used to align the nanofillers within the matrix using magnetic field. In conventional composites, the designed directionality of the fillers has improved the specific strength and reduced the cost of many components used in the aerospace, energy, and transportation industries[1, 5]. Hence, the designed orientation of nanofillers is valuable for tailoring nanocomposite properties and advancement of the nanocomposite industry. Thus, the magnetic orientation of SiCWs modified with magnetic nanoparticles has been proposed as a route to create highly ordered discontinuous (high aspect ratio) nanofillers within a composite matrix.

Research to diversify the application base for SiC nanostructures started in the 1990s[29]. The first major interest was in enhancing the luminescence efficiency of porous silicon carbide fabricated using electrochemical etching[29]. Since then, various types of silicon carbide nanomaterials have been produced. SiC nanoparticles and SiC nanocrystals are mainly synthesized using vapor phase and solution-based reactions[29]. SiC nanowires and nanofibers are primarily synthesized by vapor-solid growth and vapor-liquid-solid growth with the assistance of a metal catalyst[29]. However, as this technology has progressed, the industrial manufacturing of SiCWs has moved more toward increased production with less control over the size and structure. For instance, this research used industrially produced Silar SC-9M SiCWs. They are a proprietary material from the Advanced Composite Materials LLC.[30]. Typical properties of SiCWs are outlined in Table 2.1.

Table 2.1: Typical properties of SiCWs[31-33].

Density (g/cm^3)	Thermal conductivity (W/cmK)	Young's modulus (GPa)
3.21	3.2–4.9	442–448

Silar SC-9M SiCWs are described as very high modulus rigid rods[30]. A whisker is a high aspect ratio material formed in a single crystal of ceramic or metal with no interacting grain boundaries within the material's structure[34]. In general, today's SiCWs are synthesized by either microwave heating of silica sol and activated carbon, or by the methods relying on vapor-to-liquid-to-solid growth mechanisms[35,36-43]. Currently, industrially inexpensive and renewable sources, like rice hulls, are often used to manufacture SiCWs[34]. Using this process, 80–90 % of the material is produced as whiskers. The whiskers contain alpha, beta, and mixed alpha and beta phases with impurities of 0.1 wt. % oxygen; 0.1–0.8 wt. % of Mn Mg, Fe, and Al; and 100–1,000 ppm of Cr, K, Cu, Ni, and Na [34]. Additionally, the SiCWs are stable up to 1800 ^oC[34].

SiCWs, like the Silar SC-9M, have already being used in industrial applications to improve the thermo-mechanical properties of composites. For instance, there have been 15 granted patents by the Advanced Composite Materials Corporation on the usage of SiCWs. The applications of these patents range from laminated hybrid composites to electromagnetic radiation absorption[34, 44-48].

2.1.3: Nickel Nanoparticles

Ferromagnetic materials are being extensively incorporated into nanocomposite films, gels, and capsules[49]. These materials are used in drug delivery, medical diagnosis, magnetic recording, conductive paints, and stimuli responsive magnetic materials[49-53].

Additionally, there is an increasing demand for materials with greater strength, thermal resistance, and magnetic responsiveness. Of the ferromagnetic materials, nickel is especially suited for use in these magneto-responsive materials due to its conductivity, ferromagnetism, high Curie temperature, thermal stability, strength, and simple procedures for the synthesis of NiNPs[54]. The combination of these properties makes NiNPs an excellent choice for industrial ferromagnetic nanocomposites[55]. Some of NiNPs' properties are listed in Table 2.2.

Table 2.2: Material properties of NiNPs[56-60].

Density (g/cm^3)	Saturation magnetization (emu/g)	Remnant magnetization (emu/g)	Coercivity (Oe)
~8.90	20–55	3–7	40–100

NiNPs have been synthesized by ball milling, electrodeposition, thermal decomposition, ligand stabilized solution-phase precipitation, decomposition of organometallic precursors, chemical vapor deposition (CVD), and liquid phase reduction[61-65]. Except for the liquid phase reduction, the synthetic procedures are cumbersome, time consuming, and requiring excessive effort. On contrary, for instance, hydrazine reduction, in its simplest form, takes just four chemicals: a stabilizer, reducing agent, nickel salt, and solvent[66]. There are several types of variations with ligand stabilizers, steric stabilizers, nucleating agents, and many other additives. However, the base four components provide a sufficient foundation to synthesize the nanoparticles. Hence, the simplicity of the reduction process gives plenty of room for control and variations to tune the desired particle shape and size.

2.1.4: Iron Oxide Nanoparticles

Iron oxide particles are mostly comprised of magnetite, maghemite, hematite, and wüstite phases[67-68], which relate to different crystal structures and/or ratios of Fe to O in the lattices[67-68]. These iron oxides are most notably known for the roles they play in geological and biological sciences[69-73]. Mankind has proven iron oxides to be invaluable, with applications ranging from pigments that decorate cave walls to the development of steel processing[68]. Today, their properties and economic viability make them ideal for a variety of traditional and emerging technologies[74].

This research have used a mixture of iron oxide nanoparticles from US Research Nanomaterials, Inc. The iron oxide mixture is mostly maghemite, denoted by the prevalent reddish color in the colloidal dispersions[68]. It is known as a γ-Fe_2O_3 having a Fe^{3+} cation in a hexagonal crystallographic system with a corundum structure[67]. This structure has a HCP (001) anion stacking with the "a" and "c" lattice parameters of 0.504 nm and 1.37 nm[68], respectively. Additionally, the maghemite top surface were found to be Fe_3O_4 (111)[75]. The bulk material properties of maghemite nanoparticles are presented in Table 2.3.

Table 2.3: Material properties of maghemite nanoparticles[70, 76-77].

Density (g/cm^3)	Saturation magnetization (emu/g)	Magnetic susceptibility	Coercivity (Oe)
4.86	60–80	8–21	~20

The iron oxide nanoparticles used in this work were synthesized by a co-precipitation method and obtained as a dry powder modified with polyvinylpyrrolidone (PVP). The PVP modification delivered a surface open for further modification. Thus, the iron oxide nanoparticles could readily be modified for the use in this research.

2.2: Surface Modification

Surface modification is used to improve affinity of the nanofillers to the polymer matrix. For instance, solution-induced intercalation, *in-situ* polymerization, and melt processing are used to introduce nanoclays into polymer matricies[1, 9]. These surface modifications decrease the surface energy of the fillers and create favorable interactions between the matrix and filler. The favorable interactions between the filler and matrix increase interfacial adhesion and raise the dispersibility of the nanoparticulates in the composite material. This is vital to the structural reinforcement and stress transfer within nanocomposite systems. Furthermore, the integration of well-dispersed nanomaterials into a polymer matrix has been shown to enhance material's properties[78-81].

Agglomeration of nanoparticulates can result in defect sites inside a composite[82]. The application of an anchored polymer layer acting as a steric boundary, can prevent aggregation of the nanoparticulates in the matrix[83]. Thus, nanolayer thin films of polymer are often applied to nanomaterials via grafting or adsorption processes[84-86]. While adsorption may be the easiest method to attach polymers to the surface, it is usually an impractical approach due to the low bonding strength and inability to permanently functionalize surfaces. However, adsorption may be useful for specific combinations of polymers and surfaces that can complex via hydrogen or ionic bonding. Alternatively, "grafting to" and "grafting from" techniques generally utilize chemical (covalent) anchoring of the polymer chains[87]. The "grafting from" uses surface initiation of polymerization to form surface anchored polymer chains. The "grafting to" method uses already synthesized polymers to modify a surface. Unlike the "grafting from" approach,

the “grafting to” method is a simple and easily scalable surface modification process involving just two steps: surface activation and modification. This research utilizes surface complexation and the “grafting to” method to modify the surfaces of nanoparticulate fillers. These surface modification techniques were chosen for their relative ease of application and compatibility with the use of polyelectrolytes. These two methods of surface modification (surface complexation and “grafting to”) are discussed in the following sections.

2.2.1: Adsorption of PAA on Iron Oxides

Metal oxides’ reactivity with PAA is utilized in a number of practical applications[88]. The reaction between PAA and most metal oxides typically creates monodentate binding. Fe_3O_4, alumina, PbO, Ti_2O_3, and other ferrite nanomaterials (MFe_2O_4: M= Zn, Fe, Co, and Mn) bond with PAA by forming carboxylate salts or ferrite hydroxides[89-92].

Specifically, the complex being formed between PAA and γ-Fe_2O_3 has not been studied in details. However, it is assumed that the binding of PAA to the surface of Fe_3O_4 and γ-Fe_2O_3 is similar, as their surface structures are identical (Figure 2.5)[75].

The binding processes in Figure 2.5 were employed to form high-performance flexible battery anodes[93]. The anchoring of PAA to Fe_3O_4 has been also attributed to hydrogen and/or electrostatic bonding[94-96].

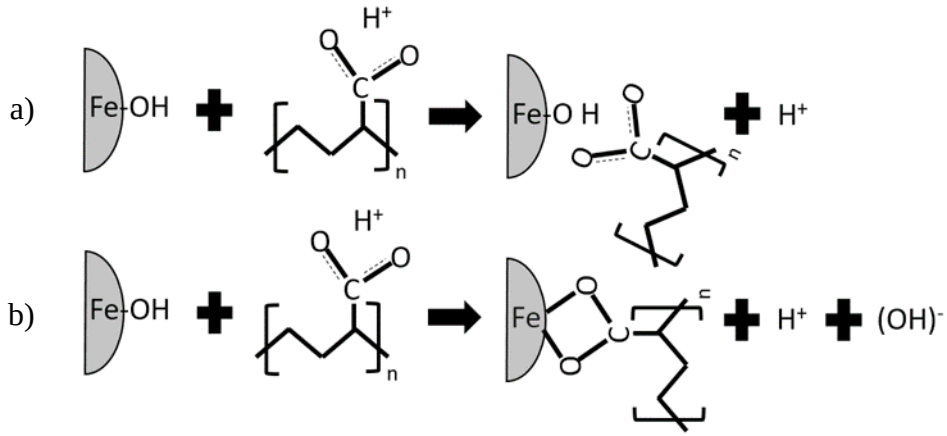

Figure 2.5: Schematic representation of the possible bonding of PAA to the iron oxide surface via (a) hydrogen bonding and (b) chelation.

2.2.2: "Grafting to" Anchoring of Polymer Chains

Polymer grafting provides resourceful means to engineer materials' surface characteristics, such as wettability, adhesion, biocompatibility, conductivity, antifogging, and antifouling[97]. The "grafting to" technique is defined by application of previously synthesized polymer to covalently bond to a surface or polymer chain of complementary chemistry[15]. For the modification of inorganic surfaces, the "grafting to" technique is particularly applicable due to the simplicity and scalability of the process. The most well-known technique is the end-terminated "grafting to" method[98] (Figure 2.6a). In addition, surface modification can be conducted also via the functional groups distributed along the polymer chains[93, 99] (Figure 2.6b). In this case, ~20 % of the functional groups anchor to the surfaces[99] leaving ~80 % of the groups to interact with the environment.

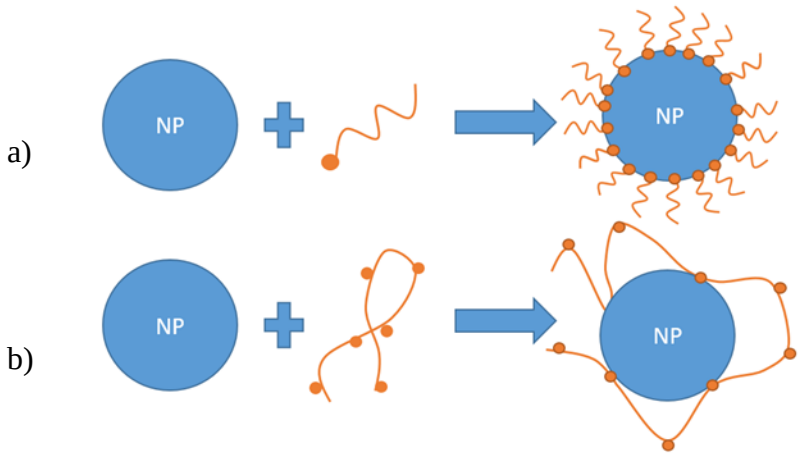

Figure 2.6: The schematic representation of the "grafting to" technique using a) end-terminated and b) functional groups methods.

2.2.3: Polymer-to-Polymer Complexation

The surface modifying polymers (including polyelectrolytes) can act as dispersing or attachment agents depending on the system used. As a dispersing agent, the polymer layer creates a steric boundary on the surface of a particulate to prevent aggregation of the particulates and produce a stable colloidal dispersion. As an attachment agent, the polymer layer binds the modified particulate to a specified surface. Generally, two distinct polyelectrolytes can create a binding complex because of the attractive interaction between their specific functional groups. [100-105] Additionally, these complexes can be very sensitive to charges in density, ionic strength, temperature, polymer concentration, and pH of the solution[106].

With applications in biochemistry, biology, water purification, particle modification, and medicine, polyelectrolytes have been used in very diverse areas[107-109]. This research utilizes polyelectrolytes that can form complexes based on hydrogen bonding. Polymer-

polymer hydrogen bonding is formed when a polymeric hydrogen donor is mixed with a polymeric hydrogen acceptor[110-113]. These hydrogen bonds have uneven charge distribution which can be seen as weak ionic bonding[114].

This study utilizes a well-known complex formation between P2VP and PAA[106, 114-115]. P2VP and PAA stand out as inexpensive hydrogen/ionic bonding polymers[116]. As for the functional groups, the carboxylic acid interacts with the pyridine to form a 2:1 (acid:pyridine) complex (Figure 2.7). However, solvents capable of hydrogen-bonding, such as alcohols, reduce the association ratio to a 1:1[116] (Figure 2.7). The 1:1 ratio is optimal for adhesion, creating strong hydrogen/ionic bonds between the polymer chains.

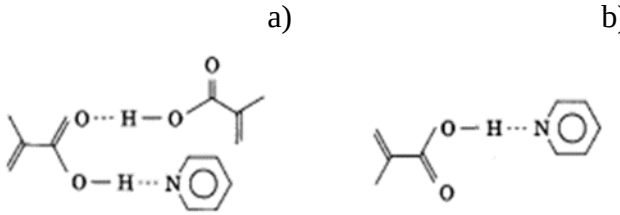

Figure 2.7: Structure of PAA-P2VP complexes depending on the association ratio between carboxylic and pyridine groups a) 2:1 and b) 1:1 (reprinted with permission).

P2VP and PAA have similar bonding structures to poly(4-vinyl pyridine) P4VP and polymethacrylic acid (PMMA). The complexes between PAA, PMMA, P2VP, and P4VP were investigated by measuring the changes in their glass transition temperatures (T_g). An increase in the T_g is directly correlated with the complex formation between polymer chains. It was found that T_g of PAA based complexes was 20 °C higher than the PMMA-based complexes[114] (Figure 2.8). Therefore, PAA was selected in this work for the complex formation. This (higher T_g) is also true for the P4VP complexes compared to

the P2VP complexes. However, P4VP is a more expensive polymer. Thus, P2VP was selected for its much lower cost at the expense of a higher bond strength.

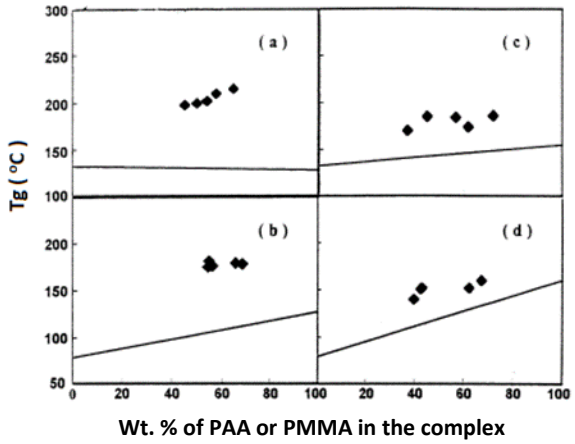

Figure 2.8: Dependence of T_g on the composition of the complexes a) PAA/P4VP, b) PAA/P2VP, c) PMMA/P4VP, and d) PMMA/P2VP (the straight line corresponds to the calculated linear additive rule values) (reprinted with permission).

2.3: Fabrication of Nanocomposites with Orientated Dispersed Phase

Composite materials with oriented fillers have been a main contributor to the modern materials portfolio[15]. However, the fabrication of such nanocomposites is not straightforward[1]. The alignment of the oriented nanofillers must be maintained throughout possible disruptions caused by thermal fluctuations, capillary forces, flow dynamics, and polymer solution melt viscosity heterogeneity, which are often present during composite fabrication[117-119].

Various methods of controlling nanofiller orientation have been attempted including tape casting, melt flow shear, slip casting, layer-by-layer deposition, electrical field, and hot-pressing from a gel[120-125]. The fabricated composites have displayed superior in-plane mechanical properties because of orientation of the fillers. However, these methods are limited by their complex methodologies and/or film geometries[126]. The

magnetic orientation within bulk matrices has shown greater versatility in this aspect. To date, results have been published for magnetically oriented composites involving the following nanoscale fillers: alumina platelets[118, 127-133], silver nanowires[134], boron nitride platelets[135-137], carbon nanotubes[138-140], carbon nanofibers[141-142], lamellar clay (montmorillonite)[143], graphene/graphene oxide[144-147] , Fe_3O_4 nanorods[148], CaP rods[149], cellulose nanowhiskers,[150] and SiC nanoparticles[137].

2.3.1: The Theoretical Aspects of Magnetic Orientation

The magnetic orientation of nanofillers is an effective way to create high degree of orientation within a composite matrix[118]. However, most high modulus nanofillers, like carbon nanotubes and SiCWs, have a very low magnetic susceptibility[151-153] and by themselves are not suitable for this type of orientation. Therefore, magnetic nanoparticles are used in a variety of ways to create highly aligned nanofillers[118]. Specifically, the attachment of magnetic nanoparticles to the surface of non-magnetic rod-shaped particulates can be employed to generate magnetic shell covering the nanofiller. An applied magnetic field would cause the magnetic moment of the shell to orient in the direction of the field. Hence, the orientation of the fillers decorated with the particles would be in the direction of the applied magnetic field as well.

In this respect, Equation 2.1 can be used to predict the critical frequency for the rotation of a paramagnetic rod in a rotating magnetic field[154-155]. The equation, describing the rotation for a single nanorod, is given by:

$$2\pi f_c = w_c \qquad (2.1)$$

where f_c is the critical frequency of the rod rotation or $1/\tau$ (where: τ is the characteristic time of orientation for a paramagnetic nanorod going from 90 ^{o} to 0 ^{o} orientation with the net director); and, w_c is the characteristic frequency.

The Equations 2.1-2.4 are used to estimate the materials characteristic time of orientation (τ) using a drag coefficient, viscosity of the solution, and applied torque.

Namely, w_c is defined by:

$$w_c = \frac{1}{\gamma} \cdot \frac{2V_{mag}}{\mu_o} \cdot \frac{\chi^2}{2+\chi} \cdot B^2 \tag{2.2}$$

where χ is the magnetic susceptibility, B is the strength of the magnetic field, μ is the vacuum permeability, V_{mag} is the volume of the magnetic material, and γ is the drag coefficient[155-157]. The drag coefficient and volume of magnetic materials are defined as:

$$\gamma = \frac{\eta l_w^3 \pi}{3\ln(l_w / d_w) - A} \tag{2.3}$$

$$V_{mag} = \frac{\pi l_w}{4} \cdot (d_w^2 - d_{w+p}^2) \tag{2.4}$$

where η is the viscosity of the matrix, d_w is the diameter of the rod, l_w is the length of the rod, d_{w+p} is the diameter of the rod plus the particles, and $A \approx 2.4$[156].

The development of magnetic orientation for the "as is" diamagnetic materials has been challenging due to the extremely high magnetic field needed to orient them. However, the attachment of magnetic nanoparticles allows for small magnetic fields to induce the orientation[118]. Additionally, recently, the methods for the fabrication of magnetically oriented nanocomposites have greatly improved[158-160]. As a result, the magnetically oriented composites with improved mechanical characteristics have been demonstrated[4, 161].

2.3.2: Magnetic Orientation of Nanofillers

It was shown that the magnetic orientation and positioning of nanofillers has offered the improvement of mechanical properties of nanocomposite materials. For example, 3-dimensional reinforcement of methacrylate resins was achieved using low magnetic fields on alumina nanoplatelets and nanorods modified with magnetite nanoparticles[118]. Namely, the reinforcement is shown to improve tensile yield strength by 60-90 %, and tensile modulus by 260 % with 20 vol. % of nanomaterial fillers[118]. In addition, an epoxy composite containing 27 vol. % of oriented alumina nanoplatelets made using oscillating field and vibration table[162], demonstrated a 140 % and 470 % higher flexural modulus than the equivalent as-cast composite and the polymer matrix[162], respectively. The local reinforcement of polyvinyl alcohol (PVA), polyurethane (PU), and polydimethylsiloxane (PDMS) using magnetic nanofillers has increased the elastic modulus by 265 %, 478 %, and 558 %, respectively[158]. Magnetic alignment has even been used in cellulose-cellulose composites to increases the modulus of paper by approximately 700 %[163]. Furthermore, magnetically oriented carbon nanotubes (CNTs)

within an epoxy matrix composite have produced increase in the tensile modulus by 55 % with 0.2 wt. % of multi-wall carbon nanotubes (MWCNT) and 40 % increase with 0.5 wt. % of single-wall carbon nanotubes (SWCNT)[159, 164]. The data on composites with magnetically oriented fillers are compiled and compared in Table 2.4.

Table 2.4: Changes in mechanical properties of composite materials incorporating magnetically oriented fillers.

Matrix	Filler	Filler's content (vol.%)	Relative increase in tensile modulus (%)
methacrylate resin	alumina nanorods	20	260
PVA	alumina nanorods	20	265
PU	alumina nanorods	20	478
PDMS	alumina nanorods	20	558
epoxy	SWCNT	0.125	55
epoxy	MWCNT	0.3125	40
cellulose	cellulose nanocrystal	5	700

The magnetic alignment of nanofillers does not just improve the mechanical properties, but also offers a variety of other benefits. It has been used to overcome the shear alignment during extrusion[149], for optical applications[165], in electrically conductive and insulating thin films[134, 160, 166-167], thermally conductive composites[168-169], and shape memory materials[161]. For instance, application of the magnetic realignment to overcome shear flow orientation is the method compatible with industrial-scale extrusion processes. It could be applied to create stronger composite fibers and tapes[149]. On the other hand, magnetic iron oxide nanorods based magnetically actuated liquid crystals have been shown to control polarization and intensity of light [165]. These effects can be integrated into optical devices in a wide variety of fields (such as displays, actuators, and optical modulators). Other scientists have shown the formation of optically transparent and electrically conductive thin films using orientation of silver nanowires with attached

superparamagnetic nanoparticles[134]. Additionally, the variations in orientation of graphene based sheets can create highly conductive[166] or insulative[167] composite materials. Oriented MWCNTs can improve conductivity in composites[160]. Thermally conductive composites have been created by the magnetic orientation of carbon nanofibers in polyester, boron nitride-iron oxide nanoparticles in epoxy, and silicon carbide-iron oxide nanoparticles in epoxy[168-169]. In another application of orientation, bioinspired shape memory composites have used the magnetically aligned nanofillers to mimic the internal structure of natural composites to control bending and twisting actuation triggered by external stimuli[161].

2.4: Properties of Composites

The properties of composites are derived from the combination of properties of two or more materials. The composite components are not independent and can reveal strong interfacial interactions that might influence the composite's properties significantly. Specifically, mechanical characteristics depend on stress transfer from the matrix to the inclusions through the interface. Thus, the properties of the composite are affected by the compatibility of the two or more components. In some instances the composite components could be incompatible, causing agglomerations, weak interfacial bonding, voids, or other possible defects in the composite material.

2.4.1: Predicting Composite's Properties

A large number of theoretical models have been developed to predict composite properties[5]. One of the most accepted methods to predict mechanical properties of nanocomposites is the Halpin-Tsia model and equation[170]. This is a semi-empirical

equation developed to model the mechanical properties of oriented and non-oriented discontinuous fillers dispersed into a polymer matrix. Equations 2.5 and 2.6 are used to calculate the mechanical modulus in the direction of the oriented fillers dispersed in a matrix.

$$E_o = E_m\left[\frac{1+\xi\eta f}{1-\eta f}\right] \tag{2.5}$$

$$\eta = \frac{E_f / E_m - 1}{E_f / E_m + \xi} \tag{2.6}$$

where E_o is the predicted composite modulus; E_m -matrix modulus; E_f - fibrous inclusions modulus; f - fiber volume fraction; η- fiber-to-load transfer parameter for the Halpin-Tsia equation; and ξ is the shear coefficient (~2 times the aspect ratio of a fiber).

These equations assume that the matrix only sustains the axial load, stress is transmitted to the fiber through shear stress, all the fibers are aligned in the direction of the stress, there is no transverse or thermal stress, and the fillers are equally dispersed in the matrix[171]. This equation is used in this study to model the properties of magnetically oriented SiCWs dispersed into the epoxy composite materials.

The modulus for randomly oriented fibers can be estimated using Equation 2.7[172-173].

$$E_o = \frac{3}{8}E_l + \frac{5}{8}E_t \tag{2.7}$$

where E_l and E_t are the longitudinal and transverse moduli, respectively. We have already estimated the longitudinal modulus, and the transverse modulus was calculated by equations (4) and (5) assuming ξ equals 2[174].

2.4.2: Surface Effects and Compatibility

Surface effects are determined by chemical and physical interactions at the interface between the reinforcement and the matrix. The interface is a phase discontinuity that can be sharp or gradual. This bi-dimensional region is a finite thickness through which material's parameters (such as the concentration, elemental composition, crystal structure, elastic modulus, density, and the coefficient of thermal expansion) change from the matrix to the filler[1]. It is one of the major contributing factors to the behavior of a composite originated in the compatibility of the matrix and the fiber.

The compatibility of the components in composite materials is a complex term related to chemical and physical relationships between the matrix and the filler[5, 175]. Specifically, wettability of the composite inclusions by the matrix determines the infiltration and spreading of the matrix on the surface of the fillers[1]. The surface roughness of the nanofillers also plays an important role by either creating mechanical interlocking or voids at the interface. Thus, these surface qualities determine the type of bonding that governs the mechanical interactions at the interface.

In general, there are three major types of interfacial bonds: mechanical, physical, and chemical[1]. Mechanical bonds involve interlocking or gripping effects at the interface of the composite. This includes phenomena such as friction associated with the matrix penetrating the roughness of nanofillers' surface. Physical bonding is classified as weak secondary bonding (energy lower than approximately 8–16 kJ/mol) and is associated with van der Waals, polar, and hydrogen bonding. Lastly, chemical bonding is defined as

metallic, ionic, or covalent bonds with bonding energies ranging from 40 kJ/mol to 400 kJ/mol.

Today, the composite interface is understood as an interfacial phase, also known as the interphase[176-177]. The interphase plays an important role in stress transfer as a mechanical transition zone[178-179]. As a transitional zone, the interphase can be designed by changing its thickness, mechanical properties, and the gradient of the mechanical properties across the interphase[179]. The gradient of the interphase is defined as the gradual or abrupt change of mechanical properties through the interphase zone. This can be summarized using the interfacial shear strength (IFSS) theory. Mostly applied to the continuous filler composites, the IFSS theory states that the shear modulus of the interphase region determines the composite's mechanical properties[1, 177]. In turn, the shear modulus of the interphase is established by the structure of the interphase region.

2.5: References

1. Chawla, K. K., *Composite materials. Science and engineering*. Springer Science: New York, 2013; Vol. 3.

2. Weiner, S.; Wagner, H. D., The material bone: Structure-mechanical function relations. *Annu Rev Mater Sci* **1998,** *28*, 271-298.

3. Wainwright, S. A.; Biggs, W. D.; Curry, J. D.; Gosline, J. M., *Mechanical design in organisms*. Princeton University Press: Princeton, 1982.

4. Elices, M., *Structural biological materials*. Pergamon Press: Amsterdam, 2000.

5. Hull, D.; Clyne, T., *An introduction to composite materials*. Cambridge University Press: Cambridge, 1996.

6. Barrera, E. V.; Lozano, K., New technologies, new composites. *Journal of the Minerals, Metals & Materials Society* **2000,** *52* (11), A32-A32.

7. Barrera, E. V.; Shofner, M. L.; Corral, E. L., *Carbon nanotubes: Science and applications*. CRC Press Taylor and Francis Group: Boca Raton, 2005.

8. Shofner, M. L.; Khabashesku, V. N.; Barrera, E. V., Processing and mechanical properties of fluorinated single-wall carbon nanotube-polyethylene composites. *Chem Mater* **2006,** *18* (4), 906-913.

9. Ajayan, M. R.; Schadler, L. S.; Braun, P. V., *Nanocomposite science and technology*. Wiley-VCH: Weinheim, 2003.

10. Koo, K. H., *Polymer nanocomposites*. Mcgraw-Hill: New York, 2006.

11. Lee, H. S.; Fasulo, P. D.; Rodgers, W. R.; Paul, D. R., TPO based nanocomposites. Part 1. Morphology and mechanical properties. *Polymer* **2005,** *46* (25), 11673-11689.

12. Yuan, Z. K.; Yu, J. H.; Rao, B. L.; Bai, H.; Jiang, N.; Gao, J.; Lu, S. R., Enhanced thermal properties of epoxy composites by using hyperbranched aromatic polyamide grafted silicon carbide whiskers. *Macromol Res* **2014,** *22* (4), 405-411.

13. Carraro, M.; Gross, S., Hybrid materials based on the embedding of organically modified transition metal oxoclusters or polyoxometalates into polymers for functional applications: a review. *Materials* **2014,** *7* (5), 3956-3989.

14. Gun'ko, Y. K., Chemical functionalisation of carbon nanotubes for polymer reinforcement. In *Carbon Nanotube-Polymer Composites*, Tasis, D., Ed. The Royal Society of Chemistry: Cambridge, 2013; Vol. 27.

15. Sperling, L. H., *Introduction to physical polymer science*. John and Wiley, Inc.: Hoboken, 1986.

16. Inam, F., Epoxy – the hub for the most versatile polymer with exceptional combination of superlative features. *Epoxy* **2014,** *1*, 1-2.

17. McMurry, J.; Simanek, E., *Fundamentals of organic chemisty*. 6th ed.; Thomson Brooks/Cole: Belmont, 2007.

18. Grenier-Loustalot, M.-F.; Grenier, P., The role of impurities in the mechanisms and kinetics of reactions of epoxy resins and their effects on final resin properties. *Brit Polym J* **1990,** *22*, 303-313.

19. Huntsman Container Corporation, High preformance components. Huntsman, Ed. Huntsman: North America, 2015.

20. Mika, T. F.; Bauer, R. S., Curing agents and modifiers In *Epoxy Resins. Chemistry and technology*, May, C. A., Ed. Marcel Dekker: New York, 1988.

21. Cahill, P. J. Alkenyl-substituted succinic anhydride. US Patent 3855251 A, 1974.

22. Wolfe, N. G. Latent catalysts for one-component epoxy resin/anhydride compositions. US Patent 3689444 A, 1972.

23. Chatrabhuti, S.; Chirachanchai, S., Single step coupling for multi-responsive water-based chitin/chitosan magnetic nanoparticles. *Carbohydr Polym* **2013,** *97* (2), 441-50.

24. Ahmad, T.; Ganguli, A. K.; Ganguly, A.; Ahmed, J.; Wani, I. A.; Khatoon, S., Chemistry of reverse micelles: A versatile route to the synthesis of nanorods and nanoparticles. In *Nanotubes, Nanowires, Nanobelts and Nanocoils - Promise, Expectations and Status*, P. R. Bandaru; S. Grego; I. Kinloch, Eds. Materials Research Society: Warrendale, 2009; Vol. 1142, pp 75-88.

25. Mu, B.; Zhang, W. B.; Wang, A. Q., Facile fabrication of superparamagnetic coaxial gold/halloysite nanotubes/Fe_3O_4 nanocomposites with excellent catalytic property for 4-nitrophenol reduction. *J Mater Sci* **2014,** *49* (20), 7181-7191.

26. Jiao, H.; Wang, J. L., Thermal decomposition fabrication, growth mechanism, and characterization of rod-like γ-Fe_2O_3. *Synth React Inorg M* **2014,** *44* (9), 1354-1357.

27. Korneva, G.; Ye, H.; Gogotsi, Y.; Halverson, D.; Friedman, G.; Bradley, J.-C.; Kornev, K. G., Carbon nanotubes loaded with magnetic particles. *Nano Letters* **2005,** *5* (5), 879-884.

28. Tokarev, A.; Rubin, B.; Bedford, M.; Kornev, K. G., Magnetic nanorods for optofluidic applications. *AIP conference proceedings* **2010,** *1311*, 204-209.

29. Fan, J.; Chu, P. K., *Silicon carbide nanostructures fabrication, structure, and properties*. Springer: New York, 2014.

30. Advanced Composite Materials, L. *Technical data sheet: Silar® SC-9M*; Greer, SC, 2012.

31. Merz, K. M.; Adamsky, R. F., Synthesis of the wurtzite form of silicon carbide. *J Am Chem Soc* **1959,** *81* (1), 250-251.

32. Burgemeister, E. A.; Vonmuench, W.; Pettenpaul, E., Thermal conductivity and electrical properties of 6H silicon-carbide. *J Appl Phys* **1979,** *50* (9), 5790-5794.

33. Su, C. M.; Wuttig, M.; Fekade, A.; Spenceer, M., Elastic and anelastic properties of chemical-vapor-deposited epitaxial 3C-SiC. *J Appl Phys* **1993,** *77* (11), 5611.

34. Sawyer, L. C. Process for dispersing silicon carbide whiskers. US Patent 4956316 A, 1990.

35. Wagner, R. S.; Ellis, W. C., Vapor-liquid-solid mechanism of single crystal growth *Appl Phys Lett* **1964,** *4* (5), 89-90.

36. Kuang, J. L.; Cao, W. B., Silicon carbide whiskers: Preparation and high dielectric permittivity. *J Am Ceram Soc* **2013,** *96* (9), 2877-2880.

37. Yang, W.; Araki, H.; Kohyama, A.; Thaveethavorn, S.; Suzuki, H.; Noda, T., Fabrication in-situ SiC nanowires/SiC matrix composite by chemical vapour infiltration process. *Mater Lett* **2004,** *58*, 3145-3148.

38. Chu, Y. H.; Fu, Q. G.; Zhang, Z. Z.; Li, H. J.; Li, K. Z.; Lei, Q., Microstructure and growth mechanism of SiC nanowires with periodically fluctuating hexagonal prisms by CVD. *J Alloy Compd* **2010,** *508* (2), L36-L39.

39. Wei, J.; Li, K. Z.; Chen, J.; Yuan, H. D., Synthesis of centimeter-scale ultra-long SiC nanowires by simple catalyst-free chemical vapor deposition. *J Cryst Growth* **2011,** *335* (1), 160-164.

40. Tang, C. C.; Fan, S. S.; Dang, H. Y.; Zhao, J. H.; Zhang, C.; Li, P.; Gu, Q., Growth of SiC nanorods prepared by carbon nanotubes-confined reaction. *J Cryst Growth* **2000,** *210* (4), 595-599.

41. Pan, Z. W.; Lai, H. L.; Au, F. C. K.; Duan, X. F.; Zhou, W. Y.; Shi, W. S.; Wang, N.; Lee, C. S.; Wong, N. B.; Lee, S. T.; Xie, S. S., Oriented silicon carbide nanowires: Synthesis and field emission properties. *Adv Mater Res* **2000,** *12* (16), 1186-1190.

42. Vix-Guterl, C.; McEnaney, B.; Ehrburger, P., SiC material produced by carbothermal reduction of a freeze gel silica-carbon artefact. *J Eur Ceram Soc* **1999,** *19* (4), 427-432.

43. Zhou, W. M.; Liu, X.; Zhang, Y. F., Simple approach to β-SiC nanowires: Synthesis, optical, and electrical properties. *Appl Phys Lett* **2006,** *89* (22), 223124.

44. Dawes, S. B.; Stempin, J. L.; Wexell, D. R. Multicomponent ceramic matrix composites. US Patent 5153152 A, 1991.

45. Rogers, W. Pressureless sintering of whisker reinforced alumina composites. US Patent 5656217 A.

46. Quantrille, T. E.; Rogers, W. M. Composite materials and devices comprising single crystal silicon carbide heated by electromagnetic radiation. US Patent 8648284 B2, 2007.

47. Rogers, W. Silicon carbide fibers essentially devoid of whiskers and method for preparation thereof. US Patent 20050013997 A1, 2004.

48. Quantrille, T. E.; Short, L. A. Functionalized silicon carbide and functionalized inorganic whiskers for improving abrasion resistance of polymers. US Patent 20130059987 A1, 2013.

49. Ridi, F.; Bonini, M.; Baglioni, P., Magneto-responsive nanocomposites: preparation and integration of magnetic nanoparticles into films, capsules, and gels. *Adv Colloid Interface Sci* **2014,** *207*, 3-13.

50. Hironari, S.; Nakano, Y.; Matsushita, H.; Onoe, A.; Kanai, H.; Yamashita, Y., Effect of heat treatment on dielectric properties of X7R designated MLCs with Ni internal electrodes. *J Mater Synth Process* **1998,** *6*, 415-418.

51. Smogunov, A.; Dal Corso, A.; Tosatti, E., Selective d-state conduction blocking in nickel nanocontacts. *Surf Sci* **2002,** *507*, 609-614.

52. Hernandez, R.; Polizu, S.; Turenne, S.; Yahia, L., Characteristics of porous nickel-titanium alloys for medical applications. *Biomed Mater Eng* **2002,** *12*, 37-45.

53. Zhang, W. X.; Wang, C. B.; Lien, H. L., Treatment of chlorinated organic contaminants with nanoscale bimetallic particles. *Catal Today* **1998,** *40* (4), 387-395.

54. Couto, G. G.; Klein, J. J.; Schreiner, W. H.; Mosca, D. H.; de Oliveira, A. J. A.; Zarbin, A. J. G., Nickel nanoparticles obtained by a modified polyol process: Synthesis, characterization, and magnetic properties. *J Appl Polym Sci* **2007,** *311* (2), 461-468.

55. Eluri, R.; Paul, B., Synthesis of nickel nanopartices by hydrazine reduction mechanistic study and continuous flow synthesis. *J Nanopart Res* **2012,** *14*, 800-814.

56. Anthony, J. W.; Bideaux, R. A.; Bladh, K. W.; Nichols, M. C., *Handbook of mineralogy*. Mineral Data Publishing: Tucson, 1995.

57. Tsurin, V. A.; Yermakov, A. Y.; Uimin, M. A.; Mysik, A. A.; Shchegoleva, N. N.; Gaviko, V. S.; Maikov, V. V., Synthesis, structure, and magnetic properties of iron and nickel nanoparticles encapsulated into carbon. *Phys Solid State* **2013,** *56* (2), 287-301.

58. Hwang, J. H.; Dravid, V. P., Magnetic properties of graphitically encapsulated nickel nanocrystals. *J Mater Res* **1996,** *12* (4).

59. Wu, S.-H.; Chen, D.-H., Synthesis and characterization of nickel nanoparticles by hydrazine reduction in ethylene glycol. *J Colloid Interf Sci* **2003,** *259*, 282-286.

60. Chen, D.-H.; Hsieh, C.-H., Synthesis of nickel nanoparticles in aqueous cationic surfactant solutions. *J Mat Chem* **2002,** *12*, 2412-2415.

61. Degen, A.; Macek, J., Preparation of submicrometer nickel powders by the reduction from nonaqueous media. *Nanostruct Mater* **1999,** *12* (1-4), 225-228.

62. Koltypin, Y.; Fernandez, A.; Rojas, T. C.; Campora, J.; Palma, P.; Prozorov, R.; Gedanken, A., Encapsulation of nickel nanoparticles in carbon obtained by the sonochemical decomposition of $Ni(C_8H_{12})_2$. *Chem Mater* **1999,** *11* 1331-1335.

63. De Caro, D.; Bradley, J. S., Surface spectroscopic study of carbon monoxide adsorption on nanoscale nickel colloids prepared from a zerovalent organometallic precursor. *Langmuir* **1997,** *13*, 3067-3069.

64. Zhang, H. T.; Wu, G.; Chen, X. H.; Qiu, X. G., Synthesis and magnetic properties of nickel nanocrystals. *Mater Res Bull* **2006,** *41* (3), 495-501.

65. Steigerwald, M. L.; Alivisatos, A. P.; Gibson, J. M.; Harris, T. D.; Kortan, R.; Muller, A. J.; Thayer, A. M.; Duncan, T. M.; Douglass, D. C.; Brus, L. E., Surface derivatization and isolation of semiconductor cluster molecules. *J Am Chem Soc* **1988,** *110* (10), 3046-3050.

66. Wu, Z. G.; Munoz, M.; Montero, O., The synthesis of nickel nanoparticles by hydrazine reduction. *Adv Powder Technol* **2010,** *21* (2), 165-168.

67. Teja, A. S.; Koh, P. Y., Synthesis, properties, and applications of magnetic iron oxide nanoparticles. *Prog Cryst Growth Ch* **2009,** *55* (1-2), 22-45.

68. Parkinson, G. S., Iron oxide surfaces. *Surf Sci Rep* **2016,** *71* (1), 272-365.

69. Bertelsen, P.; Goetz, W.; Madsen, M. B.; Kinch, K. M.; Hviid, S. F.; Knudsen, J. M.; Gunnlaugsson, H. P.; Merrison, J.; Nornberg, P.; Squyres, S. W.; Bell, J. F., 3rd; Herkenhoff, K. E.; Gorevan, S.; Yen, A. S.; Myrick, T.; Klingelhofer, G.; Rieder, R.; Gellert, R., Magnetic properties experiments on the Mars exploration Rover Spirit at Gusev Crater. *Science* **2004,** *305* (5685), 827-829.

70. Cornell, R. M.; Schwertmann, U., *The iron oxides: Structure, properties, reactions, occurrences and uses*. Wiley-VCH: Weinheim, 2003.

71. Kishkinev, D. A.; Chernetsov, N. S., Magnetoreception systems in birds: a review of current research. *Biol Bull Rev* **2015,** *5*, 46-62.

72. Kirschvink, J. L.; Kobayashi-Kirschvink, A.; Woodford, B. J., Magnetite biomineralization in the human brain. *P Natl Acad Sci USA* **1992,** *89* (16), 7683-7687.

73. Frankel, R. B.; Blakemore, R. P.; Wolfe, R. S., Magnetite in fresh water magnetotactic bacteria. *Science* **1979,** *203*, 1355-1356.

74. Tartaj, P.; Morales, M. P.; Gonzalez-Carreño, T.; Veintemillas-Verdaguer, S.; Serna, C. J., The iron oxides strike back: From biomedical applications to energy storage devices and photoelectrochemical water splitting. *Adv Mater Res* **2011,** *23* (5246-5249).

75. Bowker, M.; Hutchings, G.; Davies, P. R.; Edwards, D.; Davies, R.; Shaikhutdinov, S.; Freund, H. J., Surface structure of gamma-Fe_2O_3 (111). *Surf Sci* **2012,** *606* (21-22), 1594-1599.

76. Prene, P.; Tronc, E.; Jolivet, J.-P.; Livage, J., Magnetic properties of isolated γ-Fe_2O_3 particles *IEEE Trans Magn* **1993,** *29* (6), 2658 - 2660.

77. Dutta, P.; Manivannan, A.; Seehra, M. S.; Shah, N.; Huffman, G. P., Magnetic properties of nearly defect-free maghemite nanocrystals. *Phys Rev B* **2004,** *70* (17), 174428.

78. Bansal, A.; Yang, H.; Li, C.; Cho, K.; Benicewicz, B. C.; Kumar, S. K.; Schadler, L. S., Quantitative equivalence between polymer nanocomposites and thin polymer films. *Nat Mater* **2005,** *4* (9), 693-698.

79. Putz, K.; Krishnamoorti, R.; Green, P. F., The role of interfacial interactions in the dynamic mechanical response of functionalized SWNT-PS nanocomposites. *Polymer* **2007,** *48* (12), 3540-3545.

80. Putz, K. W.; Mitchell, C. A.; Krishnamoorti, R.; Green, P. F., Elastic modulus of single-walled carbon nanotube/poly(methyl methacrylate) nanocomposites. *J Polym Sci Pol Phys* **2004,** *42* (12), 2286-2293.

81. Ramanathan, T.; Liu, H.; Brinson, L. C., Functionalized SWNT/polymer nanocomposites for dramatic property improvement. *J Polym Sci Pol Phys* **2005,** *43* (17), 2269-2279.

82. Mittal, V., Need of new surface modification In *Polymer Nanocomposites: Advances in Filler Surface*, Nova Science Publishers: New York, 2009.

83. Iijima, M.; Kamiya, H., Surface modification for improving the stability of nanoparticles in liquid media. *Kona Powder Part J* **2009,** *27* (27), 119-129.

84. Kolb, H. C.; Finn, M. G.; Sharpless, K. B., Click chemistry: Diverse chemical function from a few good reactions. *Angew Chem Int Edit* **2001,** *40* (11), 2004-2021.

85. Caruso, F., Nanoengineering of particle surfaces. *Adv Mater Res* **2001,** *13* (1), 11–22.

86. Bhattachary, A.; Misra, B. N., Grafting: a versatile means to modify polymers: Techniques, factors and applications. *Prog Polym Sci* **2004,** *29*, 767-814.

87. Berger, S.; Synytska, A.; Ionov, L.; Elchhorn, K. J.; Stamm, M., Stimuli-responsive bicomponent polymer janus particles by "grafting from"/"grafting to" approaches. *Macromolecules* **2008,** *41*, 9669-9676.

88. Hu, H.; Saniger, J.; Garcia-Alejandre, J.; Castano, V. M., Fourier transform infrared spectroscopy studies of the reaction between polyacrylic acid and metal oxides. *Mater Lett* **1991,** *12* (4), 281-285.

89. Wu, X. F.; Ding, Z.; Wang, W.; Song, N. N.; Khaimanov, S.; Tsidaeva, N., Effect of polyacrylic acid addition on structure, magnetic and adsorption properties of manganese ferrite nanoparticles. *Powder Technol* **2016,** *295*, 59-68.

90. Xiong, P.; Chen, Q.; He, M. Y.; Sun, X. Q.; Wang, X., Cobalt ferrite-polyaniline heteroarchitecture: a magnetically recyclable photocatalyst with highly enhanced performances. *J Mater Chem* **2012,** *22* (34), 17485-17493.

91. Zhao, X. R.; Wang, W.; Zhang, Y. J.; Wu, S. Z.; Li, F.; Liu, J. P., Synthesis and characterization of gadolinium doped cobalt ferrite nanoparticles with enhanced adsorption capability for Congo Red. *Chem Eng J* **2014,** *250*, 164-174.

92. Chen, R.; Wang, W.; Zhao, X. R.; Zhang, Y. J.; Wu, S. Z.; Li, F., Rapid hydrothermal synthesis of magnetic Co_xNi_1-xFe_2O_4 nanoparticles and their application on removal of Congo red. *Chem Eng J* **2014,** *242* (2014), 226-233.

93. Cheng, Y. H.; Chen, Z.; Zhu, M. F.; Lu, Y. F., Polyacrylic acid assisted assembly of oxide particles and carbon nanotubes for high-performance flexible battery anodes. *Adv Energy Mater* **2015,** *5* (6), 1401207.

94. Wu, H. X.; Wang, T. J.; Jin, Y., Effects of -OH groups on Fe_3O_4 particles on the heterogeneous coating in a hydrous alumina coating process. *Ind Eng Chem Res* **2007,** *46* (3), 761-766.

95. Fresnais, J.; Yan, M.; Courtois, J.; Bostelmann, T.; Bee, A.; Berret, J. F., Poly(acrylic acid)-coated iron oxide nanoparticles: quantitative evaluation of the coating properties and applications for the removal of a pollutant dye. *J Colloid Interf Sci* **2013,** *395*, 24-30.

96. Fresnais, J.; Berret, J. F.; Frka-Petesic, B.; Sandre, O.; Perzynski, R., Electrostatic co-assembly of iron oxide nanoparticles and polymers: Towards the generation of highly persistent superparamagnetic nanorods. *Adv Mater Res* **2008,** *20* (20), 3877–3881.

97. Uyama, Y.; Kato, K.; Ikada, Y., Surface modification of polymers by grafting. In *Adv Polym Sci*, Springer: Berlin, 1998; pp 1-39.

98. Ligoure, C.; Leibler, L., Thermodynamics and kinetics of grafting end-functionalized polymers to an interface. *J Phys-Paris* **1990,** *51* (12), 1313-1328.

99. Guiselin, O., Irreversable adsorption of a concentrated polymer solution. *Europhys Lett* **1991,** *17* (3), 225-230.

100. Coleman, M. M.; Draf, J. F.; Painter, P. C., *Specific interactions and the miscibility of polymer blends*. Technomic Publishing: Lancaster, 1991.

101. Dong, J.; Ozaki, Y.; Nakashima, K., Infrared, Raman, and near-infrared spectroscopic evidence for the coexistence of various hydrogen-bond forms in poly(acrylic acid). *Macromolecules* **1997,** *30* (4), 1111-1117.

102. *Water-soluble polymers: Synthesis, solution properties, and applications*. Americal Chemical Society: Washington, DC, 1991; Vol. 467.

103. Usaitis, A.; Maunu, S. L.; Tenhu, H., Aggregation of the interpolymer complex of poly(methacrylic acid) and poly(vinyl pyrrolidone) in aqueous solutions. *Eur Polym J* **1997,** *33* (2), 219-223.

104. Illiopoulos, I.; Halary, J. L.; Audebert, R., Polymer complexes stabilized through hydrogen bonds. Influence of "structure defects" on complex formation: Viscometry and fluorescence polarization measurements. *J Polym Sci A Polym Chem* **1988,** *26*, 275-284.

105. Zhu, L.; Jiang, M.; Liu, L.; Zhou, H.; Fan, L. J.; Zhang, Y.; Zhang, Y. B.; Wu, C., Intermacromolecular complexation due to specific interactions. 6. Miscibility and complexation between poly{styrene-co-[p(2-hydroxypropan-2-yl)Styrene]} and poly[n-butyl methacrylate-co-(4-vinylpyridine)]. *J Macromol Sci Phys* **1998,** *B37* (6), 805-826.

106. Kaczmarek, H.; Szalla, A.; Kaminska, A., Study of poly(acrylic acid)-poly(vinylpyrrolidone) complexes and their photostability. *Polymer* **2001,** *42* (14), 6057-6069.

107. Phillipp, B.; Dautzenberg, H.; Linow, K. J.; Kotz, J.; Dawydoff, W., Polyelectrolyte complexes - recent developments and open problems. *Prog Polym Sci* **1988,** *14*, 91-172.

108. Tripathi, B. P.; Dubey, N. C.; Stamm, M., Functional polyelectrolyte multilayer membranes for water purification applications. *J Hazard Mater* **2013,** *252-253*, 401-12.

109. Nypelo, T.; Osterberg, M.; Zu, X. J.; Laine, J., Preparation of ultrathin coating layers using surface modified silica nanoparticles. *Colloids Surf A* **2011,** *392* (1), 313-321.

110. Shannon, P. C.; Lochhead, R. Y., Polyacid microstructural effects in complexation with poly(vinylpyrrolidone). *Polym Prepr ACS* **1996,** *37*, 471.

111. Chatterjee, S. K.; Sethi, K. R.; Yadav, D., Selectivity in interpolymer complexation involving nonionic polymers, polycarboxylic acid and phenolic polymer. *Polymer* **1987,** *28* (3), 519-524.

112. Chatterjee, S. K.; Yadav, J. B.; Sethi, K. R., Influence of grafting on the thermodynamic parameters and stability constants of some intermacromolecular complexes of poly(methacrylic acid) and a graft copolymer. *Angew Makromol Chem* **1987,** *154*, 121-130.

113. Bimendina, L. A.; Roganov, V. V.; Bekturov, E. A., Hydrodynamic properties of complexes poly(methacrylic acid) - polyvinylpyrrolidone in solutions. *Vysokomol Soedin* **1974,** *A16* (12), 2810-2814.

114. Zhou, X.; Goh, S. H.; Lee, S. Y.; Tan, K. L., XPS and FTi.r. studies of interactions in poly(carboxylic acid) poly(vinylpyridine) complexes. *Polymer* **1998,** *39* (16), 3631-3640.

115. Wang, L. Y.; Fu, Y.; Wang, Z. Q.; Fan, Y. G.; Zhang, X., Investigation into an alternating multilayer film of poly(4-vinylpyridine) and poly(acrylic acid) based on hydrogen bonding. *Langmuir* **1999,** *15* (4), 1360-1363.

116. Fujimori, K.; Trainor, G.; Costigan, M., Complexation and rate of polymerization of acrylic acid and methacrylic acid in the presence of poly(4-vinylpyridine) in dilute methanol solution. *J Polym Sci A Polym Chem* **1984,** *22*, 2479-2487.

117. Faure, B.; Wetterskog, E.; Gunnarsson, K.; Josten, E.; Hermann, R. P.; Bruckel, T.; Andreasen, J. W.; Meneau, F.; Meyer, M.; Lyubartsev, A.; Bergstrom, L.; Salazar-Alvarez, G.; Svedlindh, P., 2D to 3D crossover of the magnetic properties in ordered arrays of iron oxide nanocrystals. *Nanoscale* **2013,** *5* (3), 953-60.

118. Erb, R. M.; Libanori, R.; Rothfuchs, N.; Studart, A. R., Composites reinforced in three dimensions by using low magnetic fields. *Science* **2012,** *335* (6065), 199-204.

119. Odenbach, S., Ferrofluids - magnetically controlled suspensions. *Colloid Surf A* **2003,** *217* (1-3), 171-178.

120. Libanori, R.; Munch, F. H. L.; Montenegro, D. M.; Studart, A. R., Hierarchical reinforcement of polyurethane-based composites with inorganic micro- and nanoplatelets. *Compos Sci Technol* **2012,** *72* (3), 435-445.

121. Bonderer, L. J.; Studart, A. R.; Gauckler, L. J., Bioinspired design and assembly of platelet reinforced polymer films. *Science* **2008,** *319* (5866), 1069-1073.

122. Lin, T. H.; Huang, W. H.; Jun, I. K.; Jiang, P., Bioinspired assembly of surface-roughened nanoplatelets. *J Colloid Interf Sci* **2010,** *344* (2), 272-278.

123. Gurbuz, S. N.; Dericioglu, A. F., Effect of reinforcement surface functionalization on the mechanical properties of nacre-like bulk lamellar composites processed by a hybrid conventional method. *Mat Sci Eng C-Mater* **2013,** *33* (4), 2011-2019.

124. Bonderer, L. J.; Feldman, K.; Gauckler, L. J., Platelet-reinforced polymer matrix composites by combined gel-casting and hot-pressing. Part II: Thermoplastic polyurethane matrix composites. *Compos Sci Technol* **2010,** *70* (13), 1966-1972.

125. Kacir, L.; Narkis, M.; Ishai, O., Aligned short glass fiber-epoxy composites. *Composites* **1978,** *9* (2), 89-92.

126. Corni, I.; Harvey, T. J.; Wharton, J. A.; Stokes, K. R.; Walsh, F. C.; Wood, R. J., A review of experimental techniques to produce a nacre-like structure. *Bioinspir Biomim* **2012,** *7* (3), 031001.

127. Libanori, R.; Erb, R. M.; Studart, A. R., Mechanics of Platelet-Reinforced Composites Assembled Using Mechanical and Magnetic Stimuli. *ACS Applied Materials & Interfaces* **2013,** *5* (21), 10794-10805.

128. Erb, R. M.; Cherenack, K. H.; Stahel, R. E.; Libanori, R.; Kinkeldei, T.; Munzenrieder, N.; Troster, G.; Studart, A. R., Locally Reinforced Polymer-Based Composites for Elastic Electronics. *ACS Applied Materials & Interfaces* **2012,** *4* (6), 2860-2864.

129. Erb, R. M.; Sander, J. S.; Grisch, R.; Studart, A. R., Self-shaping composites with programmable bioinspired microstructures. *Nat Commun* **2013,** *4*, 1712.

130. Kokkinis, D.; Schaffner, M.; Studart, A. R., Multimaterial magnetically assisted 3D printing of composite materials. *Nat Commun* **2015,** *6*, 8643.

131. Le Ferrand, H.; Bouville, F.; Niebel, T. P.; Studart, A. R., Magnetically assisted slip casting of bioinspired heterogeneous composites. *Nat Mater* **2015,** *14* (11), 1172-9.

132. Martin, J. J.; Fiore, B. E.; Erb, R. M., Designing bioinspired composite reinforcement architectures via 3D magnetic printing. *Nat Commun* **2015,** *6*, 8641.

133. Studart, A. R.; Erb, R. M., Bioinspired Materials that Self-Shape through Programmed Microstructures. *Soft Matter* **2014,** *10*.

134. Trotsenko, O.; Tokarev, A.; Gruzd, A.; Enright, T.; Minko, S., Magnetic field assisted assembly of highly ordered percolated nanostructures and their application for transparent conductive thin films. *Nanoscale* **2015,** *7* (16), 7155-7161.

135. Yuan, C.; Duan, B.; Li, L.; Xie, B.; Huang, M.; Luo, X., Thermal conductivity of polymer-based composites with magnetic aligned hexagonal boron nitride platelets. *ACS Appl Mater Interfaces* **2015,** *7* (23), 13000-6.

136. Lin, Z.; Liu, Y.; Raghavan, S.; Moon, K. S.; Sitaraman, S. K.; Wong, C. P., Magnetic alignment of hexagonal boron nitride platelets in polymer matrix: toward high performance anisotropic polymer composites for electronic encapsulation. *ACS Appl Mater Interfaces* **2013,** *5* (15), 7633-40.

137. Kim, K.; Ju, H.; Kim, J., Vertical particle alignment of boron nitride and silicon carbide binary filler system for thermal conductivity enhancement. *Composites Science and Technology* **2016,** *123*, 99-105.

138. Yamamoto, N.; Manohara, H.; Platzman, E., Magnetically anisotropic additive for scalable manufacturing of polymer nanocomposite: iron-coated carbon nanotubes. *Mater Res Express* **2016,** *3* (2).

139. Malkina, O.; Mahfuz, H.; Sorge, K.; Rondinone, A.; Chen, J.; More, K.; Reeves, S.; Rangari, V., Magnetic Alignment of SWCNTs Decorated with Fe_3O_4 to Enhance Mechanical Properties of SC-15 Epoxy. *Aip Advances* **2013,** *3* (4).

140. Kazemikia, K.; Bonabi, F.; Asadpoorchallo, A.; Shokrzadeh, M., Influence of the concentration of carbon nanotubes on electrical conductivity of magnetically aligned MWCNT-polypyrrole composites. *B Mater Sci* **2016,** *39* (2), 457-462.

141. Pech-May, N. W.; Vales-Pinzon, C.; Vega-Flick, A.; Cifuentes, A.; Oleaga, A.; Salazar, A.; Alvarado-Gil, J. J., Study of the Thermal Properties of Polyester Composites Loaded with Oriented Carbon Nanofibers Using the Front-Face Flash Method. *Polymer Testing* **2016,** *50*, 255-261.

142. Das, A.; Raffi, M.; Megaridis, C.; Fragouli, D.; Innocenti, C.; Athanassiou, A., Magnetite (Fe_3O_4)-filled carbon nanofibers as electro-conducting/superparamagnetic nanohybrids and their multifunctional polymer composites. *Journal of Nanoparticle Research* **2015,** *17* (1).

143. Lv, F. Z.; Xu, L. N.; Xu, Z. X.; Fu, L. L.; Zhang, Y. H., Fabrication and characterization of the orientated MMT/PI composite films via relatively low magnetic field. *J Appl Polym Sci* **2015,** *132* (1), 41224.

144. Yan, H. Y.; Tang, Y. X.; Long, W.; Li, Y. F., Enhanced thermal conductivity in polymer composites with aligned graphene nanosheets. *J Mater Sci* **2014,** *49* (15), 5256-5264.

145. Yan, H. Y.; Wang, R. R.; Li, Y. F.; Long, W., Thermal conductivity of magnetically aligned graphene-polymer composites with Fe_3O_4-decorated graphene nanosheets. *J Electron Mater* **2015,** *44* (2), 658-666.

146. Ding, L.; Liu, L. P.; Li, P. G.; Lv, F. Z.; Tong, W. S.; Zhang, Y. H., Dielectric Properties of Graphene-Iron Oxide/Polyimide Films with Oriented Graphene. *Journal of Applied Polymer Science* **2016,** *133* (12).

147. Le Ferrand, H.; Bolisetty, S.; Demirors, A. F.; Libanori, R.; Studart, A. R.; Mezzenga, R., Magnetic assembly of transparent and conducting graphene-based functional composites. *Nat Commun* **2016,** *7*, 12078.

148. Wang, M. S.; He, L.; Zorba, S.; Yin, Y. D., Magnetically Actuated Liquid Crystals. *Nano Letters* **2014,** *14* (7), 3966-3971.

149. Martin, J. J.; Riederer, M. S.; Krebs, M. D.; Erb, R. M., Understanding and Overcoming Shear Alignment of Fibers during Extrusion. *Soft Matter* **2015,** *11* (2), 400-405.

150. Li, D. S.; Liu, Z. Y.; Al-Haik, M.; Tehrani, M.; Murray, F.; Tannenbaum, R.; Garmestani, H., Magnetic alignment of cellulose nanowhiskers in an all-cellulose composite. *Polym Bull* **2010,** *65* (6), 635-642.

151. Bornstein, L., Diamagnetic susceptibility. In *Numerical data and functional relationships in science and technology*, Springer-Verlag: Heidelberg, 1986; Vol. II.

152. Bornstein, L., Coordination and Organometallic Transition Metal Compounds. In *Numerical data and functional relationships in science and technology*, Springer-Verlag: Heidelberg, 1966-1984; Vol. II/2, II/8, II/10, II/11,and II/12a.

153. Applehey, M. P.; McBain, J. W.; Biodet, M. L.; Boll , M., Relaxation paramagnetique. In *Tables de constantes et donnees numerique*, Masson: Paris, 1957; Vol. 7.

154. Landau, L. D.; Lifshitz, E. M., *Electrodynamics of continuous media*. Pergamon: Oxford, 1960.

155. Kornev, K. G.; Gu, Y.; Aprelev, P.; Tokarev, A., Magnetic rotational spectroscopy for probing rheology of nanoliter droplets and thin films. In *Characterization tools for nanoscience & nanotechnology*, Kumar, C., Ed. Springer: 2015; Vol. 6.

156. Gu, Y.; Burtovyy, R.; Townsend, J.; Owens, J. R.; Luzinov, I.; Kornev, K. G., Collective alignment of nanorods in thin Newtonian films. *Soft Matter* **2013,** *9* (35), 8532-8539.

157. Frka-Petesic, B.; Erglis, K.; Berret, J. K.; Cebers, A.; Dupuis, V.; Fresnais, J.; Sandre, O.; Perzynski, R., Dynamics of paramagnetic nanostructured rods under rotating field. *J Magn Magn Mater* **2011,** *323*, 1309-1313.

158. Erb, R. M.; Cherenack, K. H.; Stahel, R. E.; Libanori, R.; Kinkeldei, T.; Munzenrieder, N.; Troster, G.; Studart, A. R., Locally reinforced polymer-based composites for elastic electronics. *ACS Appl Mater Inter* **2012,** *4* (6), 2860-2864.

159. Malkina, O.; Mahfuz, H.; Sorge, K.; Rondinone, A.; Chen, J.; More, K.; Reeves, S.; Rangari, V., Magnetic alignment of SWCNTs decorated with Fe_3O_4 to enhance mechanical properties of SC-15 epoxy. *AIP Adv* **2013,** *3* (4), 042104.

160. Kazemikia, K.; Bonabi, F.; Asadpoorchallo, A.; Shokrzadeh, M., Influence of the concentration of carbon nanotubes on electrical conductivity of magnetically aligned MWCNT-polypyrrole composites. *Bull Mater Sci* **2016,** *39* (2), 457-462.

161. Studart, A. R.; Erb, R. M., Bioinspired materials that self-shape through programmed microstructures. *Soft Matter* **2014,** *10* (9), 1284-1294.

162. Libanori, R.; Erb, R. M.; Studart, A. R., Mechanics of platelet-reinforced composites assembled using mechanical and magnetic stimuli. *ACS Appl Mater Inter* **2013,** *5* (21), 10794-10805.

163. Li, D. S.; Liu, Z. Y.; Al-Haik, M.; Tehrani, M.; Murray, F.; Tannenbaum, R.; Garmestani, H., Magnetic alignment of cellulose nanowhiskers in an all-cellulose composite. *Polym Bull* **2010,** *65* (6), 635-642.

164. Moaseri, E.; Karimi, M.; Baniadam, M.; Maghrebi, M., Improvements in mechanical properties of multi-walled carbon nanotube-reinforced epoxy composites through novel magnetic-assisted method for alignment of carbon nanotubes. *Compos A-Appl Sci Manuf* **2014,** *64*, 228-233.

165. Wang, M. S.; He, L.; Zorba, S.; Yin, Y. D., Magnetically actuated liquid crystals. *Nano Lett* **2014,** *14* (7), 3966-3971.

166. Le Ferrand, H.; Bolisetty , S.; Demirors, A. F.; Libanori, R.; Studart, A. R.; Mezzenga, R., Magnetic assembly of transparent and conducting graphene-based functional composites. *Nat Commun* **2016,** *7*, 12078.

167. Ding, L.; Liu, L. P.; Li, P. G.; Lv, F. Z.; Tong, W. S.; Zhang, Y. H., Dielectric properties of graphene-iron oxide/polyimide films with oriented graphene. *J Appl Polym Sci* **2016,** *133* (12), 43041.

168. Pech-May, N. W.; Vales-Pinzon, C.; Vega-Flick, A.; Cifuentes, A.; Oleaga, A.; Salazar, A.; Alvarado-Gil, J. J., Study of the thermal properties of polyester composites loaded with oriented carbon nanofibers using the front-face flash method. *Polym Test* **2016,** *50*, 255-261.

169. Kim, K.; Ju, H.; Kim, J., Vertical particle alignment of boron nitride and silicon carbide binary filler system for thermal conductivity enhancement. *Compos Sci Technol* **2016,** *123*, 99-105.

170. Halpin, J. C.; Kardos, J. L., Halpin-tsai equations - review. *Polym Eng Sci* **1976,** *16* (5), 344-352.

171. McCrum, N. G.; Buckley, C. P.; Bucknall, C. B., *Principles of polymer engineering*. 2nd ed.; Oxford Univeristy Press: Oxford, New York, 1997.

172. Tsai, S. W.; Pagano, N. J., Invariant properties of composite materials In *Composite materials workshop*, Tsai S. W.; Halpin, J. C.; Pagano, N. J., Eds. Technomic Publishing Company: St. Louis, 1968; p 233.

173. Nielsen, L. E., *Mechanical properties of polymers and composites*. Dekker: New York, 1974; Vol. 2, p 462.

174. Fornes, T. D.; Paul, D. R., Modeling properties of nylon 6/clay nanocomposites using composite theories. *Polymer* **2003,** *44* (17), 4993-5013.

175. Broutman, L. J.; Krock, R. H., *Interfaces in polymer matrix composites*. Academic Press: New York, London, 1974; Vol. 6.

176. Chen, L.; Jin, H.; Xu, Z. W.; Shan, M. J.; Tian, X.; Yang, C. Y.; Wang, Z.; Cheng, B. W., A design of gradient interphase reinforced by silanized graphene oxide and its effect on carbon fiber/epoxy interface. *Mater Chem Phys* **2014,** *145* (1-2), 186-196.

177. Qin, W. Z.; Vautard, F.; Askeland, P.; Yu, J. R.; Drzal, L., Modifying the carbon fiber-epoxy matrix interphase with silicon dioxide nanoparticles. *RSC Adv* **2015,** *5* (4), 2457-2465.

178. Cheng, X.; Putz, K. W.; Wood, C. D.; Brinson, L. C., Characterization of local elastic modulus in confined polymer films via AFM indentation. *Macromol Rapid Comm* **2015,** *36* (4), 391-397.

179. Wang, S. Q.; Nair, S.; Hurley, D.; Lee, S. H., Characterizing interphase properties in fiber reinforced polymer composite with advanced AFM based tools. *Adv Mater Res* **2010,** *123-125*, 403-406.

CHAPTER THREE

MODIFICATION OF SIC WHISKERS WITH NICKEL NANOPARTICLES

3.1: Introduction

This chapter is devoted to the synthesis and characterization of NiNPs, the nanoparticles surface modification via polymer grafting, and the attachment of NiNPs to the surface of SiCWs using polymer-to-polymer complexation. There are several major methods for the preparation of nanoparticles[1-5]. To obtain NiNPs, we selected a chemical procedure published elsewhere[6]. This method was chosen because it yields nickel nanoparticles with no surface modifiers and of a controllable size. Thus, the surface of the NiNPs could be readily modified without further processing. To anchor NiNPs to SiCWs the particles were modified with P2VP grafted layer. To modify the surfaces, the melt state "grafting to" method was used to attach carboxyl-terminated P2VP to the SiCWs and PAA to the NiNPs[7-10]. Then, polymer-to-polymer complexation, between the basic pyridine groups of P2VP and acid carboxyl groups of PAA, was used to attach the NiNPs to the surface of the SiCWs[11]. To the best of our knowledge, the attachment of nanoparticles to SiCWs using this type of complexation has never been carried out before.

3.2: Experimental

3.2.1: The Synthesis of Nickel Nanoparticles

The prepared NiNPs were the result of four different synthesis involving the same initial formulation of reactants. In general, we followed the procedure described by Wu et al[6]. The assumed chemical mechanism of the reaction used is described in the article as follows:

$$Ni^{2+} + 6C_2H_5OH \rightarrow [Ni(C_2H_5OH)_6]^{2+} \quad (3.1)$$

$$[Ni(C_2H_5OH)_6]^{2+} + mN_2H_4 \rightarrow 6C_2H_5OH + [Ni(N_2H_4)_m]^{2+} \quad (3.2)$$

$$[Ni(N_2H_4)_m]^{2+} + 2OH^- \rightarrow Ni(OH)_2 + mN_2H_4 \quad (3.3)$$

$$2Ni(OH)_2 + N_2H_4 \rightarrow 2Ni + N_2 + 4H_2O \quad (3.4)$$

According to the authors of the article[6], a 1:5:10 molar ratio of Ni^{2+}:N_2H_2:KOH yielded the smallest NiNPs. To reproduce these results, the temperature of the solution was monitored using a thermometer in the outer water bath. The mixing of the solution was done in a closed flask either by magnetic stirring at a constant rate of 60 rpms or by sonication using a VWR Symphony™ heated sonicator. As the reaction reached completion, the color of the solution changed from bluish green to dark black[12]. The synthetic conditions employed to fabricate NiNPs are shown in Table 3.1.

Table 3.1: Synthetic conditions for NiNPs fabrication.

Synthesis of NiNPs	Temperature (°C)	Mixing technique	Time (hours)
S1	24±2	magnetic stirring	2
S2	24±2	sonication	2
S3	22 - 42	sonication	2
S4	37±4	sonication	2

S1 and S2 are the same reactions with different mixing techniques. The temperature in S3 synthesis was varied by constantly increasing it over 2 hours from 22 °C to 42 °C. Lastly, S4 was conducted at 37 °C to investigate the effect of increased temperature on the product. The obtained nanoparticles were dispersed in water and cleaned 3 times by centrifugation at 5000 RPMs for 15 min. using a Precision Durafuge 100 centrifuge and redispresing in water. Finally, the NiNPs were transferred to methanol, magnetically separated, and redispersed into fresh methanol to reduce oxidation.

3.2.2: Modification of Model Nickel Surfaces with PGMA and polyethylene glycol (PEG)

Model nickel surfaces were obtained by sputtering Ni onto a Si wafer using physical vapor deposition (PVD) technique. The obtained nickel films were cleaned by 18 W air plasma for 5 min[13]. Then, the samples were rinsed with high-purity DI water and dried in a stream of ultra-high purity nitrogen. These nickel films were dip-coated with a 3 wt. % PGMA solution in chloroform. The deposited polymer layers were dried and annealed at 120 ^{o}C for 1 hour. Then, the surface morphology and thickness of the polymer layers were evaluated by atomic force microscopy (AFM) and ellipsometry, respectively.

Next, carboxyl-terminated PEG was used as a model polymer to assess general polymer graftability to the PGMA covered nickel surface. The powder of PEG (M_w=5,000 g/mol) was deposited onto the surface modified with PGMA. PEG was grafted onto the surface in a molten state at 115^{o}C for 2 hours to anchor the polymer chains to the surface. Then, the unattached PEG was washed away by several rising cycles with chloroform. The surface morphology and thickness of the grafted layer was evaluated by AFM and ellipsometry, respectively.

3.2.3: Modification of NiNPs with PGMA, PEG, and PAA

The NiNPs were dispersed in methyl ethyl ketone (MEK) at ~0.3 wt. %. Then, this dispersion was added dropwise to a solution of 1.0 wt. % PGMA (M_n=100,000 g/mol) in MEK while being constantly sonicated with the Symphony^{TM} sonicator. The two solutions were mixed in 1:1 volume ratio. Next, the resulting solution was dried by rotary evaporation under a nitrogen stream. The dried polymer with dispersed NiNPs was

annealed at 60 ^{o}C for 30 min. The obtained PGMA-modified NiNPs were cleaned off residual PGMA three times via centrifugation and redispersing in MEK.

The PGMA-modified NiNPs were dispersed in methanol at ~0.3 wt. % and mixed with a 1.0 wt. % carboxyl-terminated PEG (M_n=5,000 g/mol) or PAA (M_w=100,000 g/mol) methanol solution that was sonicated with the Symphony^{TM} sonicator. The two solutions were mixed in a 1:1 volume ratio. This resulting solution was rotary evaporated under a nitrogen stream and annealed at 120 ^{o}C for 30 min. for the PAA/NiNPs system and 115 ^{o}C for 2 hours for the PEG/NiNPs system. The PAA and PEG modified NiNPs were cleaned 3 times via centrifugation and redispersing in methanol. The PEG-modified NiNPs were analyzed by TEM and TGA.

3.2.4: Thermal Cleaning of SiCWs

The Silar SC-9M, silicon carbide whiskers were purchased from Advanced Composite Materials, LLC. These industrial grade SiCWs were analyzed by TGA to estimate their purity. As silicon carbide is known for being stable up to 1000 ^{o}C in air[14], the weight loss of the SiCWs was used to measure the amount of processing impurities in the supplied SiCWs. As a standard practice, the TGA was run at 20 ^{o}C/min to 700 ^{o}C in air. An example of the TGA trace is shown in Figure 3.1.

The weight reduction of the sample observed below 500 ^{o}C was assigned to the reaction of processing impurities with air. The composition of the impurities was not characterized. However, silicon carbide is known to accumulate oxygen and free carbon on its surface[14]. These surface impurities caused a 0.2 wt. % weight loss at 500 ^{o}C. As a

result of these findings, the temperature of 400 ^{o}C was chosen to clean the SiCWs by burning off any of the possible impurities in air.

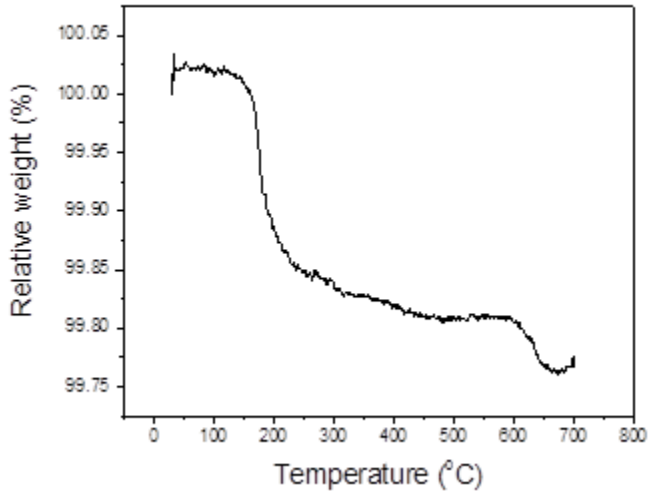

Figure 3.1: TGA of as-received SiCWs.

Typically, 1 g of the SiCWs was cleaned at a time. First, the SiCWs were placed into a non-glazed ceramic porcelain crucible (stable until 1200 ^{o}C). Next, the crucible with the SiCWs was placed into the center of a Lindberg/Blue 1000 ^{o}C ceramic lined oven with a Eurotherm 2416 temperature controller. The oven was then heated to 400 ^{o}C in 20 min. and held at 400 ^{o}C for one hour. Then, the oven was cooled down to room temperature at ~3 ^{o}C/min. in air at atmospheric pressure. The controlled heating and cooling rate were used to reduce residual thermal stresses in the SiCWs. After this thermal cleaning, the SiCWs were again tested for impurities using TGA. The TGA was run in air at 20 ^{o}C/min to 700 ^{o}C (Figure 3.2). The cleaned SiCWs had a minute weight gain of 0.02 wt. % by 700 ^{o}C.

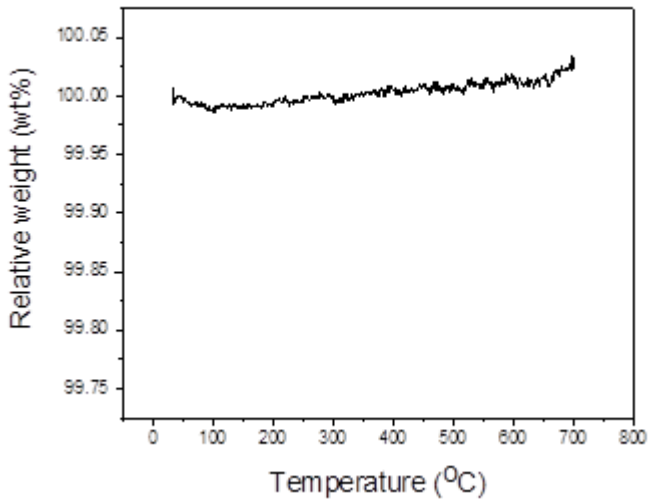

Figure 3.2: TGA of thermally cleaned SiCWs.

The thermal cleaning treatment was instrumental in clearing the surface off impurities and making the surface functional groups available for further modification. A SEM image was obtained to show the appearance of the cleaned SICWs (Figure 3.3).

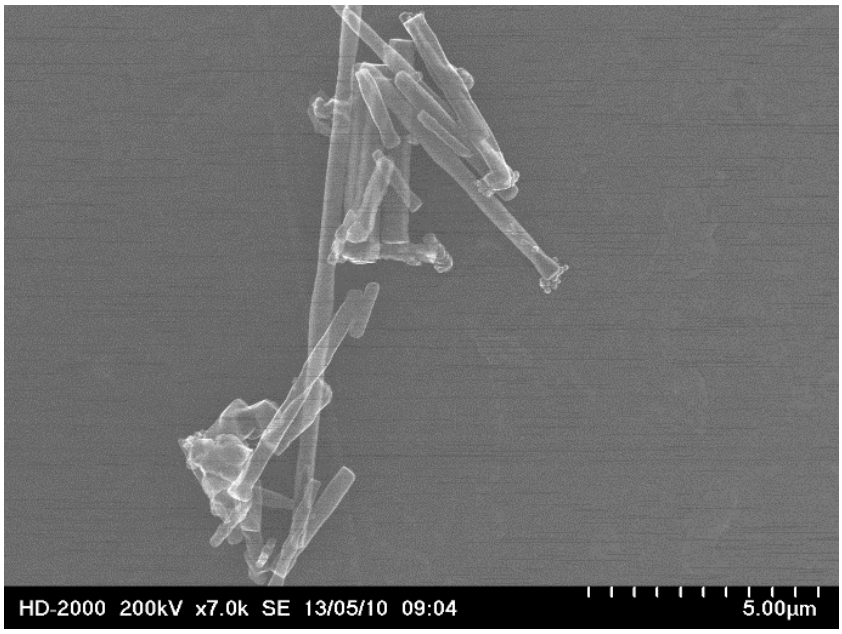

Figure 3.3: SEM image of the thermally cleaned SiCWs.

3.2.5: Size Separation of SiCWs

The size separation of the industrially manufactured SiCWs was carried out to reduce the possibility of defects in the composite caused by agglomerates and small particulates. Agglomerations introduce packed assemblies that resin cannot penetrate during fabrication. Small particulates are structural defects that considerably decrease the stress transfer due to their low aspect ratio.

To separate the two unwanted phases from the rest of the SiCW material, combination of gravity sedimentation and centrifugation was used. First, gravity sedimentation was utilized to separate SiCWs agglomerates. Acetone was chosen as the liquid media for the sedimentation, because stable dispersion of SiCWs could be obtained in this solvent. The working concentration of the whiskers was chosen by comparing the suspensions' color change over time. Suspensions of 2, 4, and 8 wt. % were initially evaluated. The 2 wt. % suspension held its color for the longest time and was used for further separation procedures. The suspension of 2 wt. % of SiCWs in 40 ml of acetone was sonicated for 15 min. Then, the 40 ml centrifugation tubes containing the dispersed SiCWs were shaken vigorously and placed standing straight up for 20 s. Afterwards, the top portion of the suspension was pipetted off until 10 ml of suspension was left. This procedure was repeated three more times, producing 90 ml of suspension.

After the gravity sedimentation, a centrifugation separation process was employed to remove small particulates. They were identified by their inability to sediment during centrifugation from a methanol suspension. Thus, the SiCWs were dispersed in methanol and centrifuged at 5000 rpms for 15 min. The sediment was kept, but the top solution was

decanted. This centrifugation process was repeated between three to six times before a clear methanol layer above the sediment of the whiskers was achieved. The separation procedure was identical for all batches of the SiCWs used in this work. The obtained whiskers were imaged by SEM and found to have diameters in the range of 0.2–0.6 μm (0.42 μm average) and lengths from 2 to16 μm (4.2 μm average).

3.2.6: "Grafting to" of PGMA and P2VP to the Silicon Wafer Surface

The silicon wafers were cleaned using a "piranha" solution (1 vol. part of 30 wt. % solution of hydrogen peroxide and 3 vol. parts of concentrated sulfuric acid) and washed with deionized (DI) water[13]. Next, the cleaned silicon wafers were dip-coated in a 3 wt. % solution of PGMA (M_w=100,000 g/mol) in acetone. The thin polymer layer of PGMA was dried and annealed at 60 ^oC for 1 hour in a vacuum oven. Then, the wafer was cleaned three times by washing it in acetone and dried under a stream of nitrogen. The layer thickness and morphology were determined by ellipsometry and AFM, respectively.

Next, a 1 wt% solution of P2VP (M_w=53,000 g/mol) in MEK was dip-coated onto the surface of the PGMA-modified silicon wafer. The polymer films were annealed at 115 ^oC overnight in a vacuum oven. The excess P2VP was removed by rinsing with MEK three times. The surface thickness and morphology were determined by ellipsometry and AFM, respectively.

3.2.7: "Grafting to" of PGMA and P2VP to SiCWs

The SiCWs were dispersed in acetone at ~0.1 wt. %. Then, this dispersion was added dropwise to a 1.0 wt. % solution of PGMA (M_w=100,000 g/mol) in acetone. The

solutions were mixed in 1:1 volume ratio while being sonicated with the Symphony™ sonicator. The resulting suspension was dried by rotary evaporation under a stream of nitrogen and annealed at 60 °C for 1 hour. The PGMA-modified SiCWs were then cleaned three times by centrifugation and redispersing in acetone.

Next, the PGMA-modified SiCWs were dispersed in MEK at ~0.1 wt. %. The SiCWs dispersion in MEK were added dropwise to a sonicated 1.0 wt. % solution of carboxyl-terminated P2VP (M_w=53,000 g/mol) and MEK. The two solutions were added in a 1:1 volume ratio. Then, the MEK was rotary evaporated under a stream of nitrogen and the resulting film was annealed at 115 °C for 24 hours. These P2VP-modified SiCWs were cleaned three times in MEK by centrifugation and redispersing in the fresh solvent and transferred to methanol.

3.2.8: Modification of Silicon Wafers with Epoxy Silane and P2VP

A silicon wafer was cleaned using "piranha" solution and washed with DI water. Then, the cleaned silicon wafer was placed into a 5 wt. % solution of epoxy silane ((3-glycidyloxypropyl) trimethoxysilane), ES in toluene for 24 hours while being shaken gently. During this process the epoxy silane was anchored to the wafer's surface[15]. This modified surface was rinsed with toluene and methanol prior to starting the P2VP grafting process.

The epoxy silane-covered silicon wafers were dip-coated in a 2 wt. % solution of P2VP in MEK. The obtained polymer film was annealed at 115 °C overnight in a vacuum oven. Then, the excess P2VP was rinsed off with the solvent three to four times. The

thickness and surface morphology of the polymer and epoxy silane films were determined using ellipsometry and AFM, respectively.

3.2.9: Modification of SiCWs with Epoxy Silane and P2VP

The modification of SiCWs was conducted using the ES solution in toluene. Namely, 1 wt% suspension of SiCWs in toluene was added dropwise to a 5 wt% ES solution to reach a 1:1 ES/SiCW ratio by weight. The mixture was shaken for 24 h. Then, the SiCWs were centrifuged and rinsed with toluene and methanol three times each to remove any unattached silane. Afterwards, modified SiCWs were transferred to methyl ethyl ketone (MEK) purchased from Acros Organics.

The epoxy silane covered SiCWs were dispersed in MEK at ~0.2 wt. % and then added dropwise into a 2 wt. % solution of the P2VP in MEK. The dispersion and the solution were mixed in a 1:1 volume ratio. Then, the mixture was dried under nitrogen using rotary evaporator. The P2VP/SiCWs system was annealed at 115 ^{o}C for 24 hours in a vacuum oven. Then, the excess P2VP was removed from the SiCWs by centrifuging and redispersing the whiskers in MEK three times. The morphology and thickness of the polymer layer were determined by TEM and TGA, respectively.

3.2.10: Modification of SiC Whiskers with Magnetic NiNPs

After the surface modification of the NiNPs and SiCWs was completed, the NiNPs were attached to the SiCWs using polymer-polymer complexation. The NiNPs modified with PAA and the SiCWs covered with P2VP were dispersed in methanol to obtain a 5 mg/ml and 10 mg/ml suspensions, respectively. The NiNP suspension was sonicated for 15 min. Then, the suspension of SiCWs was added dropwise to the NiNP suspension while

sonicating over a 15 min. period of time. The mixture was shaken for 24 hours and, then, separated using gravity sedimentation.

3.2.11: TGA Measurements

TGA was used to determine the weight loss associated with the attached polymer. The PGMA modified SiCWs were heated at 7 ^{o}C/min to 700 ^{o}C in air. The modified NiNPs and SiCWs were heated at 7 ^{o}C/min and 20 ^{o}C/min to 600 ^{o}C in air; 7 ^{o}C/min was chosen to maximize the amount of degradation at a specific temperature, and 20 ^{o}C/min was chosen as a secondary method of measurement.

3.2.12: Procedure for the Calculation of Polymer Thickness from TGA Data

The thickness of polymer bound to the surface of the particulates is directly related to the amount of weight loss in the TGA experiment and depends on the surface area of the particulates. It was assumed that the polymer is uniformly distributed across the surface of the particulates. Equation 3.5 and 3.6 were used to calculate the thickness (t) of the polymer attached to the cylindrical (whiskers) and spherical (particles) nanoparticulates, respectively. These equations are derived from geometrical considerations.

$$t = R_{np}\left(\sqrt{1+\frac{M_p\rho_{np}}{M_{np}\rho_p}}-1\right) \qquad (3.5)$$

$$t = R_{np}\left(\sqrt[3]{1+\frac{M_p\rho_{np}}{M_{np}\rho_p}}-1\right) \qquad (3.6)$$

where R_{np} is the radius of the nanoparticulate (whisker or nanoparticle), ρ_{np} and ρ_p are the densities of the nanoparticulates and polymer, M_p and M_{np} are the weight fractions for the polymer and nanoparticulates as indicated by TGA, respectively.

3.2.13: TEM Imaging of the Nanoparticulates

The NiNPs, polymer-modified NiNPs, SiCWs, polymer-modified SiCWs, and SiCWs modified with NiNP were dispersed in methanol at ~0.5 wt. % and drop-casted onto an Formvar/carbon TEM grid. Then, the particles were imaged employing a Hitachi 7600 TEM operated in a high-resolution mode. Using the Hitachi HD2000, the particulates were imaged with Z-contrast, scanning, and transmission modes.

3.2.14: XRD Measurements

The NiNPs' crystal structure was determined using an Ultima IV, Rigaku Corp. XRD. 0.015 g of the NiNPs dispersed in methanol were drop-casted onto a 1" diameter glass slide and dried overnight. The glass slide was then placed into an aluminum sample holder and the diffraction pattern was collected from 30^{o} to 90^{o} at 40 kV beam intensity and scan speed of 0.55 deg./min..

3.2.15: Magnetic Measurements

The NiNPs magnetic properties were measured using MicroMag Magnetometer, Cambridge Measurements Corp. The NiNP dispersion was dried and 3–5 mg of nanoparticles were casted into an adhesive tape. The tape was attached to the magnetometer's probe holder using a silicone gel. Then, the magnetization curves were collected from 400 to -400 A/m at scan speed of 12.5 A/m/min.

3.3: Results and Discussion

3.3.1: Synthesis and Modification of Nickel Nanoparticles

Synthesis of NiNPs

During the formation of nanoparticulates, the increase in temperature will increase the reaction rate and decrease the nucleation rate[16]. Consequently, the temperature of the NiNPs synthesis was varied to find a compromise between the nucleation and growth rates to synthesize the NiNPs with required diameter. Another factor significantly influencing the formation of NiNPs is the agitation of the reaction media. In turn, the sonication and magnetic stirring were used to vary the particle size. These methods have different intensity of agitation to break up nickel hydroxide into small particulates for the reduction process. Specific conditions for the synthetic procedure are outlined in Table 3.1.

The size of the particles synthesized in S1, S2, S3, and S4 synthetic procedures were determined from SEM images using Gwyddion image processing software; the sizes of 60–70 nanoparticles were measured manually for each synthesis.

As shown in Figure 3.4, S1, S2, S3, and S4 had rather large size distribution, as denoted by the standard deviations of the diameter values. The sonicated solutions, in general, yielded smaller nanoparticles. S3 had the smallest nanoparticles with an average diameter of 60 nm, which is 10 nm smaller than the next closest value. S1 resulted in the largest synthesized nanoparticles. The nanoparticles processed in S1 were analyzed in more detail by SEM, XRD, and magnetometry (Figure 3.5).

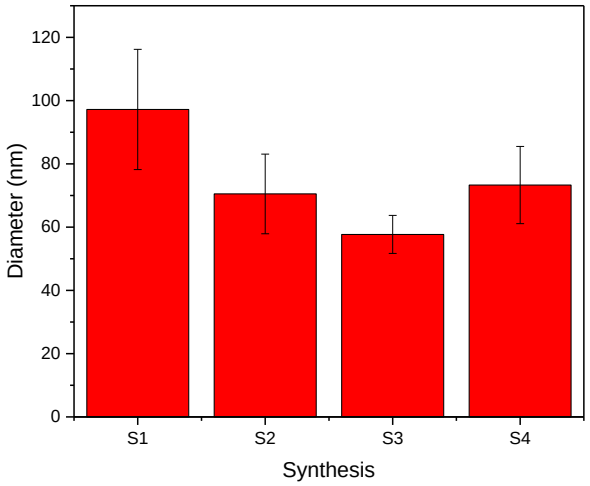

Figure 3.4: The measured diameters of the synthesized NiNPs.

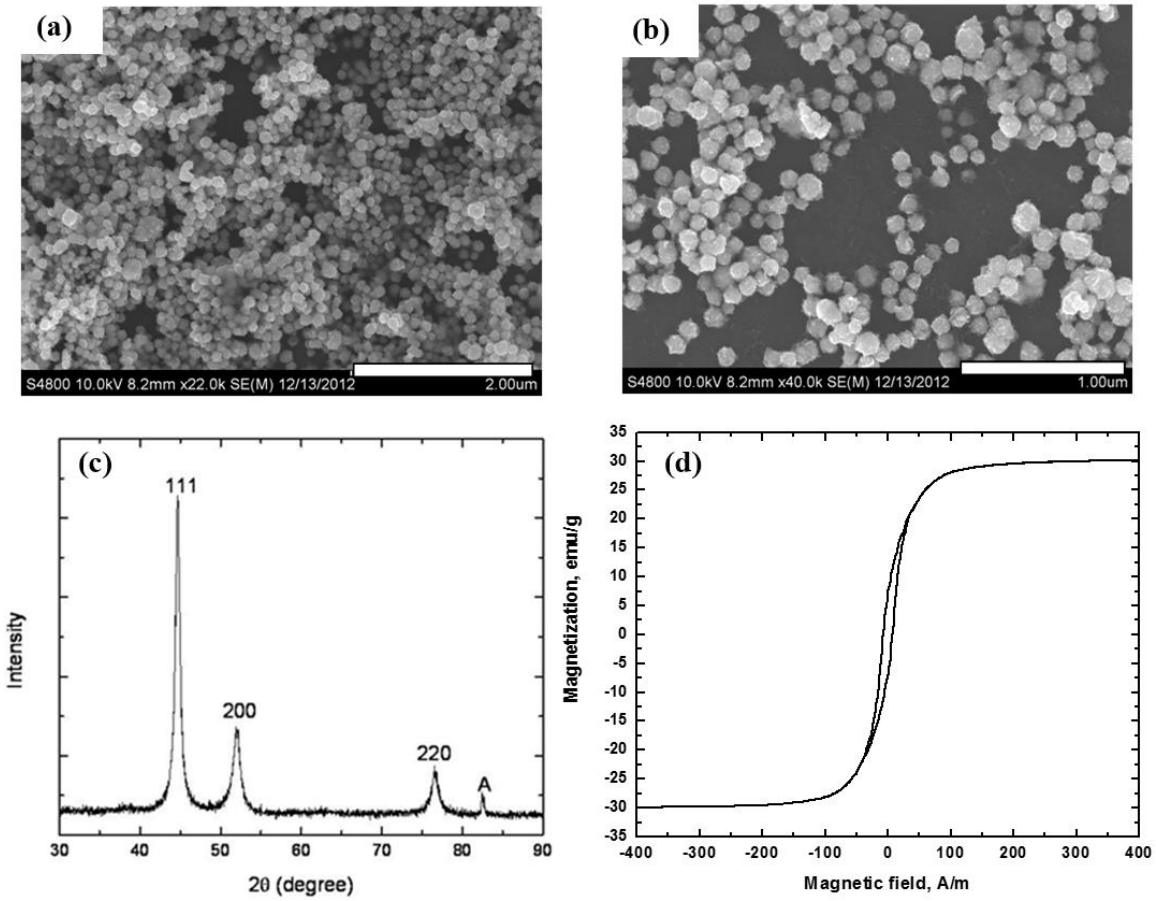

Figure 3.5: (a, b) SEM images, (c) XRD pattern and (d) magnetization curve of the S1 synthesized NiNPs.

The synthesized particles were nearly spherical with a 100 ± 20 nm diameter (Figures 3.5a and b). The particles' surface was quite rough, as typically found for the NiNPs obtained via the reduction process [6]. The XRD pattern indicated the presence of a single fcc crystal phase with three characteristic peaks ($2\theta = 44.6^{o}, 52.0^{o}, 76.5^{o}$) (Figure 3.5c) corresponding to pure metallic nickel[17]. No nickel oxide was detected within the XRD detection limit. Considering the detection limit for this XRD is a few percent for mixtures[18], ~1–2 nm of an oxide layer for 100 nm particles might be present on the surface of the nanoparticles. A film of such thickness can be attributed to a natural oxide layer typically formed on the nanoparticles' surface. The absence of the nickel oxide in the XRD pattern suggests that no additional nickel oxide (aside from the one naturally formed on the surface) is present in the synthesized particles.

Magnetic measurements (Figure 3.5d) confirmed the ferromagnetic nature of the material with the saturation magnetization of approximately 30 emu/g, remnant magnetization of 7.1 emu/g, and coercivity of 90 Oe. These results differ from bulk Ni[19], but are similar to the results reported for NiNPs[6, 20].

The particles obtained from the different synthesis were used in different experiments. The S1 nanoparticles were utilized to study the "grafting to" surface modification. Although the NiNPs obtained with S1 synthesis were not of the targeted size for the project, they provided a model surface to demonstrate the concept of grafting to nanoparticulates. The smallest nanoparticles (S3) were chosen to magnetically modify the SiCWs because they could provide the highest packing density on the surface. Therefore, the S3 synthesis was chosen to be used to functionalize the whiskers.

Modification of NiNPs' Surface

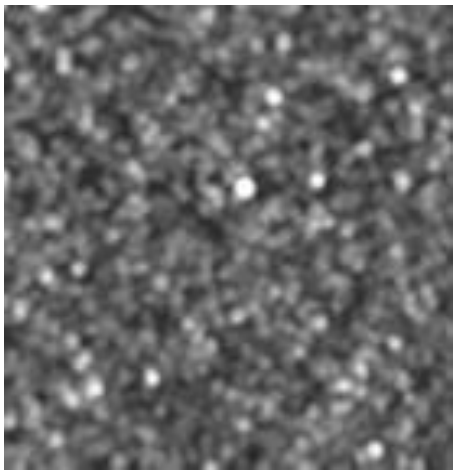

Figure 3.6: AFM topography image of the as deposited nickel film. The image size is 0.8x0.8 μm^2. The vertical scale is 5 nm.

Preliminary studies were used to prove that the Ni surface could be uniformly modified via polymer grafting. For this purpose single crystal silicon wafers were sputtered with nickel to produce a 100 ± 10 nm film, as described in the dissertation by Galabura[13]. Figure 3.6 is an AFM image showing the surface morphology of the as deposited nickel film. The AFM images revealed that the silicon wafer surface was uniformly covered by nickel. These nickel films were cleaned and activated with plasma and then dip coated in a PGMA solution in chloroform. The PGMA films were annealed and rinsed to obtain a 6–7 nm layer on the nickel substrate (Figure 3.7a). The process of grafting is described in detail elsewhere[13, 21]. The PGMA layer acts as the anchoring layer for the end carboxyl groups of the PEG. In fact, the grafting of the PEG resulted in a film with a thickness of 13 ± 1 nm (Figure 3.7). The AFM images revealed uniform coverage of the surface by both the PGMA and PEG. The increase in the polymer film thickness and change in morphology confirmed the grafting of PEG to the nickel substrate.

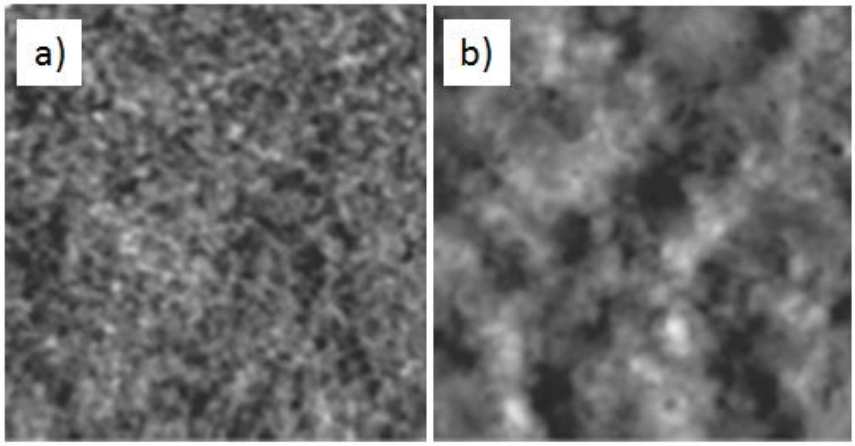

Figure 3.7: AFM topography image of the grafted (a) PGMA and (b) PEG films on the nickel substrate. The image size is 0.8x0.8 μm^2. The vertical scale is (a) 5 nm and (b) 20 nm.

Modification of NiNPs by Grafting of PGMA and PEG

Using the developed grafting procedures, PGMA and PEG were effectively anchored to the surface of NiNPs. First, the bare NiNPs (Figure 3.8a) were grafted with PGMA. The grafted PGMA layer (Figure 3.8b) was measured to be approximately 1–2 nm. Lastly, the PEG was grafted to the surface creating a 10–12 nm polymer shell (Figure 3.8c). These TEM images confirm that PGMA and PEG can be grafted to the NiNPs.

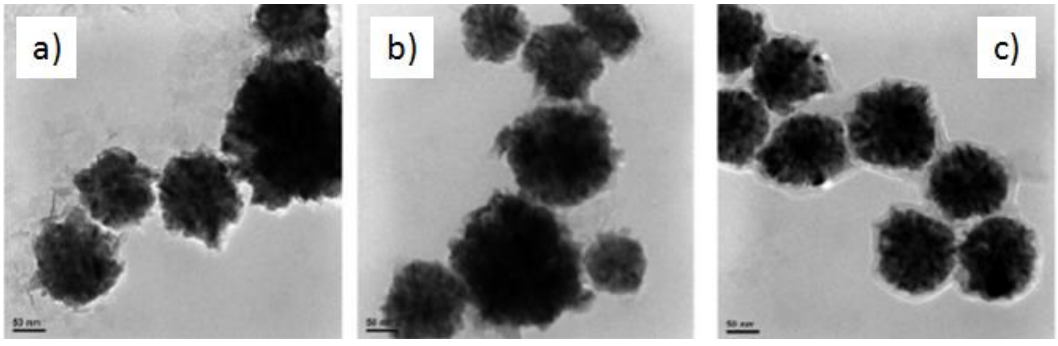

Figure 3.8: TEM images of NiNPs at various stages of the modification process: (a) bare NiNPs, (b) PGMA-modified NiNPs, and (c) PEG-modified NiNPs. The scale bar is 50 nm.

Additionally, the end-terminated PEG demonstrated the effectiveness of carboxylic acid to epoxy anchoring of functionalized macromolecules.

Grafting of PAA to PGMA anchored to NiNPs

The developed grafting procedures were used to covalently bond PAA to the surface of the NiNPs. PAA was chosen to modify the nanoparticles due to the carboxylic acid groups reactivity with epoxy and ability to complex with other polymers. Thus, the NiNPs were mixed, dried, and cured in bulk PGMA. The PGMA modified NiNPs were dispersed into a concentrated solution of PAA in methanol. This solution was dried and annealed to create a film of PAA covalently bonded to the surface of the NiNPs.

Figure 3.9 is an image of the NiNPs with grafted PAA on the surface. This image reveals the thickness of the grafted layer on the level of 10 ± 9 nm. The thickness was calculated from the average film thickness of ~65 particles. A sample of the PAA-modified

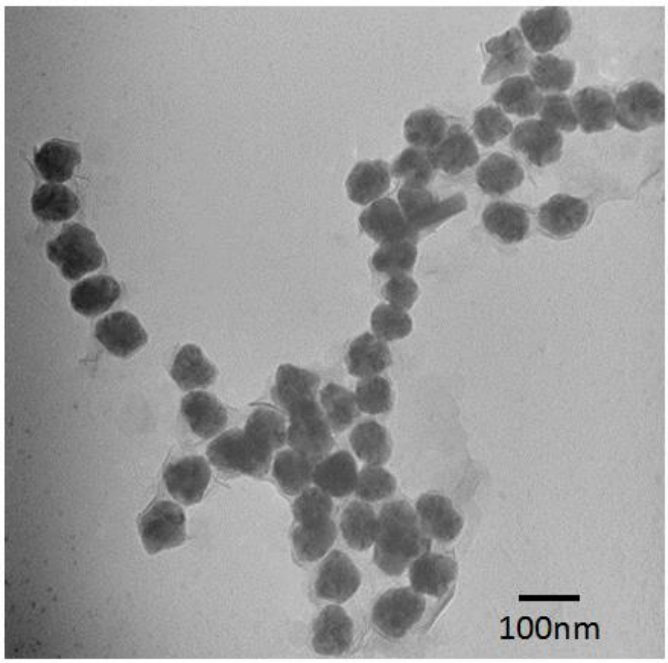

Figure 3.9: TEM image of NiNPs modified with PGMA and PAA.

NiNPs was also analyzed with TGA to estimate the grafting thickness by weight loss. The TGA results indicated a weight loss of 33.4 %. Using Equation 3.6 (density of the polymer is assumed to be 1 g/cm^3), the PAA film thickness was calculated to be 23 nm (2.3 times larger than the TEM results). Thus, the bulk sample has a large variation in the polymer grafting thickness and/or shape and size variation of particulates. However, since the layer of PAA was anchored to the surface of the NiNPs successfully, these modified NiNPs were used in further experimentation to evaluate their ability to attach to SiCWs modified with P2VP.

3.3.2: Modification of SiCWs

Modification of Silicon Wafers with Grafted PGMA and P2VP

The modification of a silicon wafer with carboxyl-terminated P2VP using a PGMA anchoring layer was done to prove that nanofilms could be produced with the polymer grafting. The silicon wafer provides a natural silica oxide layer that represents the surface of the SiCWs. The analysis of the AFM image of the PGMA-grafted surface presented in Figure 3.10a, shows that the layer has a root mean square (RMS) AFM roughness of 1.4 nm. Additionally, ellipsometry thickness measurements resulted in an average layer height of 5 ± 1 nm (averaged from 10 samples). Next, P2VP was grafted to the PGMA-modified silicon wafer (Figure 3.10b). The grafted P2VP film thickness was measured by ellipsometry to be 15.0 ± 0.7 nm (averaged from 10 samples). The uniformity of the grafted P2VP film was confirmed using AFM. From the AFM image, the RMS roughness was measured to be 1.7 nm (Figure 3.10b). The modification of the model surfaces, shown in

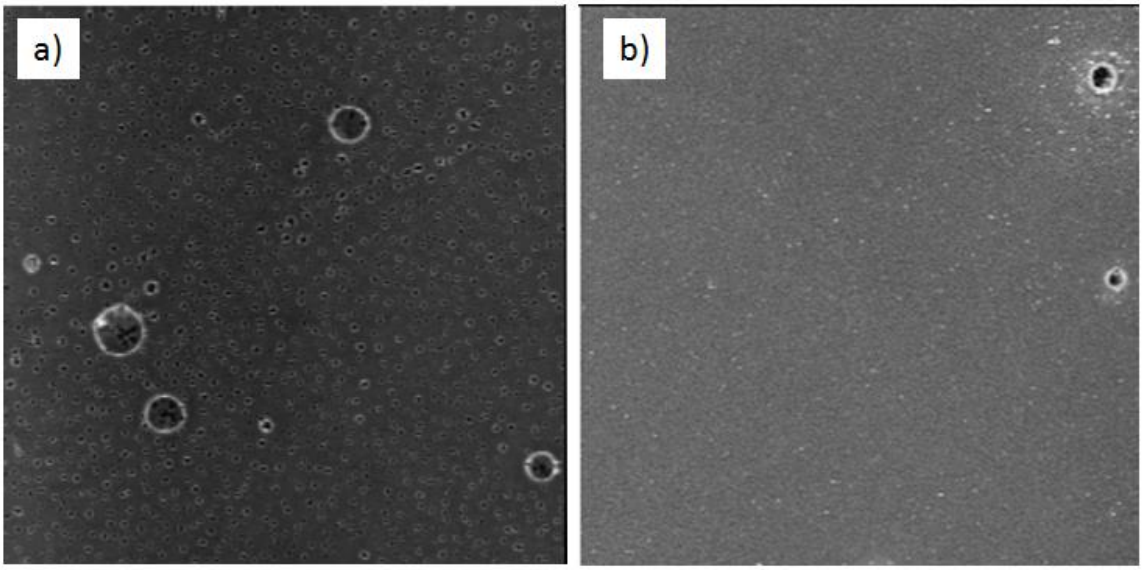

Figure 3.10: AFM topography images of the grafted (a) PGMA and (b) P2VP. The images size is 10x10 μm^2. The vertical scale is (a) 25 nm and (b) 40 nm. (The craters in the PGMA film are related to high humidity causing water condensation during the film drying).

Figure 3.10a and b, was successful at producing a uniform P2VP-grafted layer onto the silicon surface and the methodology used could be transferred to the SiCWs.

Surface Modification of SiCWs by the Grafting of P2VP via PGMA Layer

The SiCWs were modified with PGMA and carboxyl-terminated P2VP by the "grafting to" technique to create a P2VP polymer film on the whiskers' surface (Figure 3.11). TEM was used to investigate the thickness of the PGMA-layer grafted to the SiCWs. At first glance, the PGMA appeared to be grafted as a layer with thickness of several nanometers (Figure 3.11a). However, it was found that some of the SiCWs were not modified individually (Figure 3.11b). Namely, PGMA bridging between SiCWs was observed. Therefore, TGA was used to determine the average polymer thickness on the SiCWs (Figure 3.12) to evaluate the degree of bridging

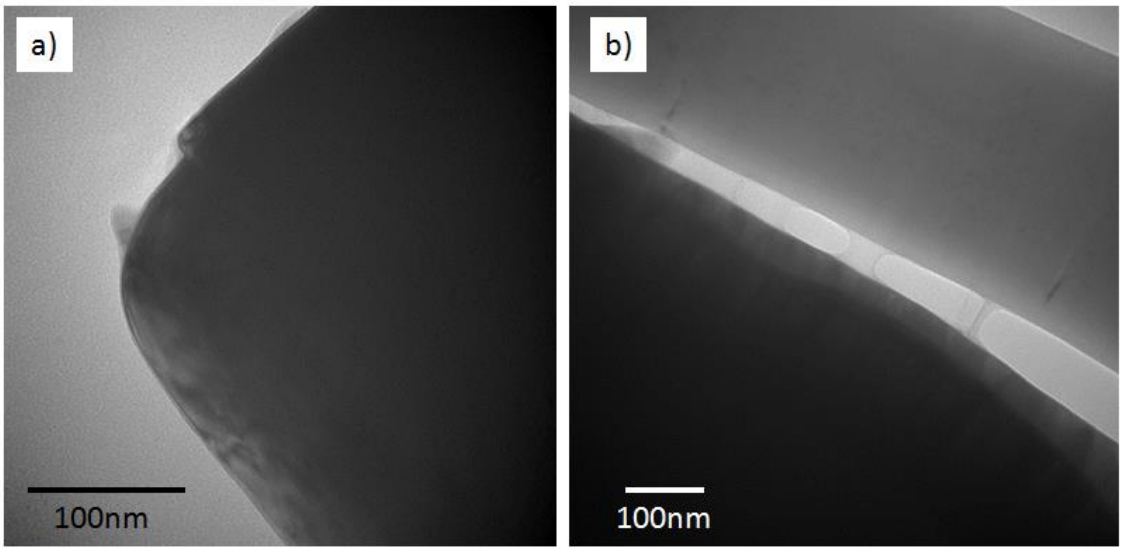

Figure 3.11: TEM images of a SiCW modified with the PGMA layer: (a) the end of a SiCW (the film is barely visible); (b) the bridging of the PGMA layers between two SiCWs.

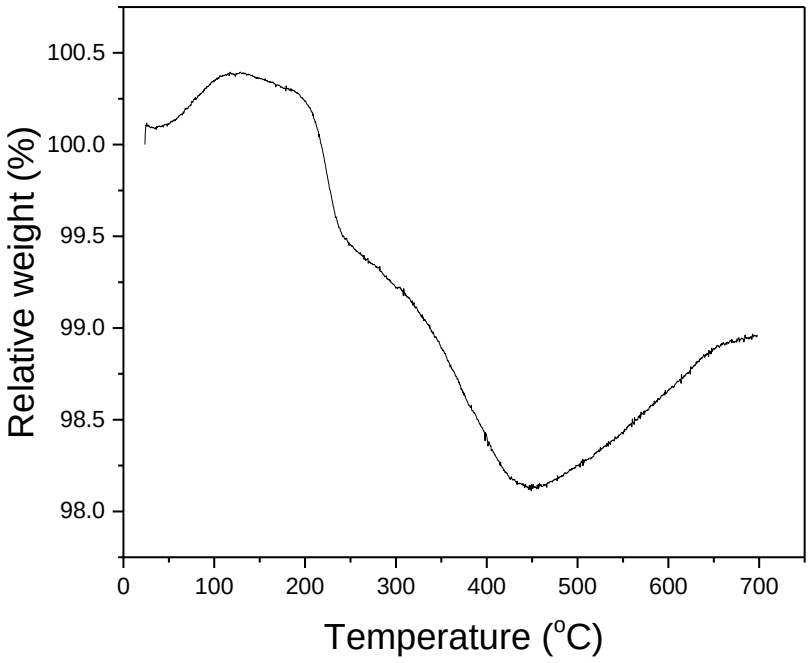

.

Figure 3.12: TGA curve of PGMA-modified SiCWs.

It was observed that the modified SiCWs had a 1.9 % weight loss up to 450 °C. Using Equation 3.5 (assumed density of the polymer was 1 g/cm^3) the polymer thickness

of the layer was found to be ~7 nm. This was just 1–2 nm different from the model silicon wafer system, indicating that the bridging of the whiskers by the PGMA is not a prevailing phenomenon. Therefore, it was assumed that the PGMA bridging would not affect the next modification with carboxyl-terminated P2VP.

Figure 3.13 is a TEM image of the P2VP grafted to SiCWs. From TEM imaging it was concluded that P2VP layer was grafted to the SiCWs surface and has thickness of

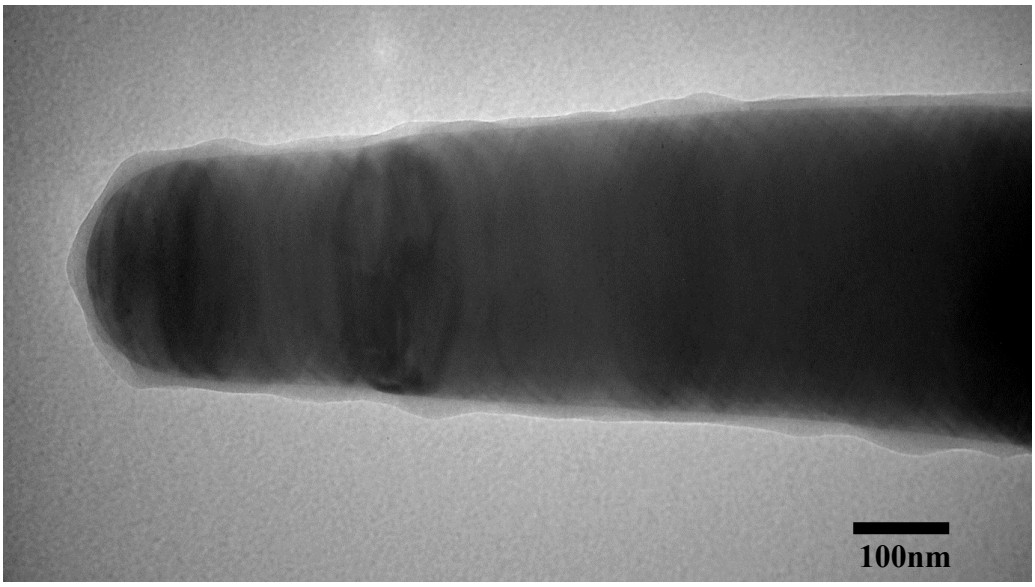

Figure 3.13: TEM image of a SiCW modified with carboxyl-terminated P2VP.

about 12±5 nm (averaged over 10 whiskers). These results were comparable to the modification of the model surface. Thus, the presence of the surface curvature did not influence the grafting of the polymer. However, the results of the TGA analysis did not complement the TEM image analysis (Figure 3.14).

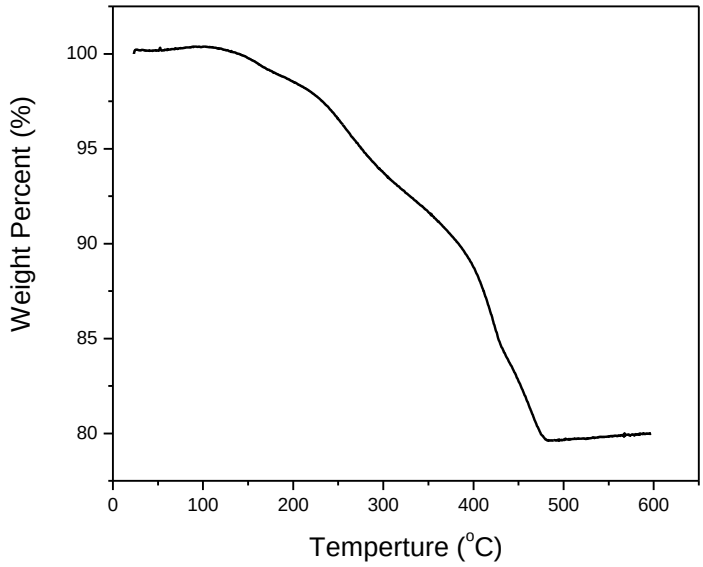

Figure 3.14: TGA curve for the P2VP-modified SiCWs.

In fact, the modified SiCWs lost about 20 wt. % of the sample, which calculates to approximately 70 nm of combined (PGMA and P2VP) polymer layer grafted to the surface (Equation 3.5, polymer density-1 g/cm^3). It results in 63 nm of P2VP after subtracting PGMA contribution (7 nm). This is approximately 5.3 times larger than the measured film in the Figure 3.13 and 4.2 times larger than the results for the model surface. These TGA results indicate that bridging and non-uniform grafting of PGMA can have a significant effect on the polymer grafting and cannot be ignored. Indeed, the extent of bridging was found, with additional TEM imaging, to be excessive (Figure 3.15).

The circles in the TEM image, for both Figure 3.15a and b, are used to highlight the regions of bridging between the SiCWs. The polymer is seen to be spanning gaps of up to several hundred nanometers between the whiskers. These results were used to conclude that PGMA is not suitable for the surface modification of SiCWs in the experimental

conditions used. Thus, a low molecular weight surface modifier (epoxy silane) was utilized in the fabrication of uniformly coated surfaces.

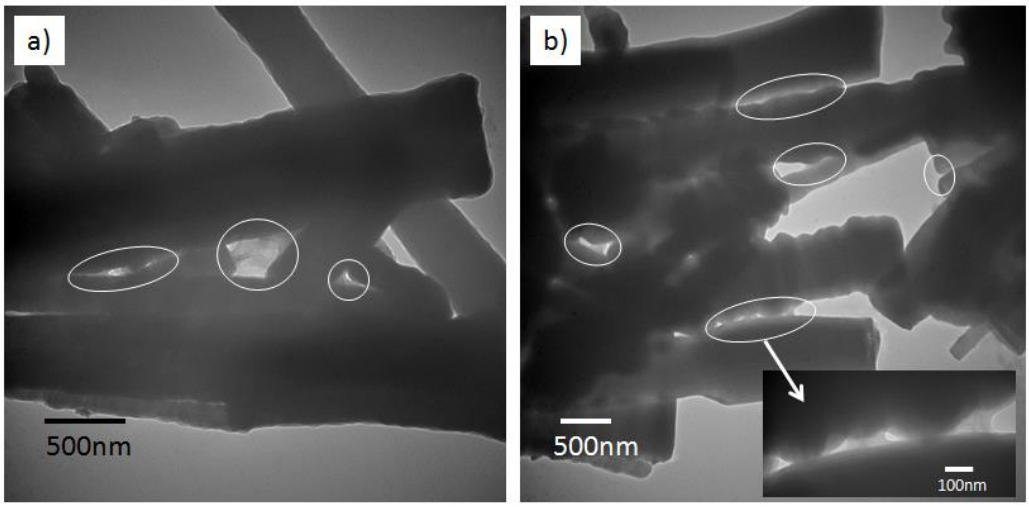

Figure 3.15: Additional TEM images of SiCWs modified with PGMA and P2VP

Surface Modification of SiCWs with an Epoxy Silane and P2VP

Surface modification of inorganic materials with epoxy silane is well established surface modification procedure to cover inorganic materials with reactive epoxy groups[7-8, 22]. Initially, model surfaces (silicon wafers) were used to verify the modification procedure. The epoxy silane was deposited onto the surface of the wafer from a toluene solution. The ellipsometry measurements indicated a deposition of 3.0 ± 0.5 nm thick epoxy silane film. Additionally, the AFM images indicated that, indeed, uniform epoxy silane layer with RMS roughness of 1.3 nm was fabricated (Figure 3.16a). The thickness of the grafted P2VP film was determined to be 9.0 ± 0.4 nm using ellipsometry. Then, AFM imaging was used to evaluate the uniformity of the film (Figure 3.16b). It was found that the grafted layer covers the surface of the wafer uniformly and has RMS roughness of

less than 1 nm. Since, the modification of the model surface with epoxy silane and P2VP was successful we used this methodology for modification of SiCWs.

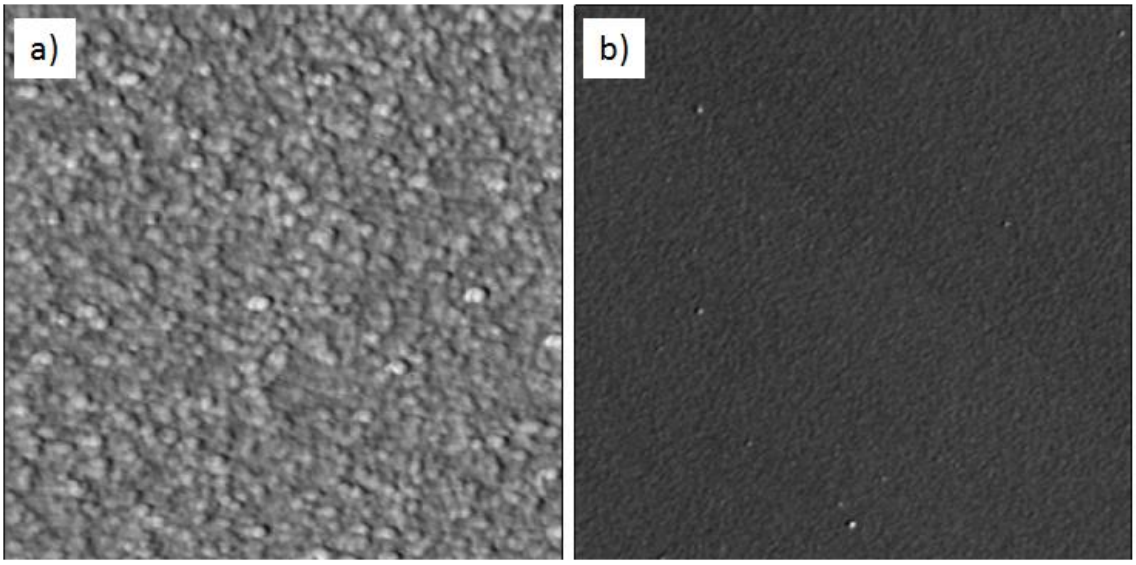

Figure 3.16: AFM topography image of (a) the epoxy silane layer (1 x 1 μm^2) and (b) grafted P2VP polymer film (10 x 10 μm^2). The vertical scale is 10 nm.

Modification of SiCWs with Epoxy Silane and P2VP

The SiCWs were modified with the epoxy silane from a solution in toluene. The resulting modified SiCWs were analyzed by TGA (Figure 3.17-3.18). The weight loss associated with of the epoxy silane was ~2 wt. %. With a density of 1.1 g/cm^3 assuming uniform coverage of the average SiCW, the epoxy silane film thickness was calculated to be 6 nm (using Equation 3.5). This is approximately the same thickness of the epoxy silane as was found on the silicon wafer. The epoxy silane-modified SiCWs were further processed by grafting the carboxyl-terminated P2VP. The thickness of the P2VP was determined using TGA and TEM. First, TGA was used to determine the weight loss

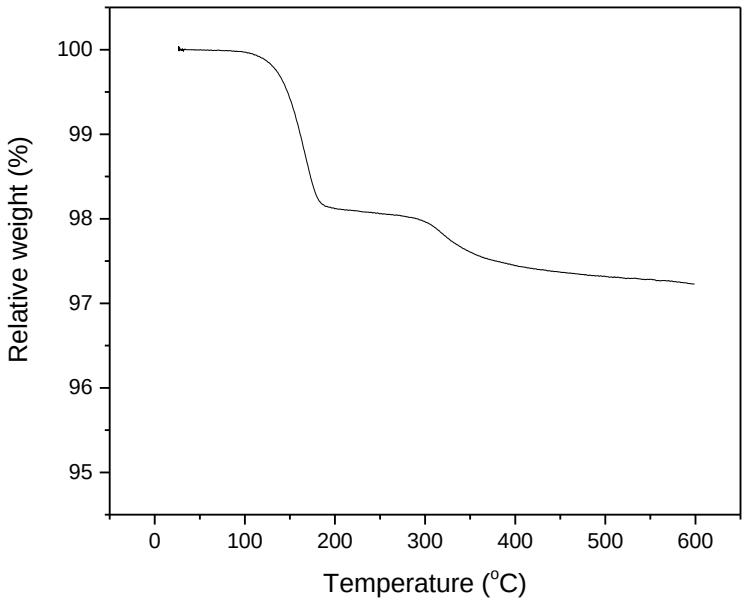

Figure 3.17: TGA curve for the SiCWs modified with epoxy silane

associated with decomposition of the polymer (Figure 3.18). The P2VP-modified SiCWs lost ~2 wt, % of the polymer, which calculated to be 6 nm of grafted polymer (using Equation 3.5). TEM image (Figure 3.19) reveals uniform polymer surface coverage

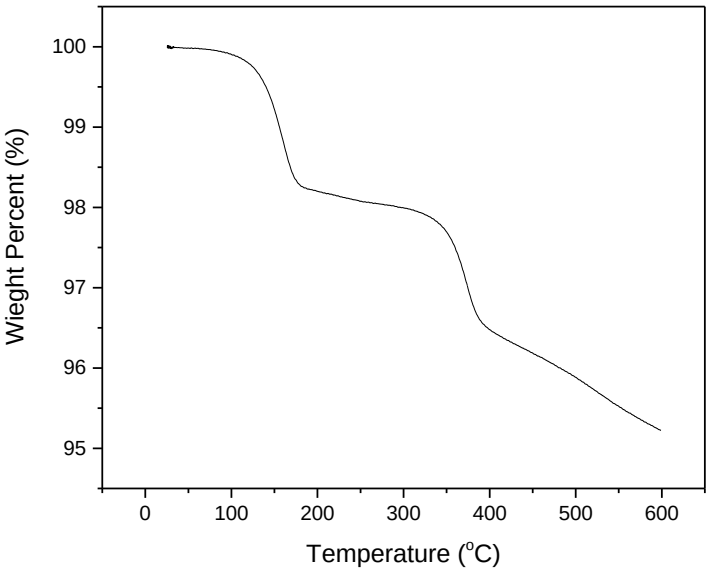

Figure 3.18: TGA curve for the SiCWs modified with P2VP via epoxy silane.
without bridging.

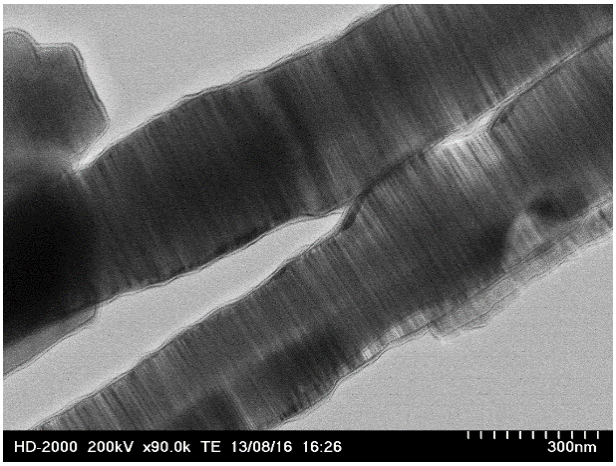

Figure 3.19: TEM image of the SiCWs modified with epoxy silane and P2VP.

Indeed, with a very thorough search throughout the entire sample, no noticeable bridging of the polymer layers was found. The image shown in Figure 3.19 was presumed to be a representative image of the P2VP modified SiCWs. The thickness of the polymer layer in Figure 3.19 is two times higher than the one obtained from TGA and 4 nm thicker than the polymer film grafted to the model silicon wafer. In general, the results prove that the silane-based modification is suitable methodology for the polymer grafting to SiCWs.

3.3.3: Modification of SiCWs with NiNPs

After attaching PAA and P2VP to the surface of NiNPs and SiCWs, respectively, the attachment of the NiNPs to the SiCWs was accomplished using the polymer-to-polymer complexation between PAA and P2VP[23-24]. In general, we foresee that the complexation approach could potentially serve as a universal modification technique to attach magnetic nanoparticulates. The complexation methodology for the magnetic functionalization of the SiCWs with NiNPs was successful to the large extent. However, we found that only a small number of NiNPs was attached to the surface of the SiCWs (Figure 3.20). The whiskers

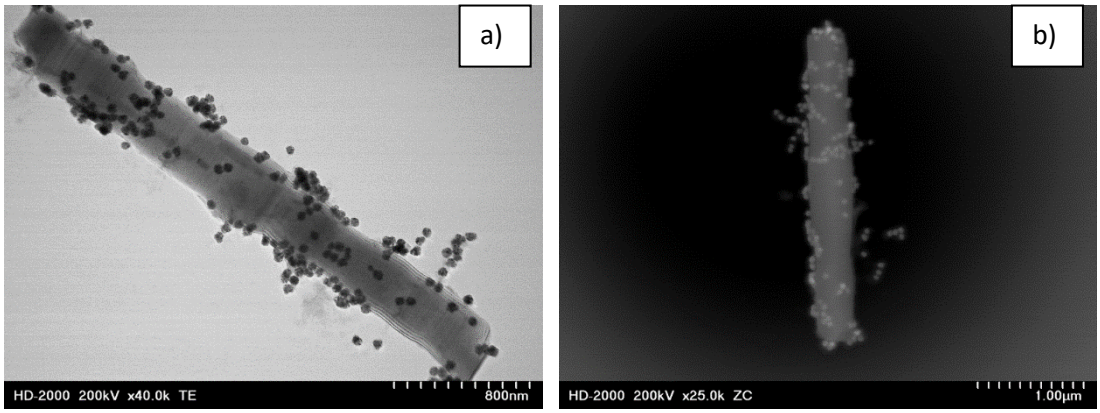

Figure 3.20: Representative (a) TEM and (b) z-contrast images of SiCWs functionalized with NiNPs.

were not uniformly covered with the particles. It was prevalent throughout all images showing an average of 275 ± 132 nanoparticles per whisker, which corresponds to 38 ± 18 nanoparticles/µm^2. Calculated maximum packing density of the NiNPs is approximately 311 nanoparticles/µm^2, which is one order of magnitude larger than the observed experimental value. Thus, the magnetic modification was possible, but resulted in low density of the nanoparticles on the surface. The magnetically modified SiCWs were found to be magnetically active as observed by magnetic rotational spectroscopy (MRS). However, the low and non-uniform coverage warps the magnetic moment in the system. Thus, the whiskers, though observing overall direction, were not oriented exactly along the magnetic field (Figure 3.21).

The two main factors that could have affected the nanoparticle attachment are ineffective complexation between P2VP and PAA and/or blockage of the surface by residuals originated from the nanoparticle synthesis. Thus, the research on modification of SiCWs with NiNPs was not pursued further.

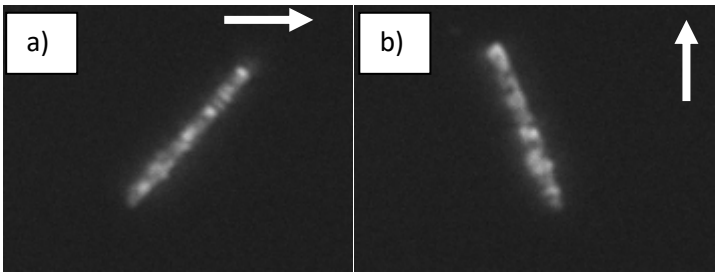

Figure 3.21: Dark field images of a SiCW modified with NiNPs orienting in the magnetic field. The magnetic field direction is denoted by the white arrow. The direction was changed by 90 ^{o} from (a) to (b).

3.4: Conclusions

The following conclusions can be derived as a result of our study reported in Chapter 3:

- Polymer modification of the nanoparticulates was successfully attained after the methodologies were elaborated for the model surfaces.
- NiNPs were attached to the surface of SiCWs via polymer-polymer complexation.
- The modification of the SiCWs with magnetic NiNPs was concluded to substantially underperform with respect to the theoretical calculations of nanoparticle packing and creation of strictly aligned orientation of the whiskers in a magnetic field.

3.5: References

1. Degen, A.; Macek, J., Preparation of submicrometer nickel powders by the reduction from nonaqueous media. *Nanostruct Mater* **1999,** *12* (1-4), 225-228.

2. Koltypin, Y.; Fernandez, A.; Rojas, T. C.; Campora, J.; Palma, P.; Prozorov, R.; Gedanken, A., Encapsulation of nickel nanoparticles in carbon obtained by the sonochemical decomposition of $Ni(C_8H_{12})_2$. *Chem Mater* **1999,** *11* 1331-1335.

3. De Caro, D.; Bradley, J. S., Surface spectroscopic study of carbon monoxide adsorption on nanoscale nickel colloids prepared from a zerovalent organometallic precursor. *Langmuir* **1997,** *13,* 3067-3069.

4. Zhang, H. T.; Wu, G.; Chen, X. H.; Qiu, X. G., Synthesis and magnetic properties of nickel nanocrystals. *Mater Res Bull* **2006,** *41* (3), 495-501.

5. Steigerwald, M. L.; Alivisatos, A. P.; Gibson, J. M.; Harris, T. D.; Kortan, R.; Muller, A. J.; Thayer, A. M.; Duncan, T. M.; Douglass, D. C.; Brus, L. E., Surface derivatization and isolation of semiconductor cluster molecules. *J Am Chem Soc* **1988,** *110* (10), 3046-3050.

6. Wu, Z. G.; Munoz, M.; Montero, O., The synthesis of nickel nanoparticles by hydrazine reduction. *Adv Powder Technol* **2010,** *21* (2), 165-168.

7. Luzinov, I.; Julthongpiput, D.; Liebmann-Vinson, A.; Cregger, T.; Foster, M. D.; Tsukruk, V. V., Epoxy-terminated self-assembled monolayers: Molecular glues for polymer layers. *Langmuir* **2000,** *16* (2), 504-516.

8. Luzinov, I.; Julthongpiput, D.; Malz, H.; Pionteck, J.; Tsukruk, V. V., Polystyrene layers grafted to epoxy-modified silicon surfaces. *Macromolecules* **2000,** *33* (3), 1043-1048.

9. Tsyalkovsky, V.; Klep, V.; Ramaratnam, K.; Lupitskyy, R.; Minko, S.; Luzinov, I., Fluorescent reactive core-shell composite nanoparticles with a high surface concentration of epoxy functionalities. *Chem Mater* **2008,** *20* (1), 317-325.

10. Tsyalkovsky, V.; Burtovyy, R.; Klep, V.; Lupitskyy, R.; Motornov, M.; Minko, S.; Luzinov, I., Fluorescent nanoparticles stabilized by poly(ethylene glycol) containing shell for pH-triggered tunable aggregation in aqueous environment. *Langmuir* **2010,** *26* (13), 10684-92.

11. Zhou, X.; Goh, S. H.; Lee, S. Y.; Tan, K. L., XPS and FTIR studies of interactions in poly(carboxylic acid)/poly (vinylpyridine) complexes. *Polymer* **1998,** *39* (16), 3631-3640.

12. Eluri, R.; Paul, B., Synthesis of nickel nanoparticles by hydrazine reduction: mechanistic study and continuous flow synthesis. *J Nanopart Res* **2012,** *14* (4).

13. Galabura, Y. Synthesis and characterization of nanoscale polymer films grafted to metal surfaces. Ph.D. Thesis, Clemson University, Clemson, SC, 2014.

14. *Properties of Silicon Carbide*. Institution of Engineering and Technology: Stevenage, 1995; Vol. 1.

15. Zdyrko, B.; Klep, V.; Luzinov, I., Synthesis and surface morphology of high-density poly(ethylene glycol) grafted layers. *Langmuir* **2003,** *19* (24), 10179-10187.

16. Kwon, S. G.; Hyeon, T., Kinetics of colloidal chemical synthesis of monodisperse spherical nanocrystals. In *Nanoscale Materials in Chemistry*, 2nd ed.; Klabunde, K. J.; Richards, R. M., Eds. John Wiley And Sons, Inc.: Hoboken, 2009; pp 127-155.

17. Jette, E. R.; Foote, F., Precision determination of lattice constants. *J Chem Phys* **1935,** *3* (10), 605-616.

18. Lifshin, E., *X-ray Characterization of Materials*. Wiley-VCH: Weinheim, 1999.

19. O'Handley, R. C., *Modern magnetic materials: principles and applications*. Wiley: New York, 2000.

20. Lu, H. M.; Zheng, W. T.; Jiang, Q., Saturation magnetization of ferromagnetic and ferrimagnetic nanocrystals at room temperature. *J Phys D Appl Phys* **2007,** *40* (2), 320-325.

21. Zdyrko, B.; Iyer, K. S.; Luzinov, I., Macromolecular anchoring layers for polymer grafting: comparative study. *Polymer* **2006,** *47* (1), 272-279.

22. Tsukruk, V. V.; Luzinov, I.; Julthongpiput, D., Sticky Molecular Surfaces: Epoxysilane Self-Assembled Monolayers. *Langmuir* **1999,** *15* (9), 3029-3032.

23. Huntsman Packaging, High preformance components. Huntsman, Ed. Huntsman: North America, 2015.

24. Kaczmarek, H.; Szalla, A.; Kaminska, A., Study of poly(acrylic acid)-poly(vinylpyrrolidone) complexes and their photostability. *Polymer* **2001,** *42* (14), 6057-6069.

CHAPTER FOUR

MODIFICATION OF SICWs WITH MAGNETIC IRON OXIDE NANOPARTICLES

4.1: Introduction

Since the functionalization of SiCWs with NiNPs (Chapter 3) did not yield the targeted result, MagNPs modified with PAA were selected to be the next option for the modification of the whiskers. MagNPs were preferred because of their commercial availability, magnetism, easily modifiable surfaces, and the range of available sizes and morphologies[1-2]. The PAA to MagNPs bonding via the formation of insoluble salt was envisioned to create a simple and easily controlled route for the surface modification[1]. It is important to point out that the surface of commercially available MagNPs is typically modified. The surface modification is used to control the surface-to-surface interactions and size of the particulates during their synthesis[3]. Hence, the attachment of PAA to the particles' surface could be hindered by the modifications. Thus, it was necessary to select particles, which possess surface modifiers compatible with the process of anchoring of PAA. In fact, the MagNPs selected for this study were covered with PVP, which can form a complex with PAA[4].

In general, this chapter describes our research on the modification of SiCWs with MagNPs via polymer-to-polymer complexation. The surface-bound PAA was used to create complexation with the P2VP-modified SiCWs[5]. The surface morphology and structure of the MagSiCWs were studied using SEM, TEM imaging and magnetometry.

Specifically, the goal of the characterization of the surface was to determine the morphology and thickness of the magnetic nanoparticles layer. The magnetic modification of the SiCWs was performed utilizing the dispersions of the MagNPs of different concentrations. Finally, to test the magnetic orientation of the whiskers, the MagSiCWs were dispersed and oriented into a polyethylene oxide (PEO) thin film.

4.2: Experimental

4.2.1: Size Separation of Iron Oxide Nanoparticles

The MagNPs were ordered from US Research Nanomaterials, Inc. and composed mostly of magnetite. The MagNPs were cleaned and separated in methanol in three stages. First, they were dispersed into methanol at 10 wt. %. Then, they were ball-milled with glass balls (1 mm in diameter) on a high setting for one hour in a IKA® Ultra Turrax® tube disperser with a ST-20/50 dispersion tube. Then, a Precision-Durafuge 100 centrifuge was used at 5000 rpms for 15 min to remove large agglomerates from the suspension. The centrifuge was used three times on the same suspension. After each centrifugation, the top portion of the supernatant was decanted and kept. Next, an Eppendorf-mini spin plus centrifuge was used at 10000 rpms for 3 min. The decanted portion of the nanoparticle suspension was centrifuged 3 more times, and each time the sediment was kept for further use. The nanoparticle suspension after this process was the color of maghemite (rusty)[2, 6]. After size separation was completed, the particles were imaged by TEM.

4.2.2: Surface Modification of Iron Oxide Nanoparticles

The obtained MagNPs were redispersed in methanol to make a 0.3 wt. % colloidal suspension. Then, 3 wt. % solution of PAA (M_w=100,000 g/mol) in methanol was prepared and sonicated. The nanoparticles suspension was added dropwise (1:1 final volume ratio) into the sonicated PAA solution. Finally, this PAA/MagNPs suspension was shaken for 24 hours and cleaned three times by repetitive centrifugation at 10000 rpms, magnetic separation and redispresion in methanol. The magnetic separation was carried out using a ~200 G neodymium magnet placed at the bottom of the vail containing the nanoparticles dispersion. The formation of PAA-anchored layers was monitored using TEM and TGA.

4.2.3: Fabrication of Magnetically Functionalized SiCWs

Two dispersions (SiCWs modified with P2VP and MagNPs modified with PAA in methanol) were mixed under continuous sonication in 1:10, 1:8.6, 1:5, and 1:2 weight ratios (MagNPs:SiCWs). The concentration of SiCWs dispersion was on the level of 1-2 wt. %. During the procedure, the dispersion of SiCWs was added dropwise to the dispersion of sonicated MagNPs. Such order of mixing ensured the particles would modify the whiskers and prevent nanoparticle bridging between the whiskers.

After each of the modifications was conducted, visual observation based on color of the layer above the sediment (clear, no color) indicated absence of any visually detectable amount of free nanoparticles. These magnetic whiskers were dispersed in

methanol and vigorously shaken for 24 hours. Then, to finalize the functionalization, the whiskers were added dropwise to a sonicated 2 wt. % solution of PAA in methanol. This secondary modification completed the coverage of the SiCWs with a final PAA layer complexing with any P2VP available on SiCWs surface. The final SiCW suspension was shaken for 24 hours. After the shaking, the MagSiCWs were cleaned in methanol by magnetic separation and centrifugation.

The attachment of MagNPs to the surface of SiCWs allowed for proximity agglomeration and collection of the MagSiCWs using a magnet. The whiskers modified with MagNPs showed an immediate response to a magnetic field. The magnet was held near the bottom of the vial containing dispersion for 15 min, and then the top portion of the liquid was decanted off. Then, centrifugation at 5000 rpm was done for 15 min. The solvent layer above sediment was decanted, and the sediment of SiCWs was redispersed in methanol and used for further studies. The MagSiCWs were characterized by TEM.

4.2.4: Magnetic Characterization

An alternating gradient field magnetometer (AGM 2900 Princeton Measurement, Inc.) was used to characterize the magnetic properties of materials. For each sample, the induced magnetic moment was measured as a function of the applied magnetic field. The applied magnetic field was slowly increased to a maximum of 400 kA/m and then decreased to -400 kA/m. The resulting hysteresis loops were analyzed. Magnetic

characterization and data interpretation were conducted by Pavel Aprelev under the guidance of Prof. K. Kornev.

Samples of MagNPs and MagSiCWs were prepared by drying at room temperature, weighing, and encapsulating in scotch tape to prevent the loss of material. The dry magnetic samples were mounted on the magnetic probe and their hysteresis curves were measured.

No magnetic hysteresis was observed and the magnetization curves were consistent with the behavior of paramagnetic materials described by the Langevin function[7-8]:

$$m = Nm_p\left(\coth\left(\frac{m_pH}{k_BT}\right)-\frac{k_BT}{m_pH}\right) \qquad (4.1)$$

where m is the magnetic moment of the sample, H is the magnitude of the external magnetic field measured in Teslas, N is the number of magnetic domains in the sample, m_p is the magnetic moment of a single domain, k_B is the Boltzmann constant, and T is the absolute temperature. The magnetic moment of the sample was calculated by fitting the magnetization curves with the Langevin equation (1) and extracting the product Nm_p[7, 9-10]. A comparison between the samples was made after normalizing the saturation magnetic moment by the mass of the sample.

4.2.5: Orientation of MagSiCWs in PEO Composite Film

PEO with a molecular weight of 1,000,000 g/mol was used as a matrix for the model composite film. PEO was dissolved to form 2.1 wt. % solution in methanol. The PEO solution was purified by multiple centrifugations at 5000 rpm to remove any non-soluble materials. Then, the MagSiCWs were dispersed into the PEO methanol solution. The concentration of MagSiCWs in the PEO matrix was 0.5 wt. % (~0.16 vol. %) and 1.84 wt. % (~0.58 vol. %).

The PEO-MagSiCW composite films were fabricated by dip-coating silicon wafers into the suspension of the whiskers in the PEO solution. Specifically, silicon wafers were cut into 1x4 cm rectangles and cleaned by sonication in DI water for a total of 45 min, replacing the water every 15 min. Then, the wafers were placed into a "piranha" solution (25 vol. % of 30 % hydrogen peroxide and 75 vol. % of concentrated sulfuric acid) for 30 min. at 60–80 ^{o}C and rinsed with DI water. After the cleaning and drying, the silicon wafers were dip-coated into a 2 wt. % solution of pure PEO in methanol at 5.4 mm/s velocity. Using the AFM scratch technique[11], pure PEO thin films were found to be 300 ± 20 nm thick. The AFM measurements were performed in tapping mode at 1–2 Hz on a Dimension 3100 (Veeco Instruments) microscope using silicon probes (50 N/m spring constant).

The dip-coating of the PEO-MagSiCWs mixture in methanol was accomplished employing the same parameters as used for the pure PEO solution in methanol. However, the drying of the dip-coated wafer was carried out in a vial between two parallel neodymium magnets (K&J Magnetics) (Figure 4.1a). The distance between the magnets

was about 6 cm. The vial was used to slow down the evaporation of the methanol during the film formation. This allowed more time for the SiCWs to orient in the direction of the magnetic field. Figure 4.1b shows the magnetic field gradient in-between the magnets observed in the experiments. The magnetic field was measured using a DTM-133 digital teslameter.

The field over the sample varied from 216 G at the very center of the sample to 320 G at the ends of the wafer (Figure 4.1b). The orientation of the whiskers was imaged using an Olympus MVX10-TLU optical microscope.

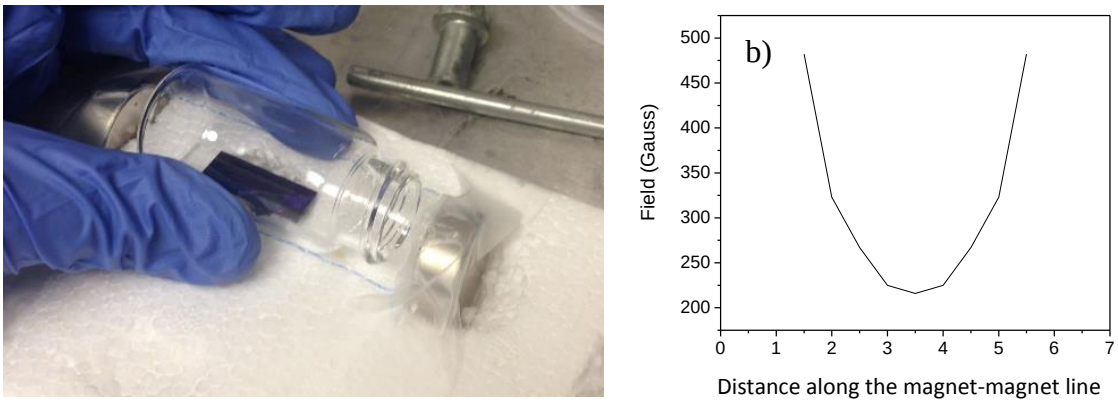

Figure 4.1: (a) The experimental set-up used for drying of the PEG-MagSiCW film; (b) magnetic field in-between the magnets.

4.3: Results and Discussion

4.3.1: Size of the MagNPs

The MagNPs' surface chemistry and size are important factors in polymer modification. Thus, after the size separation, the MagNPs were imaged using TEM (Figure 4.2) to determine the size distribution in the material. TEM imaging indicated that the nanoparticles have variable shape, which was expected considering the co-

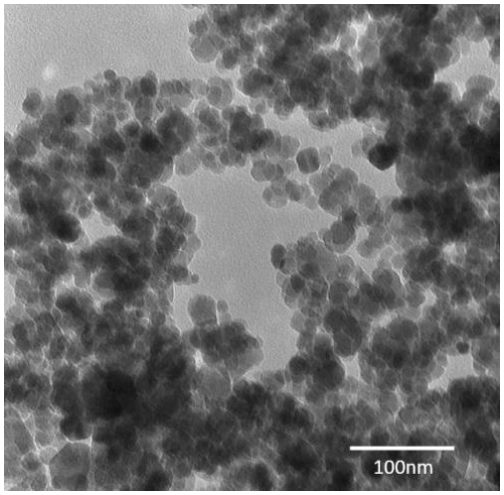

Figure 4.2: TEM image of the bare MagNPs obtained after separation processing.

precipitation synthesis. The size of the MagNPs was measured manually from TEM images using Gwyddion software. Specifically, 635 individual nanoparticles were carefully identified and measured using the representative nanoparticle diameter or longest dimension of the shape (if the shape was non-spherical). The radius size distribution of individual MagNPs was identified through JMP® statistical software (Figure 4.3).

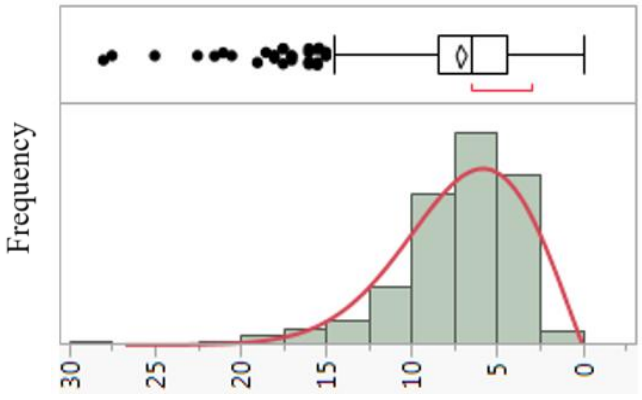

Figure 4.3: The particle size distribution fitted to the Weibull function (—). The top of the figure provides the statistical relevance of the distribution.

The mean radius of the MagNPs was 7.1 ± 3.7 nm. The top portion of the Figure 4.3 shows the range using the bars, the statistical median with outer quartiles of 25% and 75% using the boxes, the mean using the diamond within the boxes, and the statistical outliers using the dots outside of the bars. The histogram of the MagNPs' radius (Figure 4.3) was fitted with the Weibull statistical function (—). The function parameters were identified as 8.08 for the scale and 2.04 for the shape[12]. The shape parameter is the slope of the probability plot, meaning it changes with the behavior of the distribution peak. The scale parameter is equal to the broadening and sharpening of the distribution peak.

4.3.2: Modification of MagNPs with PAA

The MagNPs were modified with PAA via adsorption from methanol solution. The modified MagNPs were analyzed by TEM and TGA (Figure 4.4). Figure 4.4a shows the image of an agglomerate of the MagNPs uniformly covered with PAA. This image was used to estimate the PAA layer's thickness.

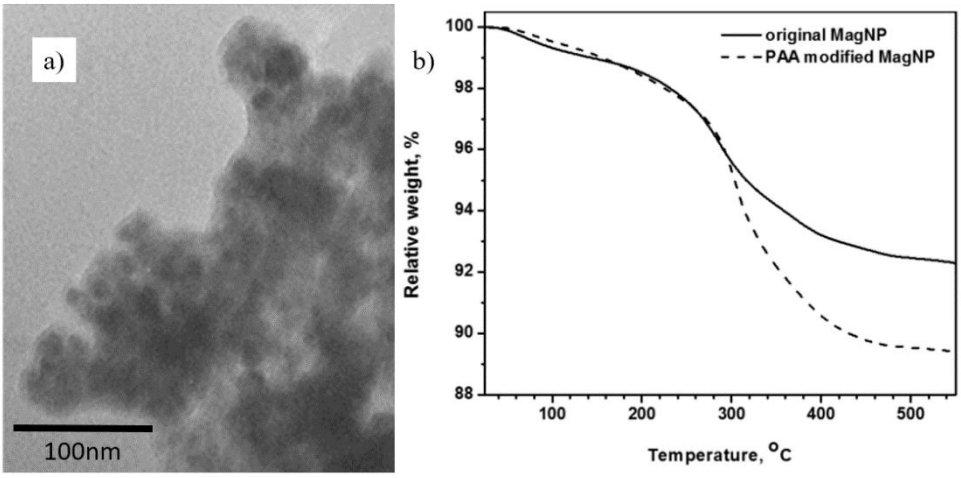

Figure 4.4: (a) TEM image of MagNPs modified with PAA and (b) TGA curves of original and modified MagNPs.

The thickness of PAA was measured at selected locations. The thickness was found to be ~10 nm (Figure 4.4a). However, the polymer film was not easily identified due to the significant aggregation of the nanoparticles. To further estimate the thickness of the polymer layer, TGA was used to measure the amount of polymer attached to the surface through weight loss (Figure 4.4b). The observed weight loss associated with PAA was ~3 wt. %. Equations 4.2 and 4.3 from Mefford et al.[12] were used to determine the thickness of the anchored polymer layer:

$$\sigma = \left({W_p N_A \rho_{mag}} \Big/ {M_n W_{mag}} \right) * \int_0^\infty \left(\frac{r}{3}\right) P(r) dr \tag{4.2}$$

$$t = {\sigma * M_n} \Big/ {N_A * \rho_p} \tag{4.3}$$

where σ is the chain density per particle, t is the thickness of PAA on the surface, W_p and W_{mag} is the weight fractions of polymer and MagNPs, respectively, N_A is Avogadro's number, ρ_{mag} and ρ_p is the density of the MagNPs and PAA, respectively, r is the radius of the measured MagNPs, and the P(r) is the Weibull probability function for the MagNP radius distribution (fitted line in Figure 4.3). Using Equations 4.2 and 4.3, the polymer layer thickness was found to be 0.5 nm. This result did not match TEM observations. The discrepancy was caused by the modification of MagNP aggregates and not individual particles. Additionally, Equation 3.6 was used to estimate that PAA layer was ~0.3 nm, which is approximately the same result as obtained from Equations 4.2 and 4.3.

The size of nanoparticle agglomerates were identified using SEM imaging of the magnetically functionalized SiCWs (Section 4.3.3). The diameter of the agglomerates structure was measured by identifying the shape of the agglomerates and drawing a circle

around the structure. The diameter of the circle was then identified as the agglomerate diameter. Approximately, 500 measurements were made (Figure 4.5).

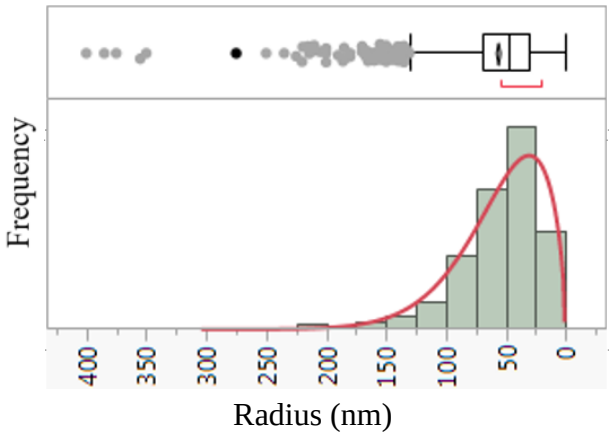

Figure 4.5: The nanoparticle agglomerate size distribution fitted to the Weibull function. The top of the figure provides the statistical relevance of the distribution.

The average agglomerate was determined to be 55.3 ± 39.0 nm in radius. The top portion of Figure 4.5 shows the range using the bars, the statistical median with outer quartiles of 25 % and 75 % using the boxes, the mean using the line within the boxes, and the statistical outliers using the dots outside of the bars. The agglomerate distribution was fitted to a Weibull plot identifying the scale and shape parameters to be 60.56 and 1.52 for the agglomerate structure. Then, using Equations 4.2 and 4.3, about 5 nm polymer layer was estimated to be on the surface of the nanoparticle agglomerates. This result is in good agreement with the thickness of PAA layer obtained from TEM. This indicated that the agglomerate structures are being modified by the PAA. Thus, particle agglomerates were identified as the major nanoparticle structure, which were used for the SiCWs modification.

4.3.3: Modification of SiCWs with MagNPs

The functionalization of SiCWs with MagNPs was a critical step in the process of creating oriented SiCWs. As SiCWs are not magnetic, it would take great amount of force from shear or electric fields to orient them. Thus, our solution to this problem was to attach MagNPs to the SiCW's surface via polymer complexation in a solution and add a magnetic moment to the SiCWs.

After grafting and adsorbing P2VP and PAA polyelectrolytes to the whiskers and particles, respectively, MagNPs and SiCWs dispersions were mixed together at various ratios to target high packing density and the uniform coverage of the whiskers. Specifically, the MagNPs and SiCWs were mixed in the following weight ratios: 1:2, 1:5, 1:8.6, and 1:10 (MagNPs:SiCWs). Then, the whiskers modified with MagNPs were imaged using SEM and TEM. The analysis of the MagNPs layer was done by measuring distance from the whisker's surface to the outer edge of the MagNP layer. 3-9 whiskers were measured for each produced batch with ~50 equally spaced measurements taken from the surface of each whisker.

The measurements were averaged and plotted in Figure 4.6a. Figure 4.6b shows a representative image of the SiCW surface morphology.

The apparent thicknesses of MagNP layers attached to the SiCWs were 158 ± 55 nm, 111 ± 47 nm, 66 ± 45 nm, and 57 ± 32 nm for the 1:2, 1:5, 1:8.6, and 1:10 of MagNP:SiCW ratio, respectively. The functionalized surface uniformity was gauged through the standard deviation of the average apparent thickness. In all cases uneven surface structures were created with a maximum standard deviation of 60 nm and

minimum of 32 nm (Figure 4.6a). Student's statistical t-test was done for the apparent thickness results to determine whether the results obtained for the different ratios are statistically different.

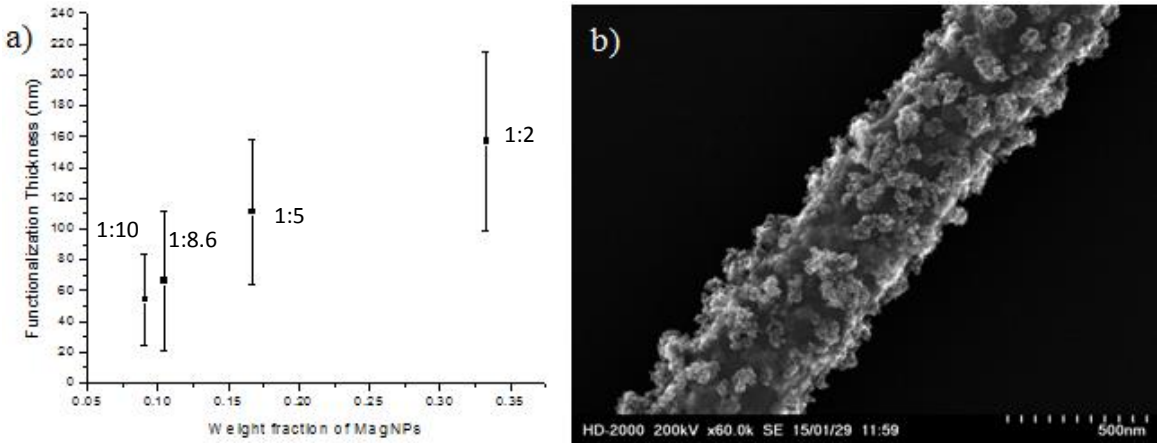

Figure 4.6: (a) The average thickness of the attached MagNPs layer vs weight fraction of magnetic nanoparticles; (b) the SEM image of the MagSiCWs for the 1:10 ratio.

With the help of Dr. William Bridges and Dr. Brooke Russell from the Mathematical Sciences Department of Clemson University, the statistical difference of the thickness values was estimated (Table 4.1).

Table 4.1: Student's t-test results for the sets of MagSiCWs batches .

Batch	Batch	Difference	Std Err Dif	p-Value
1:2	1:10	0.095	0.015	<0.001
1:5	1:10	0.049	0.023	0.0006
1:2	1:5	0.046	0.012	0.0006

The p-value results indicated that there was a statistical difference between the results obtained for different batches of the MagSiCWs[13].

In the next step of statistical analysis, the thickness measurements were divided into the batch (or weight ratio), the whiskers, the side of whiskers, and the individual measurements (Figure 4.7). Additionally, the whiskers were assumed to be independent

from each other. As such, the statistical analysis was the comparison of whiskers by functionalization which was broken up into sides of the whiskers and then the side of the whiskers had individually measured points along the whisker. To prove the independence of the whiskers, the sides and the individually measured points of the whiskers were analyzed.

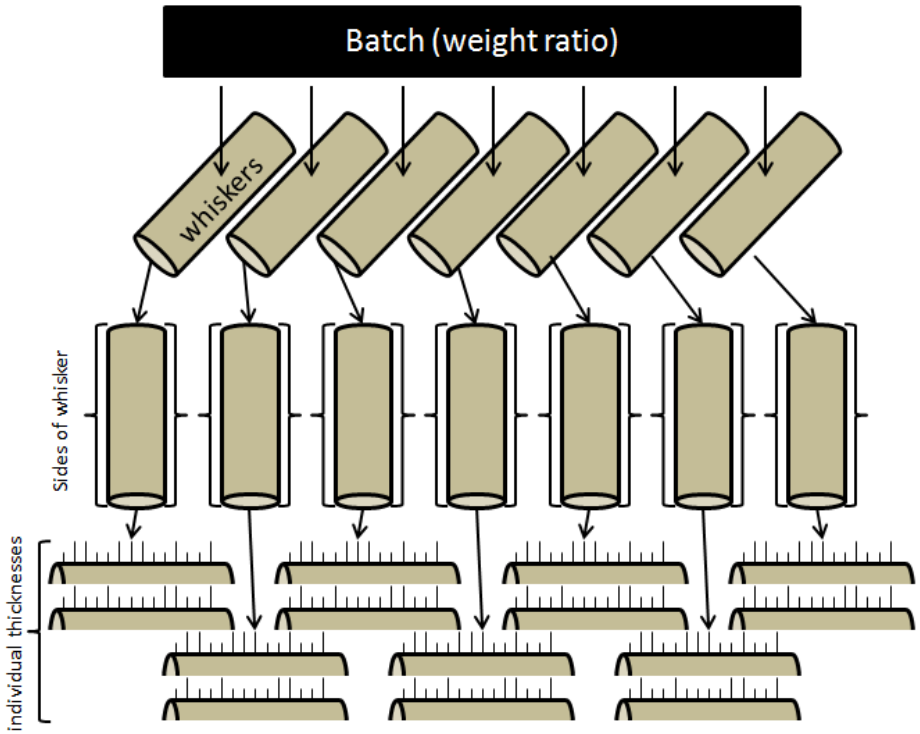

Figure 4.7: Schematic diagram of the statistical analysis methodology for the MagNPs layer attached to the SiCWs.

The measured points of the individual sides were compared in the order they were measured along the surface. However, no pattern was found from analyzing the ordered surface measurement. Thus, the thickness of the magnetic nanoparticle layer was

randomly distributed along the surface of the whisker[13]. Then, the measured points along the whiskers were compared with the distribution of a Weibull plot (Figure 4.8).

The distributions were considered unimodal and semi-symmetric. The distribution of thickness measurements for each whisker was fitted to the Weibull expression (Figure 4.8). Additionally, the Cramer-von Mises Watson test gave an average value of .087, which was less than the tabulated 0.25, meaning that the Weibull fit was statistically

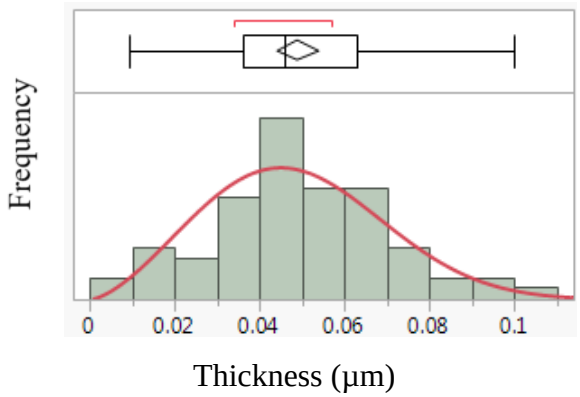

Figure 4.8: Representative histogram of the MagNP layer attached to the SiCW surface fitted to the Weibull function (—). The top of the figure provides the statistical relevance of the distribution.

good[13]. The top portion of Figure 4.8 indicates the range, the statistical median with outer quartiles of 25 % and 75 %, and the mean represented by the bars, the boxes, and the diamond within the boxes. Then, the variance for these was low in comparison to the overall distribution, meaning the whisker-to-whisker and surface-to-surface thickness differences were not statistically significant.

However, the overall variance of the individual measurements by batch showed statistical significance. Thus, the functionalization measurements were compared by the weight ratio of MagNPs to SiCWs. It appeared that the functionalization thicknesses were

statistically significant by the weight ratio of MagNPs to the SiCWs. The statistical trend of thickness to batch is shown in Figure 4.9. It reveals that the individual batches were significantly different from each other and the 1:8.6 did not have statistical relevance.

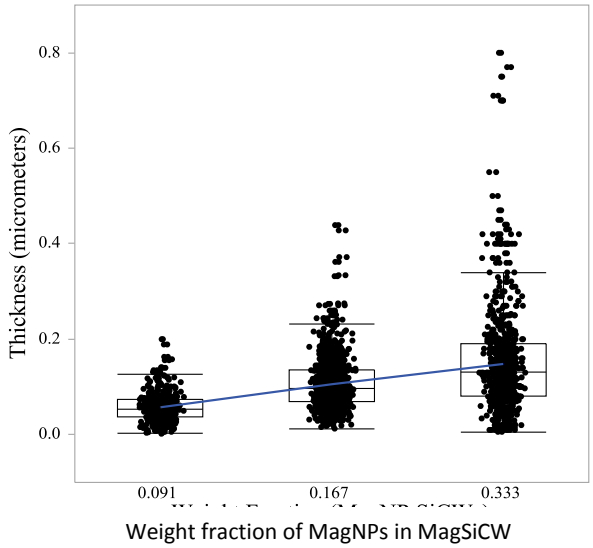

Figure 4.9: Measured thickness of the MagNP layer on the SiCWs from TEM images vs. weight fraction of the MagNP in the MagSiCW. (where: the mean (—), median, 25% to 75% quartile, range, and the individual measurements are represented by the blue fitted linear line, the middle line of the boxes, the upper and lower lines on the boxes, the bars and the individual dots).

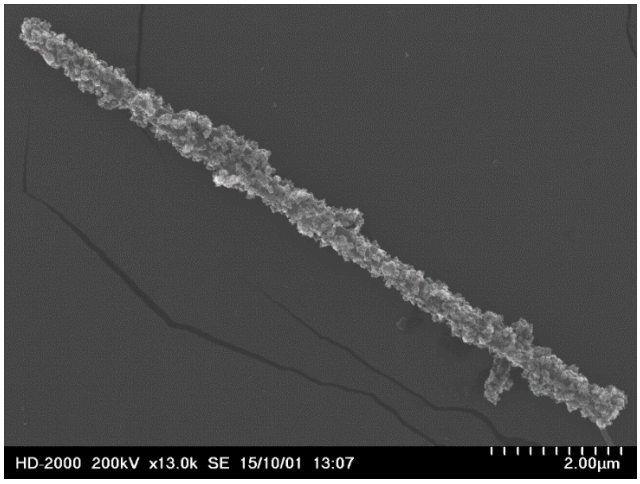

Figure 4.10: Representative SEM image of MagSiCWs obtained for the 1:5 ratio.

The 1:5 weight ratio of MagNPs to SiCWs was selected for further studies due to the average thickness of 111 nm of MagNPs layer being very close to the size of MagNPs aggregates. A representative image of the 1:5 SiCWs is shown in Figure 4.10.

4.3.4: Magnetic Characterization of the MagSiCWs

We determined the parameters of the Langevin equation (4.1) – m_p and M_g – for the MagNPs and MagSiCWs. The parameter M_g was used to analyze the amount of magnetic material attached to the whiskers. Additionally, the parameter mp was compared between MNPs and MagSiCWs to investigate the effect of magnetic interaction between individual nanoparticles on total magnetization of material. A typical plot of MagNPs and MagSiCWs magnetic moment vs. applied field along with their Langevin fit is presented in Figure 4.11.

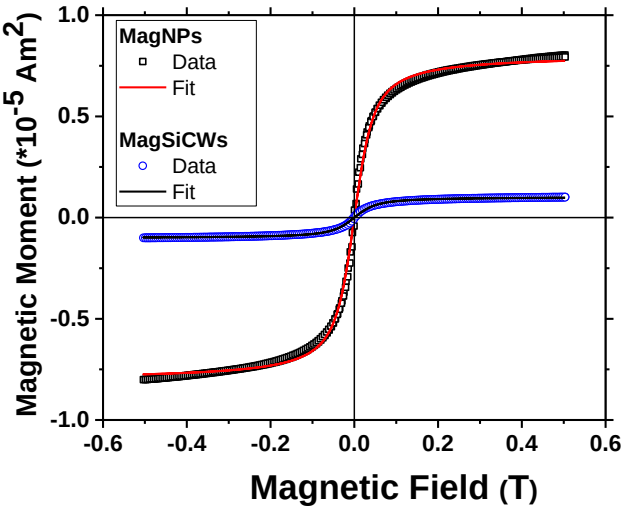

Figure 4.11: Magnetization curves for MagNPs and MagSiCWs (prepared with the 1:5 ratio).

The magnetization curve shows that there is no significant ferromagnetic coercivity or remnant magnetization of either MagNPs or MagSiCWs at the fields investigated. This is consistent with the expectation and is due to the superparamagnetic properties of iron oxide nanoparticles used in this research. Moreover, the average magnetic moment of each nanoparticle in the MNP samples and in the MagSiCW samples are practically the same, mp = $(2.2\pm0.1)*10^{-19}$ Am^2 and m_p = $(2.2\pm0.2)*10^{-19}$ Am^2 , respectively. This indicates that the particle-to-particle interactions caused by the attachment of the MagNPs to each other and to the SiCWs do not significantly affect the magnetic properties of the MagNPs. The results also confirmed a significant level of attachment of the magnetic nanoparticles to the whisker surface.

Since the magnetic properties of the nanoparticles are not affected by the attachment, the ratio of the M_g values for MagNPs and MagSiCWs can serve as a verification of the mass ratio between the nanoparticles and the silicone-carbide whiskers in the MSiCWs sample. The saturation mass magnetization for MagNPs and MagSiCWs are M_g = 0.064 ± 0.01 Am^2/g and M_g = 0.0055 ± 0.002 Am^2/g, respectively. From this measurement, it follows that the mass concentration of magnetic nanoparticles in MagSiCWs sample is 9±4%.

4.3.5: Study of Orientation of MagSiCWs in a PEO Matrix

To demonstrate the possibility of magnetic orientation for the functionalized SiCWs, thin film composites were fabricated with PEO as a matrix. The orientation of the MagSiCWs in a viscous polymer solution (formed as the composite film was drying) was used to confirm the possibility of the magnetic alignment in a dynamically changing

environment. The orientation of the whiskers in a magnetic field is dependent on the orientation of MagSiCWs' magnetic moment. Thus, this orientation experiment also tested the magnetic uniformity of the MagNPs' layer on the SiCWs.

The nanocomposite thin films of MagSiCW and PEO containing 0.16 vol. % and 0.58 vol. % of whiskers were fabricated. These concentrations were chosen to evaluate the effects of whisker-to-whisker spacing on the orientation of the whiskers. Figure 4.12 shows the orientation of the whiskers (as an angle from the net director). The result

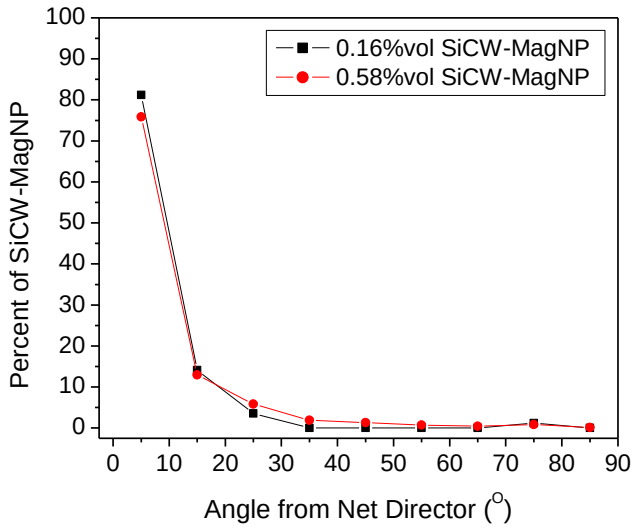

Figure 4.12: Distribution of orientation for PEO composites with 0.16 vol. % and 0.58 vol. % of MagSiCWs.

indicates that the magnetic nanoparticle layer is magnetically uniform, as evident from a high degree of orientation. The composite with 0.16 vol. % of whiskers had slightly greater than 83 % of them oriented within 10 ^{o} of the net director. The composite with 0.58 vol. % of the whiskers had greater than 75 % of them oriented within 10 ^{o} of the net director. Thus, with a 3.5-fold increase in the whiskers' concentration, the orientation decreased by just 8 %. Therefore, the composite with 0.58 vol. % of MagSiCWs in the

PEO matrix was used in further experiments to allow more whiskers to be observed. The orientation vs the field gradient was quantified for 0.58 vol. % composite film.

a)

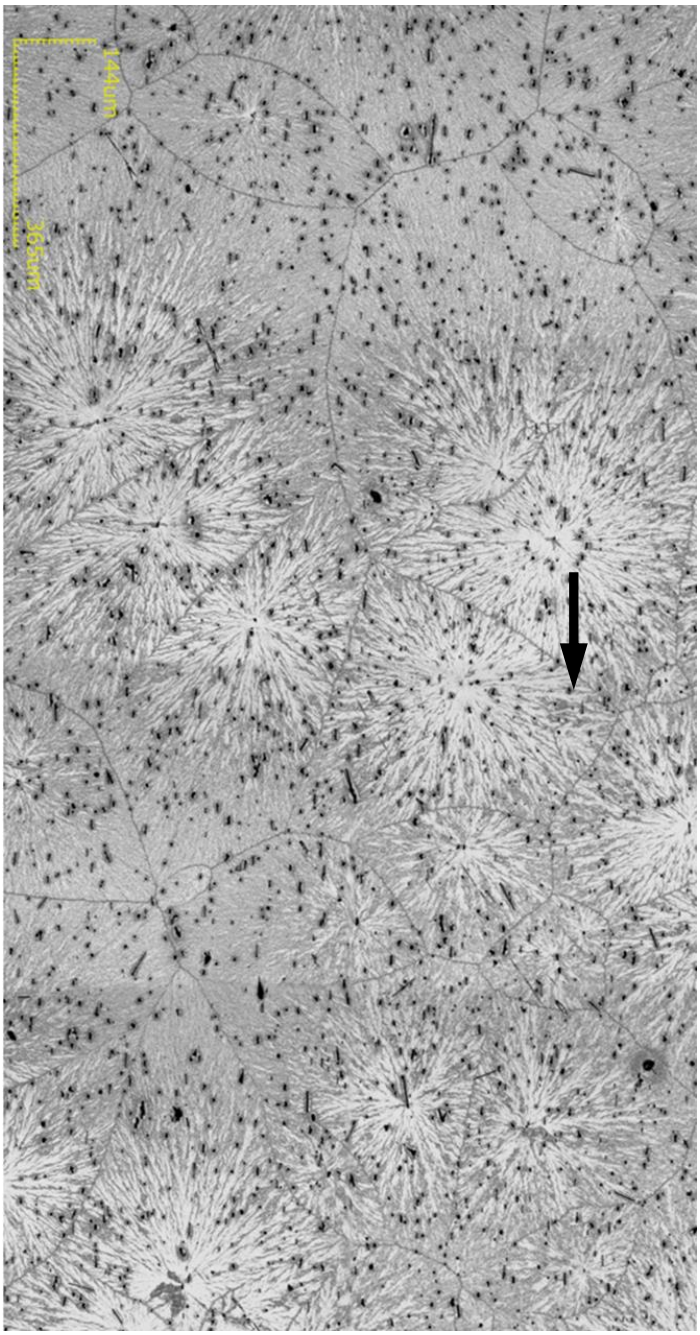

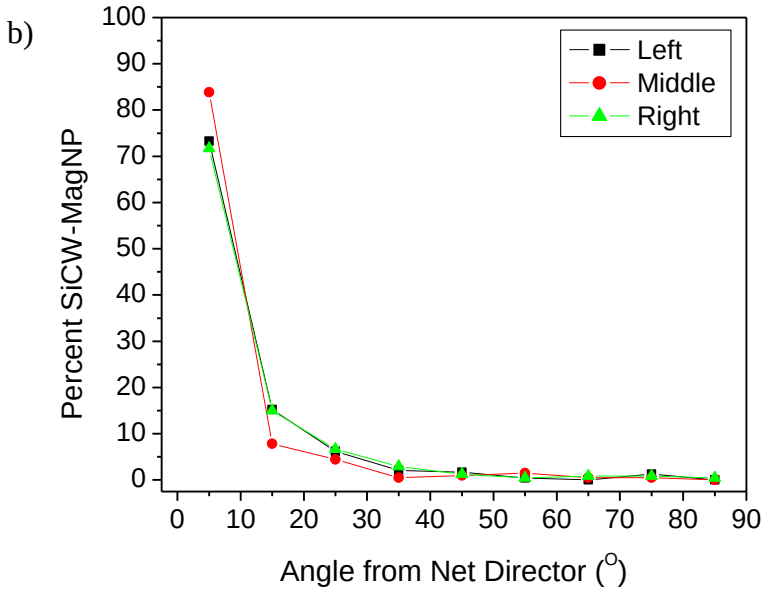

Figure 4.13: (a) Stitched image of the composite thin film with 0.58 vol% of SiCW-MagNP (the image is rotate 90 º clockwise); the black arrow describes the direction of the net director; (b) the distribution of orientation from left, middle, and right portions of the image.

Figure 4.13b shows the difference in the whiskers' orientation over long distances in the sample. Specifically, Figure 4.13a is a stitched image of the composite film with 0.58 vol. % of MagSiCWs in PEO. The image is 2.4 mm long, showing macro-scale orientation. The center of the image correlates to the center of the applied magnetic field (Figure 4.1b). The field varied by 0.3 G from the center of the image to each edge (Figure 4.13a).The average orientation of the entire sample is 7.8º, while the orientation varies by 2.7 º from the middle to the right of the image and 2.2 º from the middle to the right of the image. Where, the average orientation from the magnetic field is 8.3 º, 6.1 º, and 8.8 º for the left, middle, and right portions of the stitched image (Figure 4.13b). The middle of Figure 4.13a has the highest degree of orientation, along with the lowest applied magnetic field and gradient within the composite. It appears that not strength of magnetic

field, but rather its uniformity caused by equal fields from both magnets is a decisive factor in the orientation.

4.4: Conclusion

The following conclusions can be drawn as a result of the study reported in Chapter 5:

- The SiCWs can be magnetically modified using polymer-to-polymer complexation of PAA adsorbed to MagNPs with the grafted P2VP on the SiCWs.
- The most uniform and highly packed layer of MagNPs on SiCW's surface was fabricated using 1:5 weight ratio of the nanoparticles to the whiskers.
- The modification of the SiCWs with the MagNPs did not affect the magnetic properties of the nanoparticles.
- High degree of orientation of MagSiCWs by a magnetic field could be achieved within a dynamically changing viscous environment.

4.5: References:

1. Cheng, Y. H.; Chen, Z.; Zhu, M. F.; Lu, Y. F., Polyacrylic acid assisted assembly of oxide particles and carbon nanotubes for high-performance flexible battery anodes. *Adv Energy Mater* **2015,** *5* (6), 1401207.

2. Cornell, R. M.; Schwertmann, U., *The iron oxides: Structure, properties, reactions, occurrences and uses*. Wiley-VCH: Weinheim, 2003.

3. Teja, A. S.; Koh, P. Y., Synthesis, properties, and applications of magnetic iron oxide nanoparticles. *Prog Cryst Growth Ch* **2009,** *55* (1-2), 22-45.

4. Lau, C.; Mi, Y., A study of blending and complexation of poly(acrylic acid)/poly(vinyl pyrrolidone). *Polymer* **2002,** *43* (3), 823-829.

5. Zhou, X.; Goh, S. H.; Lee, S. Y.; Tan, K. L., XPS and FTIR studies of interactions in poly(carboxylic acid)/poly(vinylpyridine) complexes. *Polymer* **1998,** *39* (16), 3631-3640.

6. Parkinson, G. S., Iron oxide surfaces. *Surf Sci Rep* **2016,** *71* (1), 272-365.

7. Gu, Y.; Burtovyy, R.; Townsend, J.; Owens, J. R.; Luzinov, I.; Kornev, K. G., Collective Alignment of Nanorods in Thin Newtonian Films. *Soft Matter* **2013,** *9* (35), 8532-8539.

8. Chikazumi, S. O.; Graham, C. D., *Physics of ferromagnetism*. 2nd ed.; Oxford University Press: Oxford ; New York, 2009; p 655.

9. Gu, Y.; Kornev, K. G., Ferromagnetic Nanorods in Applications to Control of the In-Plane Anisotropy of Composite Films and for In Situ Characterization of the Film Rheology. *Advanced Functional Materials* **2016,** *26* (22), 3796-3808.

10. Aprelev, P.; Gu, Y.; Burtovyy, R.; Luzinov, I.; Kornev, K. G., Synthesis and Characterization of Nanorods for Magnetic Rotational Spectroscopy. *Journal of Applied Physics* **2015,** *118*, 074901.

11. Seeber, M.; Zdyrko, B.; Burtovvy, R.; Andrukh, T.; Tsai, C. C.; Owens, J. R.; Kornev, K. G.; Luzinov, I., Surface grafting of thermoresponsive microgel nanoparticles. *Soft Matter* **2011,** *7* (21), 9962-9971.

12. Mefford, O. T.; Carroll, M. R. J.; Vadala, M. L.; Goff, J. D.; Mejia-Ariza, R.; Saunders, M.; Woodward, R. C.; St Pierre, T. G.; Davis, R. M.; Riffle, J. S., Size analysis of PDMS-magnetite nanoparticle complexes: Experiment and theory. *Chem Mater* **2008,** *20* (6), 2184-2191.

13. Cowan, G., *Statistical data analysis*. Oxford University Press: Oxford, New York, 1998.

CHAPTER FIVE

ORIENTATION OF MAGETICALLY MODIFIED SIC WHISKERS IN A CURING EPOXY MATRIX

5.1: Introduction

As discussed in the previous chapter, the SiCWs can be functionalized with MagNPs and the whiskers orient in a polymer matrix with the application of a magnetic field. The obtained results demonstrated that macroscale orientation is possible in a polymer solution to form nanocomposite thin films. In this chapter, the results on the study of the orientation of MagSiCWs within a complex reacting system, epoxy resin, are presented. Specifically, this chapter focuses on the relationship between the orientation of the MagSiCWs in the epoxy matrix and the kinetics of the epoxy curing.

The epoxy system could create challenges for the orientation during resin curing. These challenges arise due to local stoichiometry for reactive groups at the surface, whisker-to-whisker cross-linking, and variations in the cross-linking density of epoxy polymer[1-2]. These events are directly related to the polymerization of the epoxy. To this end, in this study, the polymerization of the epoxy resin was monitored by following the viscosity and reaction kinetics.

First, the viscosity was measured on the macroscale to determine the working time for the orientation of the MagSiCWs. This was completed using the ball drop method[3-4]. Second, the kinetics of the epoxy curing was monitored using DSC with a method developed by Abenojara et al.[5] Next, the time required for magnetic orientation of the whiskers was theoretically estimated by modeling the characteristic time of

orientation for a super-paramagnetic nanorod in a liquid[6-8]. It was assumed that the MagSiCWs did not interact with each other by physical contact or magnetic interaction. Additionally, the material response to the magnetic field was assumed to be super-paramagnetic.

Finally, the functionalized whiskers were dispersed into the epoxy and the real-time magnetic orientation was conducted. A low concentration of the whiskers was used to minimize the whisker-to-whisker interactions. The MagSiCW/epoxy system was cast into a glass mold to image the whiskers' rotation in the magnetic field. Two magnets placed on either side of the glass mold were used to create a quasi-uniform magnetic field. The images of an identified set of whiskers were taken every 1 min. to monitor how fast the whiskers were orienting in the magnetic field. These images were compiled to show the influence of local viscosity/system changes on the magnetic orientation of the whiskers.

5.2: Experimental

5.2.1: Ball Drop Methodology

After mixing with a hardener and catalyst, the epoxy was poured into a 20-ml glass test tube with a diameter of 1.5 cm. The test tube was placed upright next to a ruler and a microscope. Then, a glass sphere, measuring 2 mm in diameter, was placed on the surface of the epoxy resin. As the sphere dropped into the epoxy, a meniscus would appear between the glass sphere and the epoxy. A microscope was used to monitor the retraction of the meniscus from the glass sphere. The retraction of the meniscus signified the complete immersion of the sphere in epoxy. As the sphere moved down and away

from the resin surface, the speed of the sphere was monitored as the sphere crossed the 2-cm marking and passed the 4–5 cm vertical distance in the resin, where 0 cm was at the surface of the epoxy resin. A ruler was used to measure the distance the glass sphere had traveled during a given time period. Using Equation 5.1, the velocity of the dropping sphere, V_s, was used to calculate the apparent epoxy viscosity, η[3-4]:

$$\eta = \frac{2r^2 g(\rho_S - \rho_L)}{9V_s} \tag{5.1}$$

where ρ_S and ρ_L are the density of the glass sphere (~2.6 g/cm^3) and liquid resin (~1 g/cm^3), g is gravitational acceleration (9.8 m/s^2), and r is the radius of the sphere (1 mm). The measurements were conducted at room temperature.

5.2.2: Calibration of the Ball Drop Experiment

The validity of the experimental procedure to evaluate viscosity was checked by measuring the viscosity of glycerol. A diagram showing how the measurements were conducted is depicted in Figure 5.1. For each experiment, a separate ball was dropped. The time counting started at 2-3 cm mark. The time at which the ball passed certain centimeter points (depth of the measurement) on the ruler was registered. Three or four balls were dropped for each measurement. The measurements were conducted at room temperature. In addition, the use of a different glass sphere for each measurement did not have a significant effect on the result variability. The results from the terminal velocity experiment are shown in Figure 5.1b. The obtained results show that the average velocity of the sphere is 0.0046 ± 0.0003 m/s (calculated as an average of all the average velocities for the sphere traveled through the glycerol).

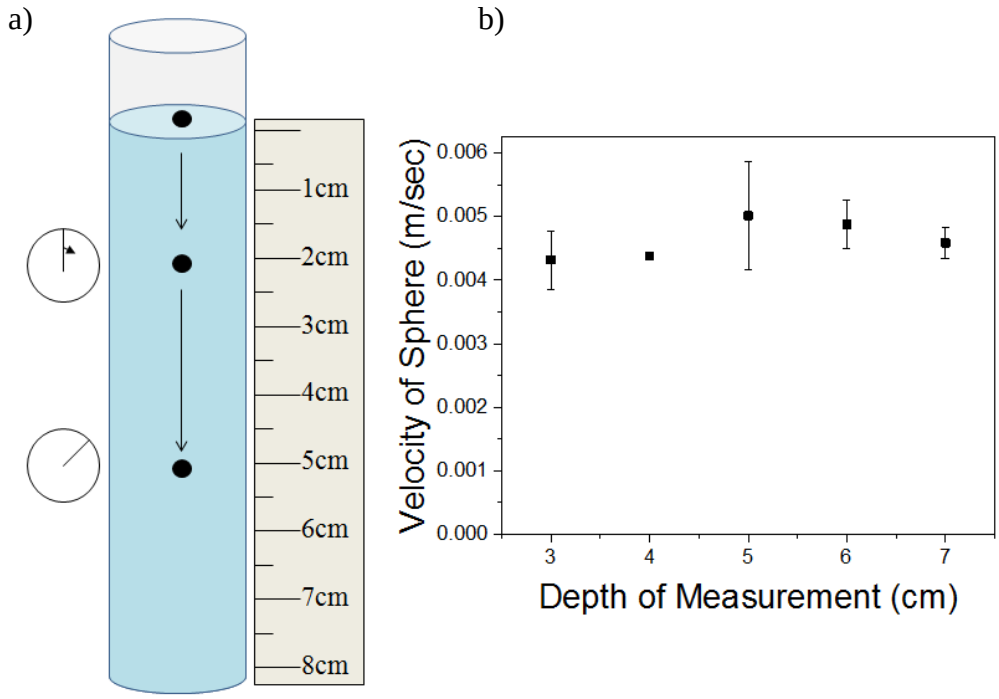

Figure 5.1: (a) Schematic diagram of the set-up for the ball drop experiment; (b) the depth of measurement vs measured velocity for the glycerol.

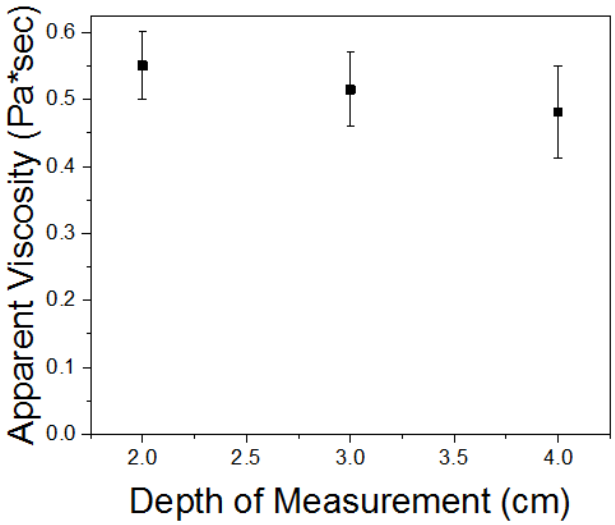

Figure 5.2: Calculated viscosity of the glass sphere in the glycerol.

From these data, a curve can be made using the velocity, measured at different depths to calculate the viscosity, as shown in Figure 5.2. The depth of measurement in

Figure 5.2 is designated by the centimeter marking at which the timer was started, e.g., the 3-cm marking in Figure 5.1a. Each of the measurements was repeated three to four times with a different ball.

Figure 5.2 shows the viscosity of the glycerol as determined in the experiment. The glycerol viscosity reported in literature (0.79 Pa*s[9]) was compared with these measurements. The comparison indicated that apparent viscosity measured here was within 30 % of the viscosity of glycerol reported elsewhere. Therefore, the experimental procedure was utilized to estimate the relative change of neat epoxy viscosity during the curing reaction.

5.2.3: Orientation of MagSiCWs in Epoxy at a Low Concentration

The orientation of the MagSiCWs in the epoxy resin was monitored using optical microscopy. To conduct the measurements, the magnetically modified whiskers were dispersed into methanol. Then, the MagSiCW methanol solution was added to the bisphenol-A epoxy and mixed. The methanol was then evaporated from the solution by nitrogen stream and vacuum pumped for 10–15 min. The MagSiCWs were dispersed into the neat epoxy resin at a 0.03 wt. % concentration. Next, DDSA hardener and tertiary amine catalyst were mixed with the MagSiCWs/epoxy in 1: 1.37: 0.07 proportions for the epoxy:hardener:catalyst. After mixing, the solution was vacuum pumped (to remove the bubbles) and then poured into the glass mold. Three layers of double-sided scotch tape were used as a separator between two glass slides comprising the mold. Two neodymium magnets were used to create a quasi-uniform 202 G magnetic field to align the whiskers. The whisker orientation was observed using Olympus MVX10 stereoscope (Figure 5.3).

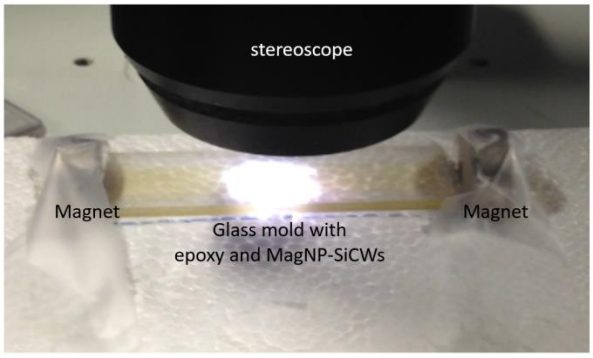

Figure 5.3: Experimental set-up for the observation of orientation of MagSiCWs at low concentration.

5.3: Results and Discussion

5.3.1: Epoxy Curing

The ball drop method was used to determine the apparent viscosity of the epoxy resin during curing. Specifically, the change in drag was monitored as a glass sphere moved through the epoxy resin[3-4]. The initial viscosity for the uncured resin was found to be 8.8 Pa*s. The change in apparent viscosity in the course of the curing calculated using Equation 5.1 is presented in Figure 5.4.

It was found that the epoxy resin reached the gel-point at ~45 hrs, where the measured viscosity increased exponentially. It is necessary to point out that viscosity measurements using a 2 mm diameter glass sphere does not capture fully local viscosity in the vicinity of the whisker being oriented in the epoxy resin. However, the working time for epoxy materials is dependent on the macroscale observations. Thus, the gel point and working time of the epoxy resin is determined to be ~45 hours at room temperature.

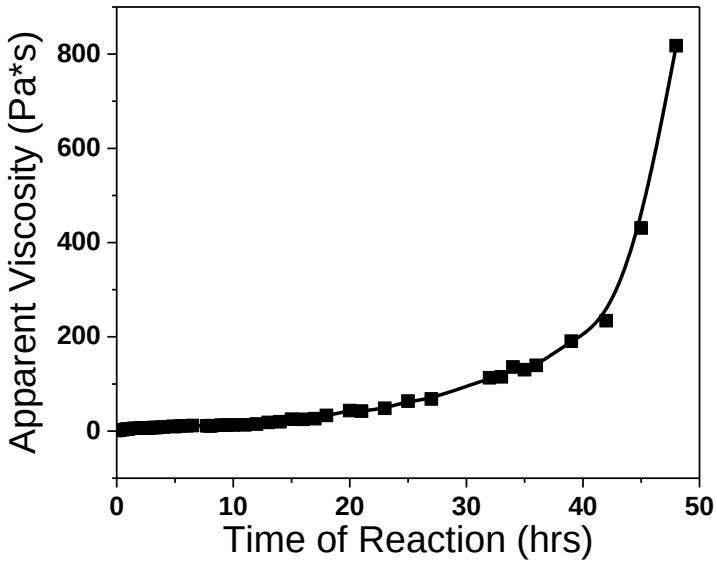

Figure 5.4: The apparent viscosity of the epoxy resin vs. the epoxy curing reaction time at room temperature.

To complement the viscosity measurement, DSC was used to monitor the extent of the curing reaction by measuring the magnitude of the released heat related to the polymerization process. The extent of the curing was determined after 3, 6, 12, 24, and 48 hours of the epoxy curing at room temperature[5]. The sample of interest was heated from 0 ^{o}C to 160 ^{o}C at 15 ^{o}C/min. Obtained exothermic peak (representing the amount of uncured epoxy at room temperature) was integrated to obtain the heat of the reaction[5]. The calculated value was divided by the initial exotherm (representing the "just prepared" epoxy resin) to yield the percentage of epoxy material that had not reacted. When subtracted from 100 % the value gave the extent (degree) of the reaction (Figure 5.5).

The reaction shows a linear trend of progression over time. After ~ 45 hours the resin reached gelation at room temperature with ~20 % of the material reacted. This left

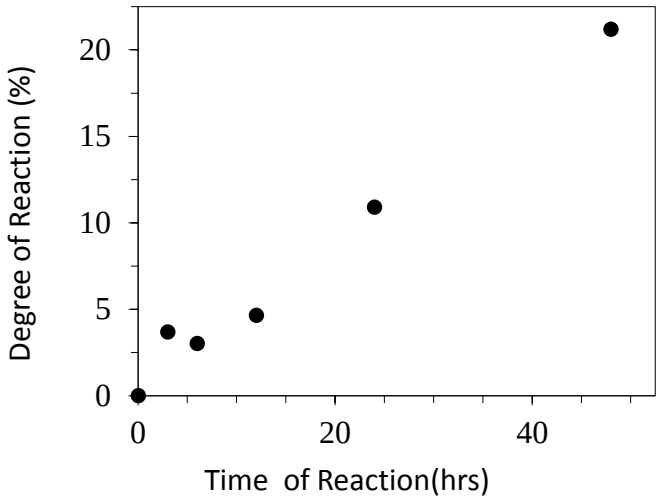

Figure 5.5: The degree of epoxy curing vs time of the reaction.

80 % of the epoxy matrix unreacted. This 80 % of the epoxy are cured at 75 ºC in our curing protocol. Therefore, in principle, curing of the epoxy resin at higher temperature where viscosity of epoxy resin is much lower, could change the orientation of the whiskers.

5.3.2: Modeling the Characteristic Time of Orientation

The model for predicting the characteristic time of magnetic orientation considered the governing forces (drag, moment of torque, and magnetic susceptibility) affecting the orientation in a viscous liquid. On contrary, inertial forces have a minor role in the dynamics of nanorods in a composite structure[8, 10]. Hence, the system for orientation is primarily controlled by the torque of an applied magnetic field countered by

the viscous drag of the media (where the torque on the magnetic materials depends on the type of magnetism and morphology of the magnetic system).

The iron oxide nanoparticles used in this work were shown to be paramagnetic (Chapter 4). Although the nanoparticle agglomerates are deposited on the surface of SiCWs, it is assumed here that the nanoparticle layer acts as a tubular paramagnetic unit when attached to the whiskers' surface. This first approximation was chosen to treat the functionalized SiCWs as a homogenous magnetic material. Thus, the magnetic moment resulting from an applied magnetic field will not deviate from the axis of a high aspect ratio paramagnetic material[11-12].

Equation 5.2 is used to determine the frequency of orientation for a paramagnetic rod[12-13]. The equation, describing the orientation of a single nanorod, is given by:

$$2\pi f_c = w_c \tag{5.2}$$

where f is the critical frequency of the whiskers rotation or $1/\tau$ (where: τ is the characteristic time of orientation for paramagnetic nanorods going from 90 ^{o} to 0 ^{o} orientation with the net director); and, w_c is the characteristic frequency, defined by:

$$w_c = \frac{1}{\gamma} \cdot \frac{2V_{mag}}{\mu_o} \cdot \frac{\chi^2}{2+\chi} \cdot B^2 \tag{5.3}$$

where χ is the magnetic susceptibility (~5.39, taken from the slope of the MagSiCW magnetometer measurement in Figure 4.11), B is the magnetic field (202 G), μ is the vacuum permeability ($4\pi \times 10^{7}$), V_{mag} is the volume of the magnetic material, and γ is the

drag coefficient[8, 11, 13]. The drag coefficient and volume of magnetic materials are defined as:

$$\gamma = \frac{\eta l_w^3 \pi}{3\ln(l_w / d_w) - A} \tag{5.4}$$

$$V_{mag} = \frac{\pi d_w}{4} \cdot (d_w^2 - d_{w+p}^2) \tag{5.5}$$

where η is the initial viscosity of the epoxy resin (~9 Pa*sec), d_w is the diameter of the whisker (400 nm), l_w is the average length of the whisker (4200 nm), d_{w+p} is the diameter of the whisker plus the particles (d_{w+p}>419 nm), and A ≈ 2.4[8].

Equations 5.3, 5.4, and 5.5 were combined and used to estimate the number of magnetic nanoparticles needed to create a reasonably practical characteristic time of orientation (Figure 5.6). The equations were applied to the starting parameters of the epoxy resin. The number of nanoparticles attached to the SiCWs was changed by increasing the thickness of the magnetic layer.

The characteristic time of orientation exponentially declines from 250 seconds as more particles are evenly distributed across the surface of the SiCW. Namely, the characteristic time is asymptotically approaching 10 sec. The typically fabricated MagSiCWs possessing a thickness of 110 nm of magnetic nanoparticles were estimated to have a 24.5 s characteristic time of orientation. Thus, to further evaluate the kinetics of MagSiCWs' rotation, the changes in apparent viscosity during curing were used to determine how the MagSiCWs would orient in the reacting matrix (Figure 5.7).

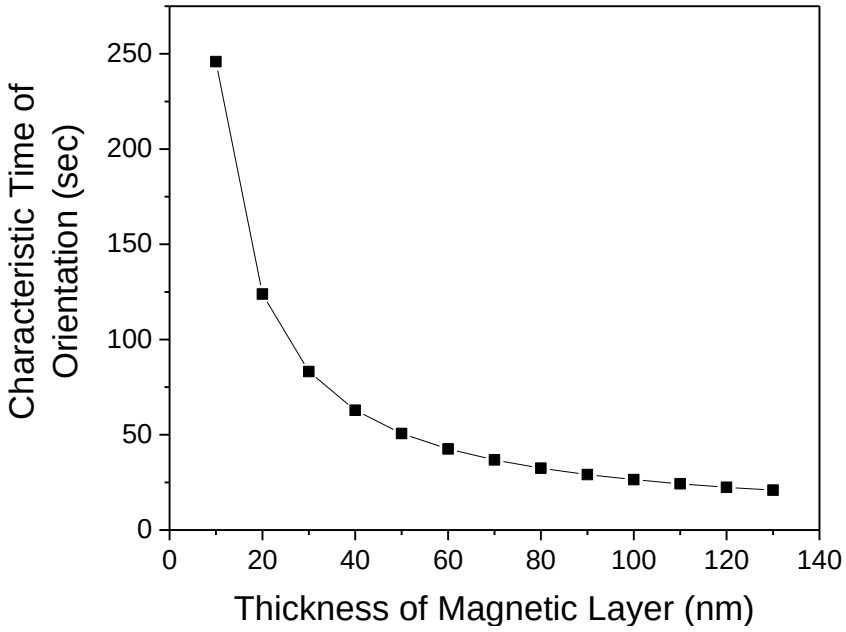

Figure 5.6: The calculated time of orientation vs. the thickness of attached MagNP within the initial epoxy resin.

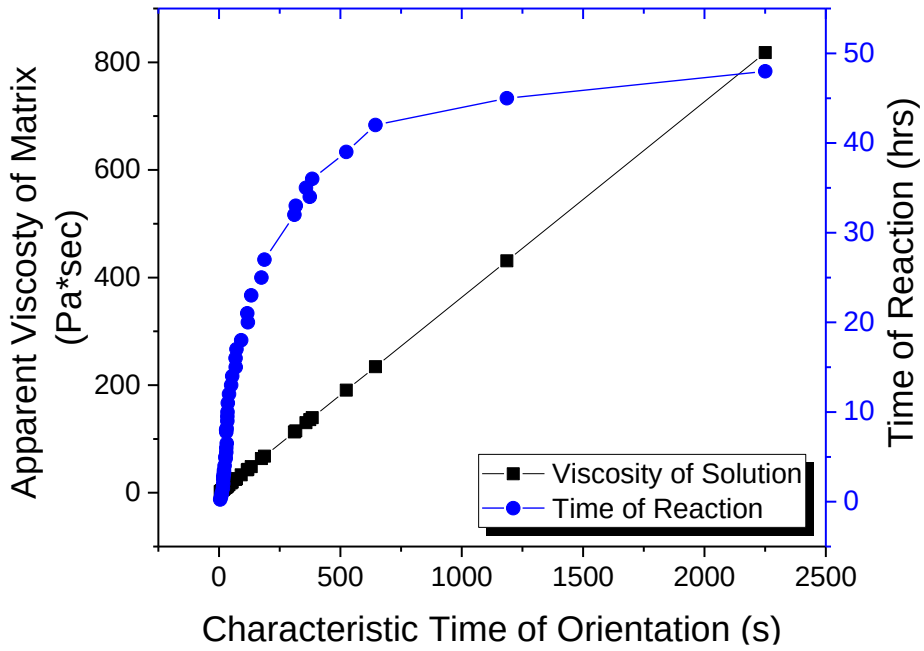

Figure 5.7: Calculated characteristic time of magnetic orientation for MagSiCWs.

The characteristic time is linearly dependent on the drag coefficient and

consequently, on viscosity of the medium. Hence, the viscosity will greatly limit the rotation of the whisker when the viscosity reaches 200 Pa*s or ~40 hours into the reaction (Figure 5.4). The characteristic time at this point would be equal to 10 min.

5.3.3: Magnetic Orientation of MagSiCWs in a Curing Epoxy Resin

The experimental assessment of the characteristic time for the rotation of MagSiCWs were performed in the low concentration orientation experiments during the curing of the neat epoxy system. Low concentration of the MagSiCWs was used to avoid indirect (ex: whisker-to-whisker resin mediated effects) and direct (ex: whisker-to-whisker contact) interactions. Figure 5.8 displays the time of orientation against the time

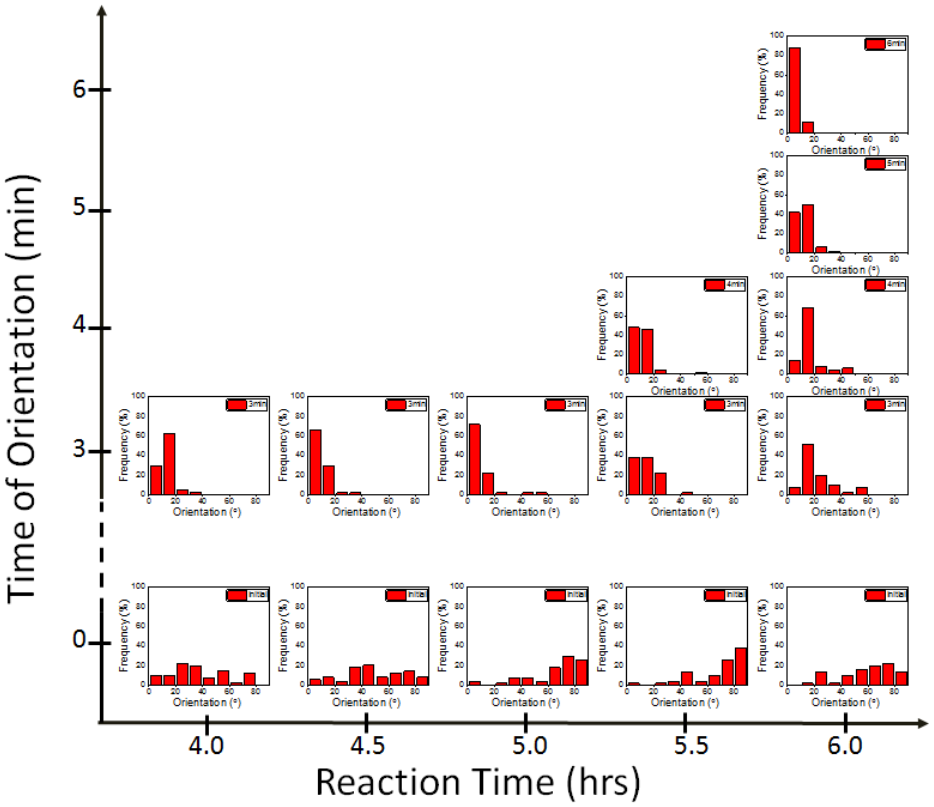

Figure 5.8: The distribution of MagSiCWs' orientation within a constant field (from images taken at specific reactionary times) during the curing process of the neat epoxy, as observed with optical microscopy.

of the curing reaction, where each point is a histogram showing the distribution of whisker at that time point. For each of these histograms, the orientation of 40–50 MagSiCWs was experimentally measured. It can be observed that the whiskers had random orientation prior to the application of magnetic field.

As, a constant 202 G magnetic field was applied to the samples the orientation of the whiskers was observed and monitored. Five hours into the reaction, the rotation of the whiskers slowed down significantly, although, the increase in the resin viscosity was just from 9 to 12 Pa*s. The epoxy matrix had only cured to a maximum of 5 % during this time span. In Figure 5.9, the time necessary for the orientation is plotted against the apparent viscosity of the epoxy material. The time of orientation was recorded when the average orientation of the whiskers was less than 10 ^{o} from the net director.

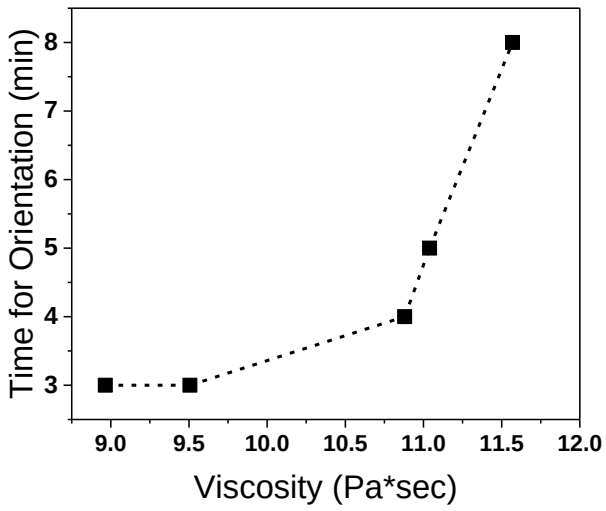

Figure 5.9: Experimentally measured time of orientation over the experimentally measured apparent viscosity.

The theoretical calculations showed a linear trend for the change of orientation time vs viscosity (Figure 5.7), therefore the exponential trend observed in the experiment (Figure 5.9) was unexpected. The trend shows that the real system is more complex than the model one. It was predicted via modeling that the orientation time for the whiskers would be on the level of seconds at these viscosities. However, their real orientation time was on a scale of minutes. In practical terms, it can be pointed that the orientation of whiskers must be done before the overall viscosity of the epoxy resin reaches 11.5 Pa*s or the reaction time reaches 6.5 hours. The deviation might be related to the local viscosity increases within the vicinity of the whiskers. It can be caused by grafting of the epoxy polymer to the whiskers via PAA on the MagSiCW's surface. Such grafting would increase the hydrodynamic radius of the whisker and, as the result, rise the drag value. The described changes would conclude in larger value of the characteristic time.

5.4: Conclusions

The following conclusions can be made as a result of the study reported in Chapter 5:

- The orientation time was predicted via modeling to have a linear trend with increase in the apparent viscosity. However, the orientation of the MagSiCWs in the experiment did not follow the model calculations.
- The experimental orientation time for the MagSiCWs increased exponentially as the reaction progressed from 4.5 hours to 6.5 hours. The whiskers required orientation time on a scale of minutes.

- It was hypothesized that the orientation of the MagSiCWs was influenced more by the local interaction of the curing epoxy resin with the whisker surface modified with the grafted layer of epoxy polymer.

5.5: References

1. Putz, K. W.; Palmeri, M. J.; Cohn, R. B.; Andrews, R.; Brinson, L. C., Effect of cross-link density on interphase creation in polymer nanocomposites. *Macromolecules* **2008,** *41* (18), 6752-6756.

2. Kim, B.; Choi, J.; Yang, S.; Yu, S.; Cho, M., Influence of crosslink density on the interfacial characteristics of epoxy nanocomposites. *Polymer* **2015,** *60*, 186-197.

3. Stokes, G. G., On the effect of the internal friction of fluids on the motion of pendulums. *Trans Cambridge Philos Soc* **1851,** *9*, 8-105.

4. Lamb, H., *Hydrodynamics*. 6th ed.; Cambridge University Press Cambridge, 1932.

5. Abenojara, J.; Encinasa, N.; del Realb, J. C.; Martínez, M. A., Polymerization kinetics of boron carbide/epoxy composites. *Thermochim Acta* **2014,** *575*, 144-150.

6. Gu, Y.; Kornev, K. G., Alignment of magnetic nanorods in solidifying films. *Part Part Syst Char* **2013,** *30* (11), 958-963.

7. Gu, Y.; Kornev, K. G., Ferromagnetic nanorods in applications to control of the in-plane anisotropy of composite films and for in situ characterization of the film rheology. *Adv Func Mater* **2016,** *26* (22), 3796-3808.

8. Tokarev, A.; Kaufman, B.; Gu, Y.; Andrukh, T.; Adler, P. H.; Kornev, K. G., Probing viscosity of nanoliter droplets of butterfly saliva by magnetic rotational spectroscopy. *Appl Phys Lett* **2013,** *102* (3), 33701.

9. Segur, J. B.; Oberstar, H. E., Viscosity of glycerol and its aqueous solutions. *Ind Eng Chem* **1951,** *43* (9), 2117-2120.

10. Tokarev, A.; Luzinov, I.; Owens, J. R.; Kornev, K. G., Magnetic rotational spectroscopy with nanorods to probe time-dependent rheology of microdroplets. *Langmuir* **2012,** *28* (26), 10064-71.

11. Frka-Petesic, B.; Erglis, K.; Berret, J. F.; Cebers, A.; Dupuis, V.; Fresnais, J.; Sandre, O.; Perzynski, R., Dynamics of paramagnetic nanostructured rods under rotating field. *J Magn Magn Mater* **2011,** *323* (10), 1309-1313.

12. Landau, L. D.; Lifshitz, E. M., *Electrodynamics of continuous media*. Pergamon: Oxford 1960.

13. Kornev , K. G.; Gu, Y.; Aprelev, P.; Tokarev, A., Magnetic rotational spectroscopy for probing rheology of nanoliter droplets and thin films. In

Characterization Tools for Nanoscience & Nanotechnology, Kumar, C., Ed. Springer: 2015; Vol. 6.

CHAPTER SIX

FABRICATION AND STUDY OF MAGNETICALLY ORIENTED SICW/EPOXY NANOCOMPOSITES

6.1: Introduction

The study of the orientation of the SiCWs showed that the working period for orientation was about 6 hours. However, this time is shorter than the one predicted by modeling. Therefore, it was hypothesized that the whiskers actively participate in the curing of the epoxy taking place in their vicinity. Namely, the surface carboxylic acid groups react with the epoxy functional groups causing the formation of an extended interphase zone[1-2]. To this end, this chapter describes an experiment aiming to clarify this matter. The MagSiCWs were extracted from the curing epoxy composite (after reacting for 5 hours) and examined using TGA and SEM. This experiment helped us to evaluate the level of grafting of the epoxy resin to the MagSiCWs. It is necessary to note that the mechanism and kinetics of the epoxy/anhydride curing have previously been investigated[3-6,7]. In addition, the effects of fillers and additives on the epoxy/anhydride resin systems have been studied for SiO_2 surfaces using DSC[7]. None of these studies considered the effect of surface chemistry on the epoxy curing reaction. Thus, in this part of the work DSC and ATR-FTIR were used to elucidate the influence of MagSiCWs on the curing reaction[4, 7].

The methodology for the magnetic orientation of MagSiCWs in epoxy composite materials was developed. Specifically, three methods of magnetic field application were used to find an optimal protocol to apply magnetic field for orientation of the SiCWs. Neat epoxy and the composite materials with oriented and non-oriented SiCWs were fabricated and their mechanical and thermal properties were evaluated. First, thermo-mechanical

properties were investigated using dynamic mechanical analysis (DMA). DMA provided insights into the interfacial and structural aspect of the mechanical properties[8-11]. Second, the thermal properties of the composite materials were investigated using DSC. DSC analysis contributed additional information on the composites' T_g[12-14]. The glass transition and thermo-mechanical behavior of the composites have been used to investigate the interphase zone[1, 8, 14-16]. Additionally, the composite materials' magnetic properties were studied. After characterization of the composites, their microstructure was investigated using variable pressure SEM and swelling experiments[9].

6.2: Experimental

6.2.1: Fabrication of the Composites

The 5 mg/ml methanol suspension of MagSiCWs was mixed with pure epoxy resin, DGEBA, and dried overnight under a stream of nitrogen to remove methanol. Then, the epoxy resin was prepared at 0.41:0.56:0.03 volume ratios between DGEBA/dodecyl succinic anhydride (DDSA) hardener/N-benzyl dimethyl amine (BDMA) catalysts. Then, the resin was vacuumized to remove any air bubbles created during mixing. The same procedure was utilized for the fabrication of the neat epoxy resins used in this work for comparison purpose.

After the material was prepared, the resin suspensions of MagSiCWs were poured into a Teflon mold. Teflon was chosen because it is one of the few materials epoxy does not adhere to and it is thermally stable at the curing temperature of the epoxy. The epoxy resin was cured at room temperature until the gelation point (about 48 hours) and, then, placed into an oven for 24 hours at 75 ^{o}C to complete the curing process. Parameters of curing kinetics, whiskers content in the matrix, T_g and the degree of curing were

determined using DSC and ATR-FTIR, TGA and DSC, respectively. In addition, SEM imaging was utilized for characterization of the composite morphology, optical microscope was used to observe orientation kinetics, and DMA was employed to obtain T_g and moduli of the nanocomposites.

6.2.2: Curing Kinetics Monitored using DSC

The exothermic peaks related to the epoxy curing process were recorded with DSC using a methodology described elsewhere[17]. The DSC measurements were carried out for samples initially cured at room temperature for 3, 6, 12, 24, and 48 hours.

6.2.3: Curing Kinetics Monitored using FTIR

The utilization of the ATR-FTIR technique allowed acquiring IR spectra with very little material used. As the prepared epoxy and composite resins were curing at room temperature (at ambient humidity), the samples were drop casted by a glass pipette onto an ATR crystal at 0, 3, 6, 12, 24 and 48 hours into the reaction. The obtained results were converted to the degree of reaction by integrating the 913 cm^{-1} and 1780 cm^{-1} FTIR peaks of epoxy and anhydride functional groups involved in the curing. The initial values for spectral peaks were normalized to the 1470 cm^{-1} methyl peak. The 1470 cm^{-1} peak was chosen because the methyl groups are not involved in the reaction and the area under the peak was approximately the same throughout the course of the reaction. Then, Equation 6.1 was used to calculate the degree of reacted functional groups (α):

$$\alpha = \left(1 - \frac{A_t}{A_o}\right) * 100 \qquad (6.1)$$

where, A_t and A_o – normalized peak's area for the time *t* and original area at time 0, respectively.

6.2.4: Determination of the Amount of Epoxy Grafted to MagSiCWs

The whiskers were mixed with the epoxy resin of the given composition (as stated previously). Then, the mixture was left to react for 5 hours and then was dissolved in methanol. From this solution, the whiskers were magnetically separated for further analysis. Four cleaning cycles of rinsing with methanol were performed to remove non-grafted epoxy. The difference between the MagSiCWs removed from the epoxy and original MagSiCWs' surface structure was investigated using TGA and SEM/TEM. The TGA was used to determine the addition weight gain by the whiskers due to the epoxy grafting. The TGA runs were performed up to 750 ^{o}C at 20 ^{o}C/min in a dry air environment. The surface morphology of the MagSiCWs was imaged by Hitachi HD2000 SEM/TEM. For the imaging the samples were dispersed in MEK and drop-casted onto a Formvar carbon, and copper wire TEM grids.

6.2.5: Orientation of MagSiCWs in Epoxy Resin

A 216 G magnetic field was used to orient the MagSiCWs in the epoxy matrix. Three different methods were conceived and studied to determine the method that provides the highest degree of the whiskers orientation. The magnetic field was applied after the composite resin had already been cast into the mold. The first method of orientation was called the *'singular'* method. It was a one-time magnetic alignment for 15 min. at 1, 2, or 3.5 hours into the curing process. The next method of orientation was called the '*pulsed'* method. It included a pulsed magnetic alignment applied to a single sample for 15 min. at 4 separate times, 1, 2, 3.5, and 5 hours during the curing of the epoxy resin. The last method of orientation was called the '*continuous'* alignment method. In the method magnetic field was applied to the composite continuously for the 5 hours of the curing process.

6.2.6: Thermo-Mechanical Characterization by DMA

Neat epoxy, non-oriented nanocomposites, and oriented nanocomposites were fabricated for the DMA testing. They were casted into the mold with a length of ~8.00 mm, a width of ~5.00 mm, and a thickness of ~0.34 mm. Then, the 'pulsed' orientation method was utilized to align the MagSiCWs. After the curing process, the composite samples were extracted from the Teflon mold and tested. The DMA testing was run at 2 ^{o}C/min from -20 ^{o}C to 150 ^{o}C using frequencies of 1, 2, and 5 Hz applying 5 μm amplitude of oscillation. Three to four parallel samples were fabricated and analyzed.

6.2.6: Thermal Characterization using DSC

The DSC samples were prepared from the mold-casted epoxy and thermally cured and composite samples. They were weighed in the range of 5–10 mg and sealed into an aluminum pan with an aluminum lid. The first DSC run was from -10 ^{o}C to 150 ^{o}C at 15 ^{o}C/min. Then, the samples were cooled to -10 ^{o}C at 15 ^{o}C/min and run for the second time from -10 ^{o}C to 150 ^{o}C at 15 ^{o}C/min.

6.2.7: Magnetic Characterization of the Composite Materials

The samples of the composite materials were cut into 3x3 mm squares with a thickness of approximately 0.34 mm. The average difference between the side lengths was 0.2 mm. Magnetization curves were measured for two samples of non-oriented composite and three samples of oriented composite. Samples of nanocomposite materials were cut into 3-mm squares having a thickness of approximately 0.34 mm. The average difference in length between the sides of the squares was 200 μm. Magnetic hysteresis loops were measured for two samples of nanocomposite with non-oriented embedded nanorods and three samples of nanocomposite with oriented embedded nanorods. For each sample, two

magnetic hysteresis measurements were performed: one measurement with the magnetic field oriented along one side of the sample and the other measurement with the magnetic field oriented along the other side of the sample. By comparing the hysteresis loops along each side of the sample, an estimation of magnetic anisotropy was made for oriented and non-oriented nanocomposites. Magnetic characterization and data interpretation was conducted by Pavel Aprelev under the guidance of Prof. K. Kornev.

6.2.8: SEM Analysis of Composites' Microstructure

SEM was used to evaluate the microstructure of the composite materials. The samples were dipped into liquid nitrogen and broken in the longitudinal direction. The samples were then attached to an aluminum SEM puck with a carbon tape to have the broken edge facing a detector. The distribution and orientation of the nanoparticulates were analyzed manually using Gwyddion software. The distribution of the SiCWs in the matrix was evaluated by selecting 25–35 random whiskers per an image and measuring the distance to the next closest whiskers (usually 8–13 whiskers). The distance was measured between the centers of the whiskers. The orientation was analyzed by identifying the whiskers' shape and drawing a line through the center of the whisker going from one end of the whisker to another end. Then, the orientation from the set net director was calculated using the Gwyddion software. There were some groups/agglomerates of whiskers within the composite matrix. These agglomerates were counted and the number per unit area of the sample was calculated. This procedure was performed for two to three images and two different samples for each set. The size of the agglomerates was determined by drawing a box around them and measuring its size.

6.2.9: Determination of Composites' Cross-Linking Density

In a thermoset composite material, cross-linking density is one of the most important structural characteristics. The density of cross-links can be determined using statistical thermodynamics of elasticity and data on swelling of the thermoset in a solvent[9]. The thermodynamic expression involving cross-linking density is presented in its simplified form in Equation 6.2[9]:

$$E_{Mc} \approx \frac{\rho_{x-link}}{2} RT \tag{6.2}$$

where E_{Mc} represents the modulus of the material 40 degrees past the mechanical T_g (denoted by the loss modulus peak), R is the gas constant, T is the temperature in Kelvin of E_{Mc}, and $\rho_{x\text{-}link}$ is the cross-linking density[9].

The swelling experiment relied on the diffusion of a solvent into the cross-linked composite. Acetone was chosen as the solvent, as it is a good solvent for phthalic anhydride cross-linked epoxy[18]. The weight of the sample was measured before and after the swelling. The swelling maximum for the composite was reached after ~24 hours in the solvent. Therefore, the composite samples were placed into a glass vial containing 10–15 ml of acetone and left in dark at room temperature for 24 hours. The weight gain of the sample is equivalent to the amount of solvent swelling the sample. The swelling data was used to calculate the cross-linking density using the Flory-Rhener expression for the tetra functional affine network, Equation 6.3[9]:

$$\rho_{x-link} = 2 * \frac{\ln(1-v_2)+v_2+\chi v_2^2}{V_1(\frac{v_2}{2}-v_2^{1/3})} \tag{6.3}$$

where ρ_{x-link} is the cross-linking density, v_2 is the volume fraction of the polymer at equilibrium, χ is the polymer-solvent interaction parameter (~0.4[18]), and V_1 is the molar volume of the solvent. For this experiment, v_2 was determined using Equation 6.4:

$$v_2 = (1 + \left(\frac{m_{eq} - m_d}{m_d}\right)\left(\frac{\rho_2}{\rho_1}\right))^{-1} \quad (6.4)$$

where ρ_1 and ρ_2 are the densities of the polymer (~1 g/cm^3) and solvent (0.79 g/cm^3), and m_d and m_{eq} are the dried mass and swollen mass of the composite materials. Thus, by the change in weight of the material due to swelling, a rough estimate of the cross-linking density can be made.

6.3: Results and Discussion

6.3.1: Curing of Epoxy Resin in the Presence of MagSiCWs

The study of chemical reaction between functional groups on the MagSiCW's surface and epoxy resin is described in this section. It is well-known that carboxylic acid groups, of PAA, can react with epoxy[19]. Therefore, DSC and ATR-FTIR were used to study the kinetics of the epoxy resin curing in the presence of the MagSiCWs. First, DSC was used to investigate the extent of the reaction. Then, ATR-FTIR was used to determine the chemical pathway of the epoxy curing.

Studies of Epoxy Curing using DSC

The degree of epoxy curing at room temperature for the composites was monitored and compared with the one determined for neat epoxy polymerization (Figure 6.1). The obtained results showed that the whiskers changed the curing rate. In the presence of the whiskers, the resin cured ~20 % faster than the neat epoxy, indicating that the whiskers

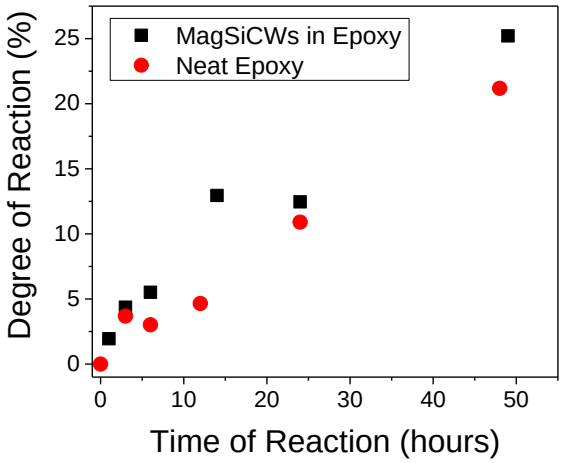

Figure 6.1: The degree of epoxy curing over the time of reaction at room temperature

chemically interacted with the curing matrix. To further investigate the effect of MagSiCWs on the polymerization of epoxy, the temperature of the curing was varied to evaluate the activation energy (E_a) of the reaction. The E_a for the neat epoxy and the epoxy with MagSiCWs were determined using DSC. The Kissinger method was used, as published elsewhere[7]. The experimental results are shown in Figure 6.2, where the heating rate divided by T_p squared (T_p - peak temperature of the reaction exotherm) is plotted versus $1/T_p$.

The slope of this line was taken as E_a/R, from the Arrhenius-like equation proposed by Kissinger:

$$\ln\left(\frac{heating\ rate}{T_p^2}\right) = -\frac{E_a}{RT_p} + \ln(A) \qquad (6.4)$$

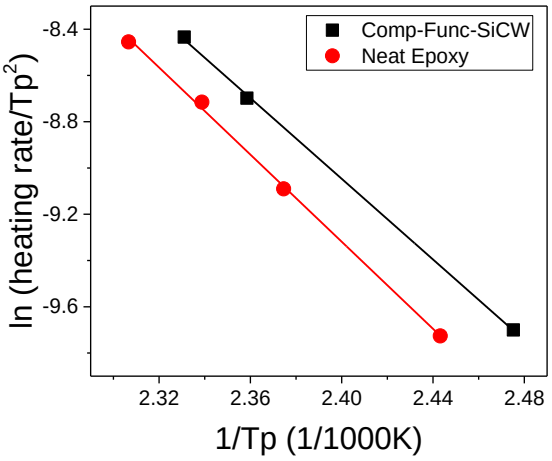

Figure 6.2: The plot of ln(heating rate/T_p^2) vs. $1/T_p$

where the heating rate value is from the DSC experiments, T_p is the peak temperature, E_a is the activation energy for the reaction, R is the gas constant, and A is the pre-exponential factor.

The E_a of the neat epoxy and the composite were 78.2 J/mol and 72.5 J/mol, respectively. MagSiCWs can be considered to be a reaction accelerant due to a 6 J/mol decrease in the activation energy[7] caused by the presence of the whiskers.

The increased rate of polymerization may cause changes in the structure of the matrix and cross-linking density in comparison to the neat epoxy system[7, 20]. It is suggested that the change in the polymerization is related to the high concentration of PAA carboxyl groups on the surface of the whiskers. This indicates that PAA creates an alternative reactive pathway that accelerates the curing at the beginning of the process. In turn, these changes in local concentrations are hypothesized to change the matrix structure. Thus, ATR-FTIR was used to characterize the mechanism of the curing reaction[4].

Studies of Epoxy Curing using ATR-FTIR

As the main components of the epoxy resin system, the epoxy and the anhydride IR peaks were followed throughout the course of the curing. Figure 6.3 shows the change in the epoxy functional groups' concentration over the time of the polymerization reaction at room temperature. It is found that the neat epoxy has a much higher consumption of epoxy groups than the composite material. Additionally, the neat epoxy exhibits a significant consumption (from 0 % to 26 %) of epoxy groups in the first 3 hours into the reaction. Then, the reaction progresses somewhat linearly until 48 hours into the curing. On the contrary, the composite consumes epoxy groups in a nearly linear fashion, at a rate of about 1 % of epoxy groups per hour.

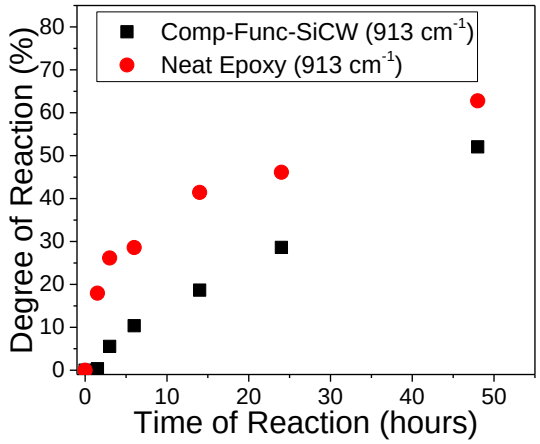

Figure 6.3: The kinetics of the epoxy functional groups consumption during the curing reaction at room temperature.

Next, Figure 6.4 shows the change in the anhydride consumption throughout the curing. The neat epoxy has a much lower consumption of anhydride than the composite system. Both curves progress quasi-linearly at a rate of 0.7 % and 1.5 % of anhydride

groups consumed per hour for the neat epoxy and the composite, respectively. Based on these results, a diagram of the reaction was compiled to show how the composition of the epoxy resin is changing with the curing extent (Figure 6.5).

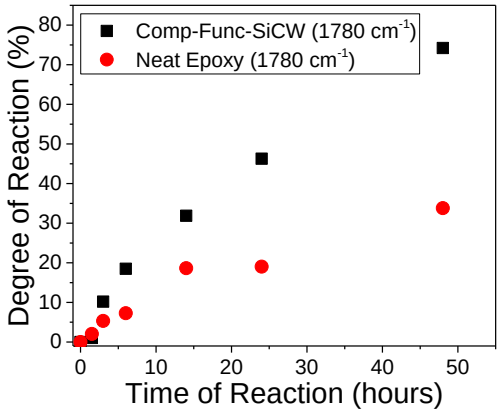

Figure 6.4: The kinetics of anhydride consumption during the epoxy curing reaction at room temperature.

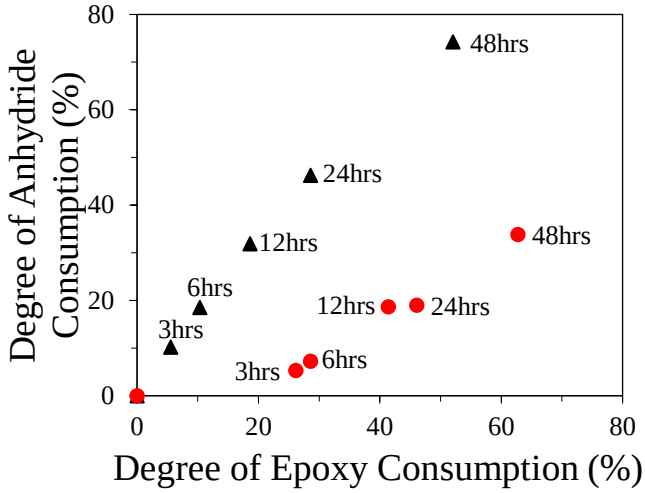

Figure 6.5: Change in the epoxy resin composition during the course of the curing reaction for the composite materials (▲) and the neat epoxy resin (●).

The reaction pathway is directly related to the chemical reactions between the substances in the material. For instance, if the dependence is linear, the curing is due to a

1:1 reaction of the epoxy and the anhydrides. In turn, the epoxy group consumption is favored in the neat epoxy resin, and the anhydride groups consumption is favored in the composite epoxy system. Hence, the functionalized whiskers cause the polymerization process to change its chemical pathway to the preferential consumption of the DDSA to form ester or acid linkages bonds with the acrylic acid or epoxy groups[3]. It is necessary to point out that the change in the chemical processes occurring during the epoxy polymerization can change the internal structure of the composite materials.

6.3.2: Grafting of Epoxy Polymer to MagSiCWs

Now that the change in the polymerization process is observed, the possibility of grafting epoxy polymer to MagSiCWs was investigated. First, TGA was used to determine if the anchoring of epoxy polymer to the MagSiCWs' surface (Figure 6.6) is occurring.

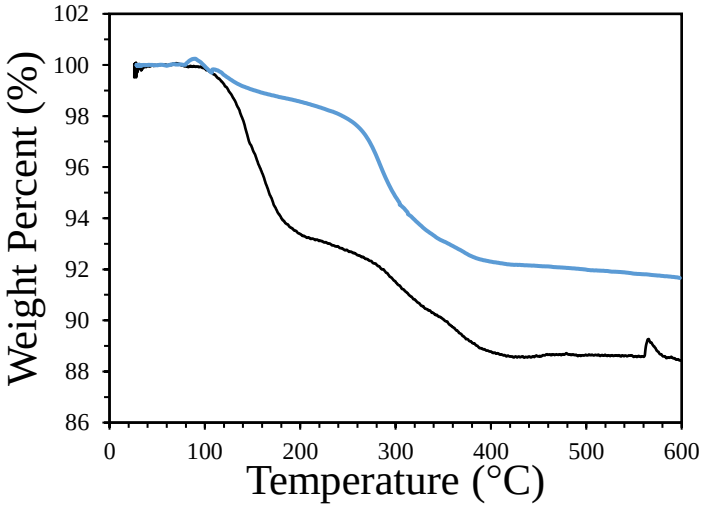

Figure 6.6: TGA curves for MagSiCWs soaked in epoxy for 6 hours (—) and original MagSiCWs (—).

The TGA data shown in Figure 6.6 revealed that epoxy polymer was grafted to the whiskers. Indeed, the MagSiCWs separated from the resin lost 11.4 wt. %, while the non-reacted MagSiCWs lost just 8.0 wt. % when heated up to 600 ^{o}C. The average surface coverage was calculated using Equation 3.5. It was found that the MagSiCWs were covered with the polymer layer of 12 nm thickness. This would translate to a swelled polymer layer on the order of 60–120 nm from surface. (The estimation is based on the swelling ability of polymer brushes[21].) Next, the surface morphology of the MagSiCWs reacted with the epoxy was imaged using TEM. Figure 6.7 shows the morphology of the SiCW after curing in the epoxy for 6 hours. The grafted epoxy is not clearly seen in the image. Therefore, the

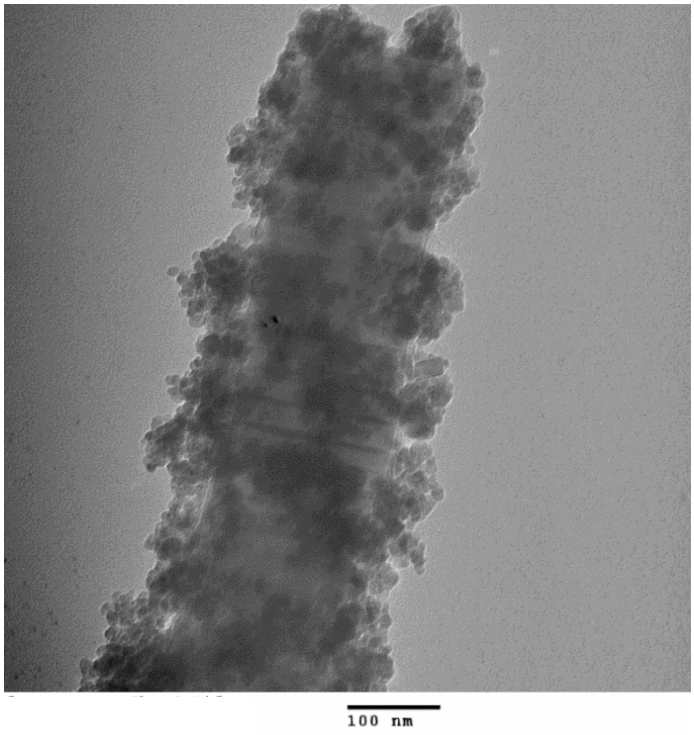

Figure 6.7: TEM image of the MagSiCWs' surface after soaking in the curing epoxy resin for 6 hours.

growth of the epoxy chains is suggested to be within the agglomerated MagNPs attached

to the SiCWs. Thus, it could be concluded that the epoxy polymer interpenetrated the agglomerate structures and created a MagNPs/PAA/Epoxy/DDSA composite as the interphase.

6.3.3: Magnetic Orientation Methods for MagSiCWs in the Epoxy Resin

The 'singular', 'pulsed', and 'continuous' magnetic field application methods were used to determine the most effective methodology for the orientation of MagSiCWs at 3 vol. % in the epoxy matrix. To observe the orientation the samples were broken in liquid nitrogen in the longitudinal direction and imaged. The typical images are shown in Figure 6.8. The images clearly show the microstructure of the nanocomposites, such as, the particulates' spatial distribution and orientation. It is obvious that the orientation of the whiskers in the composite is directly related to the applied magnetic field. A histogram of the level of the MagSiCWs' orientation is plotted in Figure 6.9 for the different magnetic field application methods.

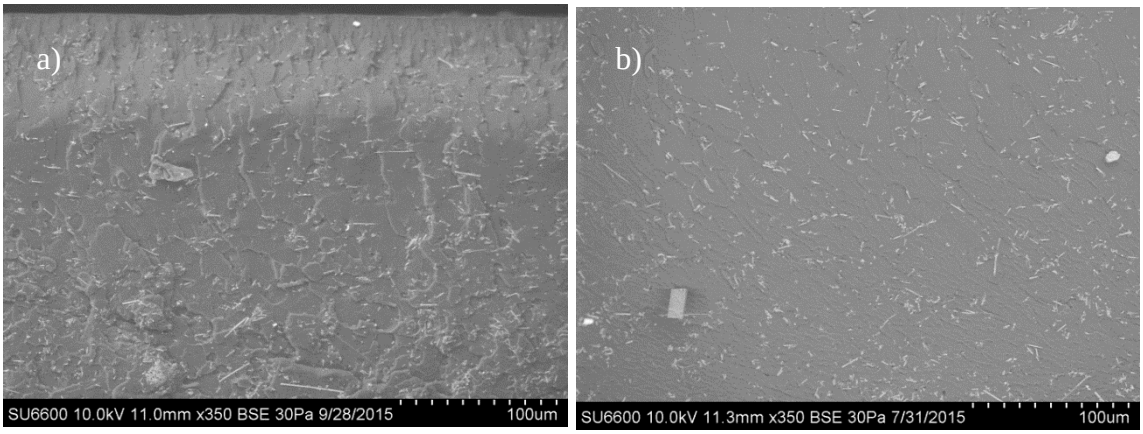

Figure 6.8: SEM images of composite materials (a) with a magnetic orientation and (b) without a magnetic orientation.

The distribution was determined from the measurement of 450–600 different whiskers from two to three images for each sample made. The ‘singular’ method had three parallel samples, while the ‘pulsed’ and ‘continuous’ methods had two parallel samples.

The comparison between the methods of magnetic alignment indicated that the 'pulsed' method of alignment resulted in the highest degree of orientation. The average orientation for the ‘pulsed’ alignment had an average orientation of 24^{o} from the net director. In contrast, the average orientation for the ‘singular’ and ‘continuous’ methods were 36^{o} and 30^{o}, respectively. We suggest that in the ‘singular’ alignment method, local internal stresses developed during the curing of the epoxy and the associated matrix relaxation decreased the level of the orientation after the magnetic field was released. In addition, the total orientation time in this method was significantly shorter than for the ‘pulsed’ and ‘continuous’ methods. In the ‘continuous’ method the sample was influenced by the magnetic field for an extended period enabling MagSiCWs to attain higher level of alignment and preventing possible relaxation of the whiskers. However, with an extended application of the magnetic field the migration of the whiskers to the magnets was initiated. Therefore, we concluded that the migration could disrupt uniformity of the distribution of the whiskers in the epoxy matrix. Conversely, the short-term application of the magnetic field in the ‘pulsed’ method allowed high orientation levels to be attained due to the sufficiently long cumulative time of interaction with the magnetic field and prevention of excessive relaxation resulting from repetitive application. Hence, the ‘pulsed’ method was selected for fabrication of the nanocomposite materials in this research.

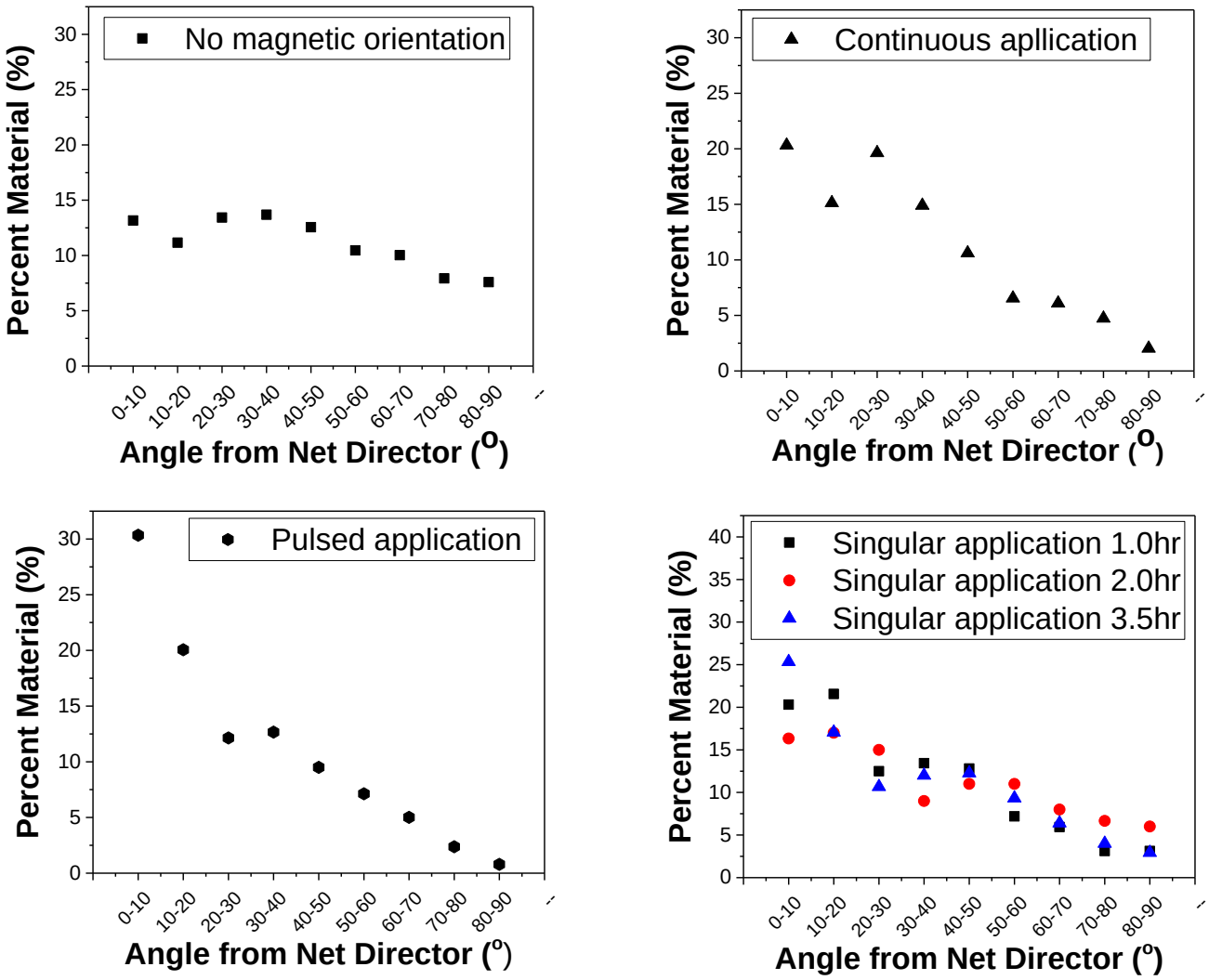

Figure 6.9: The level of MagSiCWs orientation in epoxy composite for the different methods of magnetic field application. *Continuous:* the continuous application of magnetic field to the composite for 4 hours (from 1hr to 5hrs into the curing). *Singular:* the magnetic field was applied once for 15 mins at 1, 2, or 3.5 hrs (one application per sample) during the curing. *Pulsed:* magnetic field was applied to a single sample for 15min 4 times (at 1, 2, 3.5 and 5 hours) during the curing.

6.3.4: Properties of the MagSiCW/Epoxy Composite Materials

Interphase formation

Thermal transitions and mechanical behavior of nanocomposite materials have been reported to significantly deviate from the values recorded for the unfilled polymer matrix.[1, 14-15, 22-27] The observed positive or negative deviations are associated with the formation of an interphase in the vicinity of the nanoscale filler. The polymer chains involved in the interphase demonstrated fundamental changes in mobility (relaxation time) due to interaction with the filler surface. In the nanocomposites (possessing a high ratio between the surface of the filler and the volume of the matrix), extended interphase zones were found, which can percolate through the entire nanocomposite and dominate the properties of the material.[1] In addition, for thermoset materials (like epoxy resins) synthesized in the presence of the nanoscale filler, chemical reaction and/or interaction between the monomers and the surface can also change the chemical structure of the polymer materials, such as cross-linking density.

In general, formation of extended interphases has been reported for epoxy nanocomposites. Using microscopy and nanoindentation methods the extent of the interfacial region in the composites was determined to be between tens of nanometers and several microns.[1, 14, 22-23, 28-30] If the surface of the filler was interacting with the epoxy matrix, formation of interphases with thicknesses between hundreds of nanometers and several microns were reported.[28, 31-32] In terms of mechanical properties, the interphase region can demonstrate a higher or lower modulus in comparison to the bulk polymer. Within a single interphase, variation of the modulus from lower to higher values compared

to the modulus for the bulk material was reported as well.[28] We note that in some examples the glass transition temperature (T_g) of the epoxy composite material increased through incorporation of the nanoscale filler, indicating formation of an interphase possessing a higher glass transition temperature.[1, 14] Conversely, many examples of depressed T_g are reported for epoxy composites.[1]

Because the influence of the MagSiCWs on the curing process is significant, we assume the formation of interphases in the nanocomposites with thicknesses between hundreds of nanometers and several microns. We can identify at least three distinct structural domains in the nanocomposite material: (A) an MagNP layer impregnated with epoxy polymer with the thickness of approximately 110 nm and the epoxy matrix near the layer, (B) a domain located next to the domain A, and (C) an epoxy network unaffected by the presence of the MagSiCWs. The domains A and B constitute the interphase in the nanocomposite.

Thermal characterization of the nanocomposites

We conducted DSC studies of the nanocomposites to observe the behavior of the epoxy materials in the T_g region. Figure 6.10a illustrates that the behavior of the "as fabricated" neat epoxy and nanocomposite materials is quite different in the T_g region. The neat epoxy and non-oriented composite clearly demonstrated enthalpic relaxations associated with the transition from a nonequilibrium conformational state of the polymer chains to an equilibrium state upon annealing.[14] The midpoint T_g value of the neat epoxy was observed to be ~ 60^{o}C and is approximately 13^{o}C higher than that of the non-oriented composite. The observed result indicated formation of an extended interphase with a lower T_g value

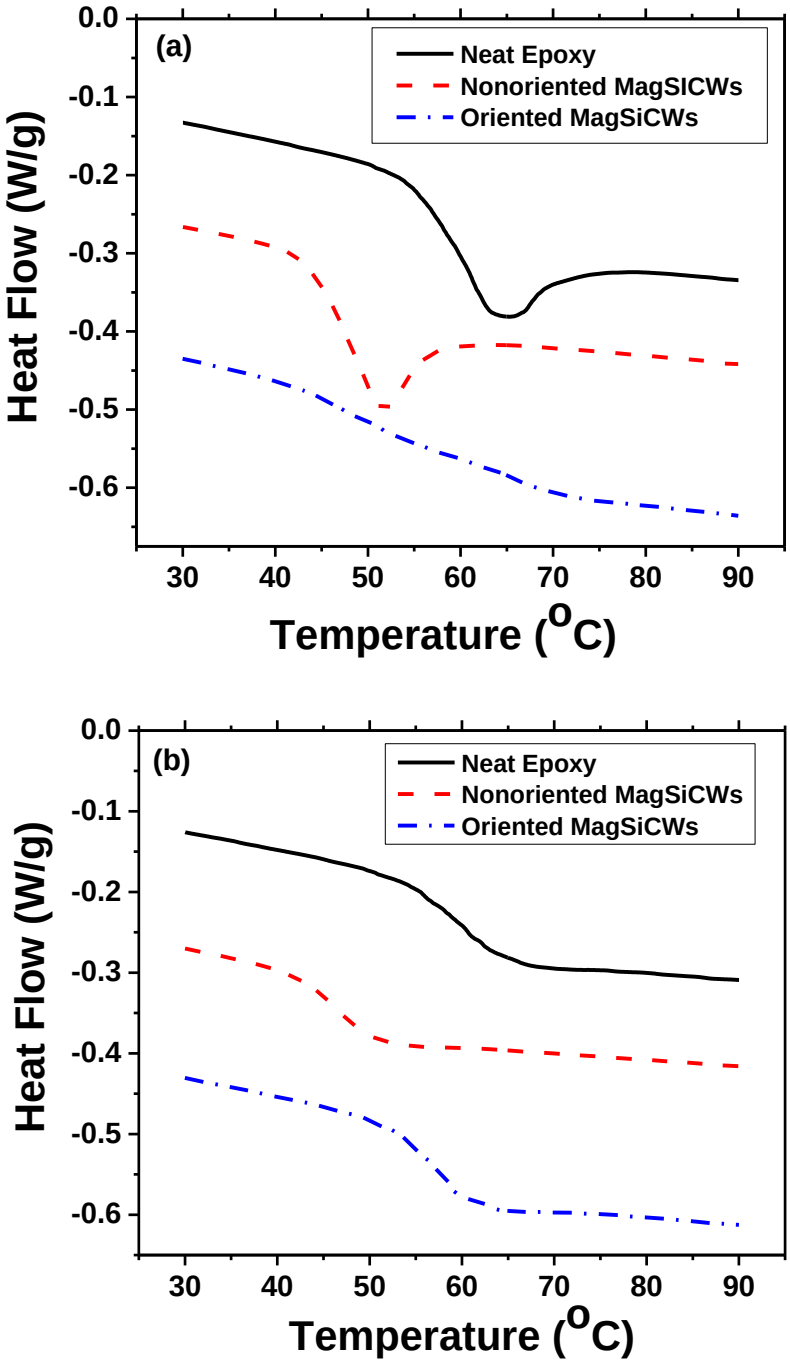

Figure 6.10: DSC traces for neat epoxy and epoxy/MagSiCW nanocomposites. (a) is the first run and (b) is the second run.

near the MagSiCWs. The magnetic orientation of the whiskers dramatically changes the behavior of the material upon heating. The oriented composite has a T_g transition where the midpoint T_g value is only about 2°C less than that of the neat epoxy. The DSC measurements also revealed that the oriented composite had no visible enthalpic relaxation and had an exceptionally extended (~30°C) T_g region. The region starts at the similar to non-oriented composite temperature and ends at the temperature higher than that for the neat epoxy. The observed results point to the formation of an extended interphase where both higher T_g and lower T_g zones are present.

From our analysis of the experimental results we propose the following coarse-grained model for the oriented and non-oriented epoxy-MagSiCW composite material. We suggest that the low T_g region (domain A with polymer chains possessing higher mobility than bulk epoxy) is located closer to the whisker surface and is associated with epoxy network disruption caused by the highly porous layer of nanoparticles and the high concentration of carboxylic groups of PAA. Domain B has a higher T_g value than the neat epoxy with chains having lower mobility caused by connectivity of the cross-linked chains to the solid surface via the chains involved in the domain A. Such behavior of the interfacial region in epoxy composites has been experimentally observed via nanomechanical measurements.[28] From straightforward geometrical considerations, it is obvious that the volume fraction of domain B in the oriented composites is higher than in the non-oriented material. The reason is the significant overlap between domains B for the randomly distributed whiskers. Therefore, in the oriented composite, where the higher T_g value of

domain B compensates for the lower T_g value of domain A, the glass transition temperature approaches that of the neat epoxy material. In the non-oriented nanocomposite, having a smaller extent of domain B, the T_g compensation does not occur.

Figure 6.10b demonstrates the DSC results for the second run, in which the fabrication history of the materials is erased via annealing. The DSC traces now show no visible signs of enthalpic relaxations indicating that polymer chains in the epoxy approach their equilibrium conformations. In general, the midpoint T_g values are similar to the ones obtained for "as fabricated" materials. The T_g region of the oriented composite materials is reduced in breadth and is comparable to the T_g value of the neat epoxy matrix, whereas the non-oriented composites again demonstrated lower T_g values. The obtained results indicated that the proposed coarse-grain model for the composite materials can be applied for the annealed samples as well, and the differences in T_g values of different materials are not artefacts of the fabrication procedure.

Thermomechanical properties of the nanocomposites

The neat epoxy, the epoxy with randomly orientated MagSiCWs, and the directionally oriented MagSiCW nanocomposites were tested by tensile DMA to evaluate their mechanical properties at different temperatures. The dependence of the storage modulus, E' for the materials is presented in Figure 11a. It is evident that below T_g the composites exhibited higher modulus than the pure epoxy matrix pointing to the efficient stress transfer from the matrix to the whiskers in the mechanical measurements. The room temperature value of E' for the neat epoxy was 1.52 ± 0.02 GPa. The randomly oriented

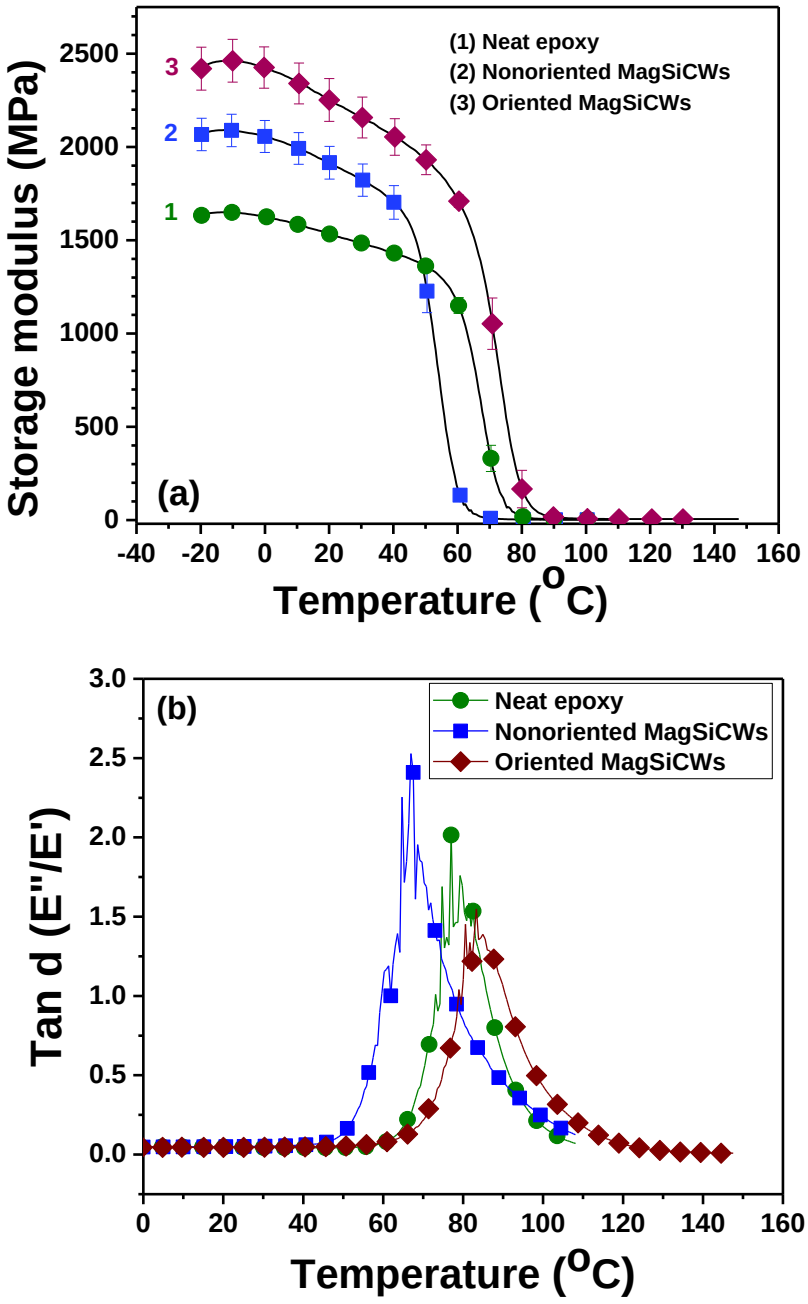

Figure 6.11: DMA results: (a) the storage modulus, E/ and (b) tan δ data for neat epoxy and epoxy/MagSiCW composites.

nanocomposite had a tensile modulus of 1.9 ± 0.1 GPa. The material with aligned MagSiCWs had a tensile modulus of 2.2 ± 0.1 GPa measured in the direction of the fiber orientation. These results reveal approximately 25% improvement was attained by just adding the filler and an approximately 45% increase in the modulus was realized by adding the MagSiCWs and orientating them.

We compared the obtained storage modulus values with those predicted by the Halpin-Tsai model that is commonly used for estimation of nanocomposite mechanical properties.[27, 33-34] The Halpin-Tsai model is a semi-empirical equation for prediction of the modulus of a discontinuous composite structure. The model is based on the assumptions that only the matrix sustains the axial load and transmits stress to the fiber through shear stress and that all fibers are well dispersed in the matrix.[35] The Halpin-Tsai model equations express the longitudinal and transverse engineering moduli in the following form:

$$E_o = E_m\left[\frac{1+\xi\eta f}{1-\eta f}\right] \tag{6.6}$$

$$\eta = \frac{E_f / E_m - 1}{E_f / E_m + \xi} \tag{6.7}$$

where, E_o is the predicted composite modulus; E_m is the matrix modulus; E_f is the fibrous inclusions modulus (450 GPa for SiCW[36]); f is the fiber volume fraction; η fiber-to-load transfer parameter for the Halpin-Tsai equation; and ξ is the shear coefficient (~ two times the aspect ratio of a fiber for the longitudinal, fiber direction modulus; and 2 for the

transversal, perpendicular to fiber direction, modulus). The average aspect ratio for the whiskers used in this research is approximately 10. This equation, therefore, predicts the longitudinal modulus of our composite material with aligned whiskers to be 2.4 GPa, while the result from our experimentation is 2.2 GPa. The calculated theoretical and experimental results are in a good agreement. We associate the slightly lower values for the experimental modulus with non-ideal (24^o instead of the ideal 0^o) orientation of MagSiCWs in the material. The modulus for randomly oriented fibers can be estimated using equation 6.8:[37-38]

$$E_o = \frac{3}{8}E_l + \frac{5}{8}E_t \qquad (6.8)$$

where E_l and E_t are the longitudinal and transverse moduli, respectively. We have already estimated the longitudinal modulus, and the transverse modulus was calculated by equations (6.6) and (6.7) assuming ξ equals 2.[33] Next, using Equation 6.8, the modulus for the composite with randomly distributed whiskers was found to be approximately 1.9 GPa in excellent agreement with the DMA results. In general, the comparison between the calculated and experimental values for oriented and non-oriented epoxy/MagSiCW composites clearly indicated that efficient matrix–whisker stress transfer existed in the nanocomposites.

The temperature dependence of tan δ (E''/E') is shown in Figure 11b. E'' is the loss modulus determined in the DMA experiment. The position of the tan δ peak indicates the glass transition temperature of the material when variable stress is applied to the sample. As in DSC measurements, the lowest T_g value (67^{o}C) was observed for the epoxy

composite with non-oriented MagSiCWs, which is significantly lower than that of the neat epoxy material (T_g = 77°C). However, the T_g value measured by DMA for the nanocomposite with oriented MagSiCWs (83°C) is higher indicating that mobility of polymer chains is restrained in the whisker direction in comparison with the bulk epoxy. We also note that the width of the tan δ peak is significantly greater for the composites with asymmetry into the higher temperature region. The width of the transition is related qualitatively to the homogeneity of the epoxy network (variation in cross-linked density) and, therefore, to the variation in mobility of polymer chains.[39-41] Therefore, as was already determined from the DSC measurements, zones with noticeable differences in network density are present in the nanocomposites. The asymmetry of the dependence of the tan δ peak on temperature corroborates formation of interphase domains possessing chains with mobility changed by the presence of the whiskers.

Noticeable differences in the height of the tan δ peaks are observed for the materials as well. The peak height is a measure of interfacial stress transfer in composite materials, where smaller values point toward a higher degree of elastic response to the stress applied.[39] The oriented composite has the lowest tan δ peak, and the non-oriented composites have the highest tan δ peak. This behavior of the oriented nanocomposite materials is indicative of lower loss (more elastic) material, if compared with the neat epoxy and non-oriented composite. In general, DMA results confirm our suggestion that an extended interphase with variable properties is formed in the nanocomposites and that the interphase formation is affected by the orientation of the MagSiCWs in a positive way leading to a nanocomposite with superior mechanical properties.

Magnetic Characterization

Magnetization curves were measured for composites consisting of non-oriented and magnetically oriented MagSiCWs with a pure epoxy sample as a control. The magnetic response of a pure epoxy sample was measured to be negligibly small, while the nanocomposites were observed to be significantly magnetic with superparamagnetic characteristics. To characterize the magnetic anisotropy, two magnetic measurements were performed for each sample: one measurement with the in-plane magnetic field oriented along one side of the sample and the other measurement with the in-plane magnetic field oriented along the other side of the sample. Thus, for the oriented nanocomposites, the measurements were conducted along the direction of orientation of the nanorods ($m_{p||}$, $M_{g||}$) and perpendicularly to the direction of orientation of the nanorods, ($m_{p\perp}$, $M_{g\perp}$). Results of the magnetic measurements are presented in Table 6.1.

Table. 6.1: Magnetic properties of the nanocomposites.

Type of sample and measurements	Magnetic moment of each particle, m_p [Am^2]	Mass magnetization, M_g [Am^2/g]
Non-oriented average – direction 1	$1.92*10^{-19}$	$3.78*10^{-4}$
Non-oriented average – direction 2	$1.96*10^{-19}$	$3.68*10^{-4}$
Oriented average – parallel	$1.92*10^{-19}$	$4.84*10^{-4}$
Oriented average – perpendicular	$1.83*10^{-19}$	$4.86*10^{-4}$

Typical plots of the magnetization curves for non-oriented and oriented samples are presented in Figure 6.12, however, the graphical representations do not allow one to distinguish the results.

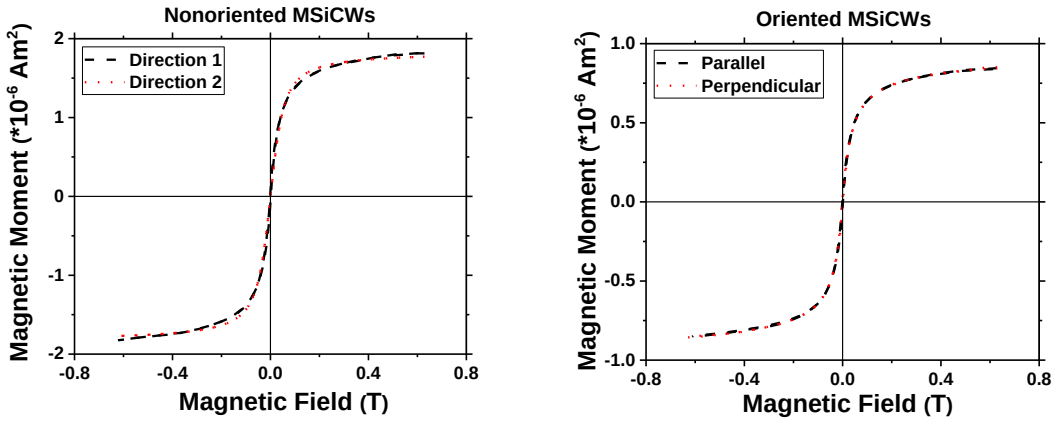

Figure 6.12: Magnetometer measurements of the oriented composite materials where the Mag-SiCWs were oriented (left) parallel and (right) perpendicular to the magnetic field.

For quantitative evaluation of these differences, one can introduce the order parameters as $\Delta_{m_p} = \left|m_{p\|} - m_{p\perp}\right| / m_{p\|}$ and $\Delta_{M_g} = \left|M_{g\|} - M_{g\perp}\right| / M_{g\|}$. These parameters provide a metric for the nanorod orientation in the sample. As a reference, an estimation of magnetic anisotropy was made for non- oriented samples. Following the same procedure, we obtained Δ_{m_p} = 0.02 and Δ_{M_g} = 0.03. These values define the accuracy of our measurements of anisotropy. For oriented samples, the order parameters were measured as Δ_{m_p} = 0.05±0.02 and Δ_{M_g} = 0.0±0.03. This suggests that the nanorod orientation does not affect the magnetic properties of the composite at high fields when the magnetic moments are co-aligned with the field, but does demonstrate an anisotropy at the lower fields when the magnetic moments are not completely aligned with the field. These weak fields

correspond to the Langevin dependence shown in Figure 6.12 at the fields roughly below 0.4 Tesla.

6.3.5: Composite Microstructure Analysis

The composite microstructure is comprised of the distribution of the particulate orientation, particulate dispersity, and the cross-linking density of the epoxy matrix. These were investigated by variable pressure SEM and swelling experiments. The analysis was important to draw general conclusions from the structure-to-properties relationship.

MagSiCW/Epoxy Composite Microstructure Analysis

The composite microstructure was analyzed from images like the one presented in Figure 6.8. The number of agglomerates and whiskers' dispersity was measured. The summary of the composite microstructural analysis is reported in Table 6.2. The composite materials' distribution of MagSiCW does not significantly varies between non-oriented and oriented samples. However, there is a significantly more aggregates in the oriented samples. Additionally, the oriented composites have a higher aspect ratio of the aggregates. We suppose that the aggregation is caused by additional application of a magnetic field. The MagSiCWs are forced together by the whisker-to-whisker magnetic interactions creating a greater aspect ratio for the composite aggregates.

Table 6.2: The agglomeration and dispersity of the composite fillers within the cured epoxy matrix.

Summary	Distance between fillers (μm)	# of aggregates/mm	Length of aggregates (μm)	Width of aggregates (μm)
Non-oriented	10.9 ± 5.9	80 ± 3	10.6 ± 3.6	5.1 ± 3.6
Oriented	9.4 ± 4.8	171 ± 44	10.9 ± 3.4	3.6 ± 3.4

Next, the orientation of the particulates was measured and recorded for each composite. The level of orientation was measured from longitudinally broken composite samples. The whiskers were identified by hand drawing a line down the center of the whiskers from end to end. Then, the angle of orientation was taken between the net director and the line using Gwyddion software. Approximately 200–300 randomly selected whiskers were measured for each image, with two to four SEM images from two to three samples. The orientation of the non-oriented and oriented composite materials is shown in Figure 6.13.

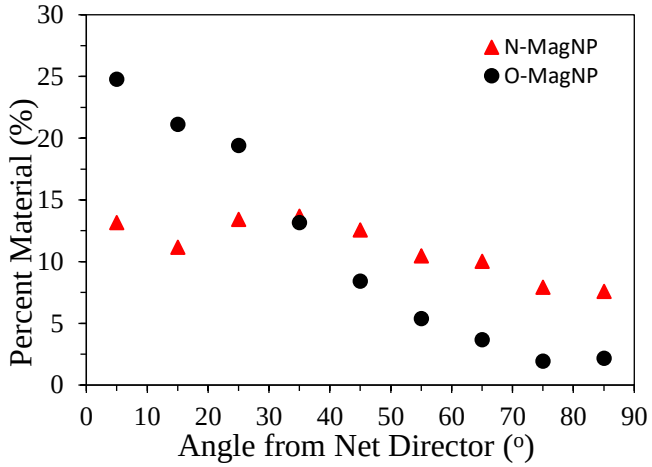

Figure 6.13: Histogram of the fillers' orientation from the net director within each of the composites.

It can be pointed that the orientation of the whiskers without the application of the magnetic field was practically random. However, the oriented composite shows a shift in the alignment with ~64 % of the filler oriented within 30 ° of the net director.

Analysis of the Relative Cross-Linking Density in Epoxy and Composite Materials

First, the composite materials' cross-linking density was calculated from the storage modulus at 40 °C above the Tg (E_{Mc}) using Equation 6.2. The modulus was equal

3.5 MPa, 1.5 MPa, and 5.4 MPa for neat epoxy, epoxy with non-oriented whiskers and epoxy with oriented whiskers, respectively. These cross-linking densities from DMA results were compared to the relative cross-linking density extrapolated from the swelling experimentation. The swelling results for the composite materials are presented in Table 6.3.

Table 6.3: Results of swelling experiments.

Sample	Neat Epoxy	MagSiCW/Epoxy - No Orientation	MagSiCW/Epoxy - Orientation
m_d (g)	0.016±0.003	0.015±0.006	0.011±0.001
$m_{eq} - m_d$ (g)	0.006±0.001	0.009±0.002	0.004±0.001

These parameters were plugged into Equation 6.4 to obtain the volume fraction of polymer in the sample to then used in Equation 6.3 to calculate the relative cross-linking density of the samples. For each one of these samples, three to four measurements were averaged to estimate the standard deviation.

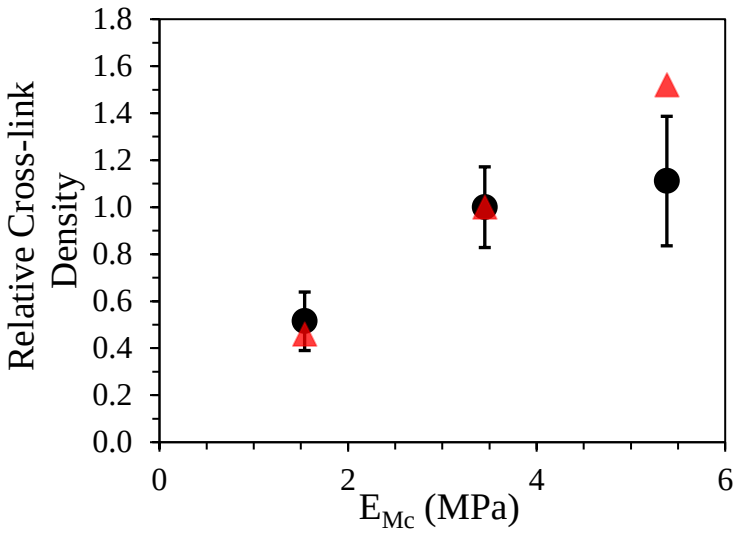

Figure 6.14: The results from the calculated relative cross-linking using DMA measurements (▲) and swelling experimentation (●) vs E_{Mc}, storage modulus above 40°C. (The samples are signified from left to right as the non-oriented MagSiCW/epoxy composite, neat epoxy, and oriented MagSiCW/epoxy composite).

It was found that the composite samples with oriented MagSiCWs show a dramatic increase in cross-linking density in comparison with the non-oriented composite (Figure 6.14). This result supports formation of extended interphase domain B in the oriented composite possessing higher level of crosslinking. On the other hand, E_{Mc} results (Equation 6.2) do not fit the experimental results of the solvent swelling for the oriented composite. This suggests that the orientation of the fillers is absorbing more stress, creating a higher elastic modulus, although the oriented composite and the neat epoxy share approximately the same cross-linking density. Hence, the E_{Mc} of the oriented composite was 1.6 times larger than the neat epoxy and 3.5 times larger than the non-oriented composite. We associate the decrease in T_g for the non-oriented composite with formation of interphase with lower T_g inside layer of MagNP and in close proximity to the whiskers' surface. It appeared that the orientation of the whiskers to a certain extend alleviate this problem.

6.4: Conclusions

The following conclusions can be determined as a result of our study reported in Chapter 6:

- The MagSiCWs change the chemical pathway of the epoxy reaction, accelerating the polymerization reaction that prefers to consume the anhydride hardener vs DGEBA epoxy groups.
- The grafting of the epoxy polymer to the surface of the MagSiCWs is observed.
- The best orientation of whiskers in the epoxy matrix composite is achieved using the 'pulsed' application of a magnetic field.

- The oriented and non-oriented MagSiCW composites had a greater storage modulus than the neat epoxy. However, the glass transition temperature determined from DMA was only improved by the whisker orientation.
- The thermal properties revealed that the composite with orientation yielded no enthalpic relaxation along with a ΔT_g that is 3x the length of the other composite materials.
- The composite materials' magnetic properties on the macro-scale were considered super-paramagnetic. Additionally, when a field was applied perpendicular and parallel to the orientation of the composite material, these composite properties were the same.
- Microstructural analysis showed that the magnetically oriented composite had a higher degree of packing and more agglomerates. However, the agglomerates did have a higher aspect ratio than the non-oriented composites.
- Microstructural analysis of the amorphous polymer structure showed that the oriented composites had a much greater cross-linking density than the non-oriented composites.

6.5: References

1. Putz, K. W.; Palmeri, M. J.; Cohn, R. B.; Andrews, R.; Brinson, L. C., Effect of cross-link density on interphase creation in polymer nanocomposites. *Macromolecules* **2008,** *41* (18), 6752-6756.

2. Cheng, X.; Putz, K. W.; Wood, C. D.; Brinson, L. C., Characterization of local elastic modulus in confined polymer films via AFM indentation. *Macromol Rapid Comm* **2015,** *36* (4), 391-397.

3. Kolar, F.; Svitilova, J., Kinetics and mechanism of curing epoxy/anhydride systems. *Acta Geodyn Geomater* **2007,** *4* (3), 85-92.

4. Chu, F. D. J.; Robertson, R. E., The effect of adherends on the curing of an epoxy adhesive. *J Adhesion* **1995,** *52* (1-4), 149-166.

5. Jung, J. C.; Lee, S. K.; Lee, K. S.; Choi, K. Y., Chain-length effect of alkenyl succinic anhydride on thermal and mechanical properties of the cured epoxy resins. *Angewandte Makromolekulare Chemie* **1991,** *185*, 129-136.

6. Park, W. H.; Lee, J. K., A study on isothermal cure behavior of an epoxy-rich/anhydride system by differential scanning calorimetry. *Journal of Applied Polymer Science* **1998,** *67* (6), 1101-1108.

7. Harsch, M.; Karger-Kocsis, J.; Holst, M., Influence of fillers and additives on the cure kinetics of an epoxy/anhydride resin. *European Polymer Journal* **2007,** *43* (4), 1168-1178.

8. Murayama, T., *Dynamic mechanical analysis of polymeric mateiral*. Elsevier Scientific Publishing Group: Amsterdam, 1978.

9. Chen, J. S.; Ober, C. K.; Poliks, M. D.; Zhang, Y. M.; Wiesner, U.; Cohen, C., Controlled degradation of epoxy networks: analysis of crosslink density and glass transition temperature changes in thermally reworkable thermosets. *Polymer* **2004,** *45* (6), 1939-1950.

10. Kennedy, J. M.; Banerjee, A.; Cano, R. J., Characterization of interfacial bond strength by dynamic analysis. *J Compos Mater* **1990,** *26* (6), 869-882.

11. Wu, H. F.; Gu, W.; Lu, G. Q.; Kampe, S. L., Non-destructive characterization of fibre-matrix adhesion in composites by vibration damping. *Journal of Materials Science* **1997,** *32* (7), 1795-1798.

12. Donth, E., Characteristic length of the glass transition. *J Polym Sci Part B Polym Phys* **1996,** *34*, 2881-2892.

13. Lu, H. B.; Nutt, S., Enthalpy relaxation of layered silicate-epoxy nanocomposites. *Macromol Chem Phys* **2003,** *204* (15), 1832-1841.

14. Lu, H. B.; Nutt, S., Restricted relaxation in polymer nanocomposites near the glass transition. *Macromolecules* **2003,** *36* (11), 4010-4016.

15. Putz, K. W.; Mitchell, C. A.; Krishnamoorti, R.; Green, P. F., Elastic modulus of single-walled carbon nanotube/poly(methyl methacrylate) nanocomposites. *J Polym Sci Pol Phys* **2004,** *42* (12), 2286-2293.

16. Ramanathan, T.; Liu, H.; Brinson, L. C., Functionalized SWNT/polymer nanocomposites for dramatic property improvement. *J Polym Sci Pol Phys* **2005,** *43* (17), 2269-2279.

17. Abenojara, J.; Encinas, N.; Del Real, J. C.; Martínez, M. A., Polymerization kinetics of boron carbide/epoxy composites. *Thermochim Acta* **2014,** *575*, 144-150.

18. Jackson, P. L.; Huglin, M. B.; Cervenka, A., Use of inverse gas chromatography to quantify interactions in anhydride cured epoxy resins. *Polym Int* **1994,** *35* (2), 135-143.

19. Zdyrko, B.; Klep, V.; Luzinov, I., Synthesis and surface morphology of high-density poly(ethylene glycol) grafted layers. *Langmuir* **2003,** *19* (24), 10179-10187.

20. Montserrat, S., Physical aging studies in epoxy resins. I. Kinetics of the enthalpy relaxation process in a fully cured epoxy resin. *J Polym Sci Pol Phys* **1994,** *32* (3), 509-522.

21. Brown, H. R.; Char, K.; Deline, V. R., Enthalpy-driven swelling of a polymer brush. *Macromolecules* **1990,** *23* (13), 3383-3385.

22. Rittigstein, P.; Priestley, R. D.; Broadbelt, L. J.; Torkelson, J. M., Model polymer nanocomposites provide an understanding of confinement effects in real nanocomposites. *Nat. Mater.* **2007,** *6* (4), 278-82.

23. Bansal, A.; Yang, H.; Li, C.; Cho, K.; Benicewicz, B. C.; Kumar, S. K.; Schadler, L. S., Quantitative equivalence between polymer nanocomposites and thin polymer films. *Nat Mater* **2005,** *4* (9), 693-8.

24. Hussain, F.; Hojjati, M.; Okamoto, M.; Gorga, R. E., Review article: Polymer-matrix nanocomposites, processing, manufacturing, and application: An overview. *J Compos Mater* **2006,** *40* (17), 1511-1575.

25. Zhou, Y. X.; Hosur, M.; Jeelani, S.; Mallick, P. K., Fabrication and characterization of carbon fiber reinforced clay/epoxy composite. *Journal of Materials Science* **2012,** *47* (12), 5002-5012.

26. Al-Saleh, M. H.; Sundararaj, U., Review of the mechanical properties of carbon nanofiber/polymer composites. *Compos Part A Appl S* **2011,** *42* (12), 2126-2142.

27. Putz, K.; Krishnamoorti, R.; Green, P. F., The role of interfacial interactions in the dynamic mechanical response of functionalized SWNT-PS nanocomposites. *Polymer* **2007,** *48* (12), 3540-3545.

28. Steffan, C. E.; Liu, H.; Winter, R. M.; Cabibil, H.; Lozano, J.; Celio, H.; White, J. M.; Houston, J. E., The Relationship Between Nanomechanical and Chemical Properties in Polymer Composites. In *Proceedings of the Society of Experimental Mechanics IX International Congress on Experimental Mechanics*, 2000; pp 920-923.

29. Diez-Pascual, A. M.; Gomez-Fatou, M. A.; Ania, F.; Flores, A., Nanoindentation assessment of the interphase in carbon nanotube-based hierarchical composites. *J Phys Chem C* **2012,** *116* (45), 24193-24200.

30. Yedla, S. B.; Kalukanimuttam, M.; Winter, R. M.; Khanna, S. K., Effect of shape of the tip in determining interphase properties in fiber reinforced plastic composites using nanoindentation. *J Eng Mater-T Asme* **2008,** *130* (4), 15.

31. Williams, J. G.; Li, F. P.; Miskioglu, I., Characterization of the interphase in epoxy/aluminum bonds using atomic force microscopy and a nanoindenter. *J Adhes Sci Technol* **2005,** *19* (3-5), 257-277.

32. Downing, T. D.; Kumar, R.; Cross, W. M.; Kjerengtroen, L.; Kellar, J. J., Determining the interphase thickness and properties in polymer matrix composites using phase imaging atomic force microscopy and nanoindentation. *J Adhes Sci Technol* **2000,** *14* (14), 1801-1812.

33. Fornes, T. D.; Paul, D. R., Modeling properties of nylon 6/clay nanocomposites using composite theories. *Polymer* **2003,** *44* (17), 4993-5013.

34. Libanori, R.; Erb, R. M.; Studart, A. R., Mechanics of platelet-reinforced composites assembled using mechanical and magnetic stimuli. *ACS Appl Mater Interfaces* **2013,** *5* (21), 10794-805.

35. Halpin, J. C.; Kardos, J. L., The Halpin-Tsai equations : A review. *Polymer Engineering and Science* **1976,** *16* (5), 344-352.

36. Compton, B. G.; Lewis, J. A., 3D-printing of lightweight cellular composites. *Adv Mater* **2014,** *26* (34), 5930-5.

37. Tsai, S. W.; Pagano, N. J., Invariant properties of composite materials In *Composite materials workshop*, Tsai S. W.; Halpin, J. C.; Pagano, N. J., Eds. Technomic Publishing Company: St. Louis, 1968; p 233.

38. Nielsen, L. E., *Mechanical properties of polymers and composites. Vol. 2*. Dekker: New York, 1974; p 462.

39. Vennerberg, D.; Rueger, Z.; Kessler, M. R., Effect of silane structure on the properties of silanized multiwalled carbon nanotube-epoxy nanocomposites. *Polymer* **2014,** *55* (7), 1854-1865.

40. Miyagawa, H.; Misra, M.; Drzal, L. T.; Mohanty, A., Biobased epoxy/layered silicate nanocomposites: Thermophysical properties and fracture behavior evaluation. *J Polym Environ* **2005,** *13* (2), 87-96.

41. Miyagawa, H.; Rich, M. J.; Drzal, L. T., Amine-cured epoxy/clay nanocomposites. I. Processing and chemical characterization. *Journal of Polymer Science Part B-Polymer Physics* **2004,** *42* (23), 4384-4390.

CHAPTER SEVEN

THE EFFECT OF INTERFACIAL MODIFICATION ON SICW/EPOXY COMPOSITE FORMATION AND PROPERTIES

7.1: Introduction

It is well established that nanoscale fillers can improve mechanical, electrical, and optical properties of polymer composite materials[1-5]. To a significant extent, such improvements are caused by interactions at the interface between fillers and a matrix (nano-confinement effects)[6-8]. Therefore, in this work, the interfacial effects within the SiCWs/epoxy composites were investigated further by modifying SiCWs' surface with different materials to determine the influence of surface modification on the composite's properties.

In general, the interfacial interactions within composites have been considered from a chemical and structural points of view[9]. Thus, depending on the application, a variety of surface modifications can be employed to improve the matrix/filler interactions. For example, carbon fibers are processed with nitric acid to create favorable surface chemistry and increased roughness for improvement of epoxy composites[10]. However, it is still not entirely understood how surface modification can affect the material's properties and structure of a nanocomposite.

In this chapter of the dissertation, we examine the effect of whisker surface modification on the epoxy composite system. As in, SiCWs have been used in nanoparticulate-enhanced polymer coatings[11], multi-component ceramic matrix composites[12] and epoxy carbon fiber composites[13-15] for reinforcement, abrasion,

resistance and thermal conductivity. However, published works have not paid significant attention to interfacial interactions in SiCWs-based composites. To this end, this part of the study focuses on the SiCW nanoparticulate surface modification targeting thermo-mechanical reinforcement of epoxy composites. For this specific purpose, we examined the formation and properties of the composites as a function of the interaction at the epoxy/SiCW interfaces. A schematic of surface modification for the SiCWs is presented in Figure 7.1. Specifically, the following surface modifications were conducted: “a” is the inner darkest region representing the thermally cleaned SiCWs (SiCW-OH); “a–b” is the black solid line representing the epoxy silane modification (SiCW-Ep); “b” is the greyed middle area representing the grafted P2VP layer (SiCW-P2VP); “b–c” is the black dashed line representing the PAA to P2VP complexation; and “c” is the grey outer-layer of the whiskers representing the attached PAA (SiCW-PAA).

Figure 7.1: Layout of the silicon carbide whisker after three consecutive surface modifications: (a) is bare SiCWs; (a-b border) - epoxy silane modification; (b) - grafted P2VP; (c) - PAA layer.

7.2: Experimental

7.2.1: Surface Modification

To clean the surface and create the surface hydroxyl groups, the SiCWs (SiCW-OH) were heat treated at 400 ^{o}C for 1 hour in an air environment. Next, 1 gram of the cleaned SiCWs were mixed with DI water and shaken for 24 hours. To separate the agglomerates from the solution, the water suspension was left to settle for 20 s and then decanted. The decanted portion of SiCWs was dispersed in methanol at a 2 wt. %. Then, the SiCW suspension in methanol was cleaned three times by repetitive sequential centrifugation, decanting and redispersing in methanol. The final cleaned whiskers had an average length of 4700 nm and a diameter of 400 nm, as was determined by SEM imaging.

For the surface modification, we used methodology reported elsewhere[16-20]. To modify the surface of SiCWs with the epoxy-silane (SiCW-EP), the SiCWs were mixed into a 2.5 wt. % solution of epoxy silane in toluene and shaken for 24 hours. Next, the SiCWs modified with epoxy silane were cleaned in fresh toluene and methanol by several centrifugation and redispersion cycles.

To obtain SiCWs modified with P2VP (SiCW-P2VP), the SiCW-EP was dispersed in MEK and added dropwise to a 5 wt. % of P2VP solution in MEK. This solution was rotary evaporated and placed inside a vacuum oven at 120 ^{o}C for 24 hours. To remove non-grafted polymer, the SiCW-P2VPs were cleaned 3 times with fresh MEK using centrifugation and redispersion cycle.

Finally, to deposit the PAA layer by complexation[21] on the SiCWs (SiCW-PAA), the SiCW-P2VP were dispersed into methanol at 1 wt. % and added dropwise (at 1:1 volume ratio) to 2 wt. % PAA solution in methanol. This mixture was shaken for 24 hours. The SiCW-PAA was cleaned in fresh methanol 3 times using redispersion, centrifugation cycle.

7.2.2: Composite Fabrication

As reported in the previous chapter, the SiCWs were mixed with the epoxy resin and then the hardener and catalyst were added. The epoxy, hardener, and catalyst volume ratio was 1:1.37:0.07. To prepare composite material, the epoxy matrix/whiskers mixture was casted into Teflon mold at room temperature. The mixture was cured at room temperature for 48 hours, and then at 75 ^{o}C for 24 hours. According to DSC results, these time-temperature conditions were sufficient to fully cure the polymer matrix. The volume fraction of the whiskers in the matrix was approximately 3 %.

7.2.3: Epoxy Curing Reaction

The activation energy (E_a) and degree of reaction (α) for the curing were determined using DSC to gauge the effect of temperature on the reaction and to monitor the real-time progression of the reaction. The activation energy of the pure epoxy and composites was determined using the Kissinger method[22]. Namely, the peak temperatures (T_p), defined by the exothermic peak of the epoxy curing reaction were obtained by heating the epoxy resin at a rate of 10, 30, and 40 ^{o}C/min. The resultant T_ps were plotted against the natural logarithm of the heating rate divided by T_p^2. E_a was obtained from the

slope of the dependence. The α at specific time point of 3, 6, 12, 24, and 48 hours was determined using Equation 6.1

7.2.4: Thermo-Mechanical Characterization using DMA

Tensile DMA testing was run at 2 ^{o}C/min from -20 ^{o}C to 150 ^{o}C using frequencies of 1, 2, and 5 Hz and applying 5 μm amplitude of oscillation. Each of the samples was approximately the same dimensions with a length of 8.00 mm, a width of 5.00 mm, and a thickness of 0.34 mm.

7.2.5: Thermal Characterization using DSC

The DSC samples were prepared from the mold casted and thermally cured epoxy and composite samples. The samples of 5–10 mg were sealed into an aluminum pan with an aluminum lid. The first DSC run was at 15 ^{o}C/min from -10 ^{o}C to 150 ^{o}C. Then, the samples were cooled at 15 ^{o}C/min to -10 ^{o}C and run for a second time at 15 ^{o}C/min from -10 ^{o}C to 150 ^{o}C.

7.2.6: Composite Microstructure Analysis by SEM

SEM was used to evaluate the microstructure of the composite materials. The samples were dipped into liquid nitrogen and broken in the longitudinal direction. The samples were then attached to an aluminum SEM puck with a carbon tape to have the fractured edge facing the SEM detector. The images were analyzed using Gwyddion software to determine the distribution of the SiCWs in the epoxy matrix. The distribution was quantified by randomly selecting 25–35 whiskers and measuring the distance to the next closest, typically 8–13,whiskers. The distance to the next closest identifiable whiskers was measured between the centers of the whiskers. Additionally, whisker

agglomerates within the composite matrix were counted, their size and concentration were measured. The length and width of the aggregates were measured by drawing a box around them. This was done for two to three images and two different samples of the materials.

7.2.7: Determination of the Composites' Cross-Linking Density for the Epoxy Matrix

The density of cross-links was determined from the storage modulus value above T_g and swelling results for the thermoset[23]. The relevant methodologies are described in Chapter 6.

7.3: Results and Discussion

7.3.1: Curing of Epoxy Resin in the Presence of Modified SiCWs

Studies of Epoxy Curing using DSC

The extent of epoxy polymerization in the presence of modified SiCWs versus time of the polymerization at room temperature is shown in Figure 7.2a. Using the on the

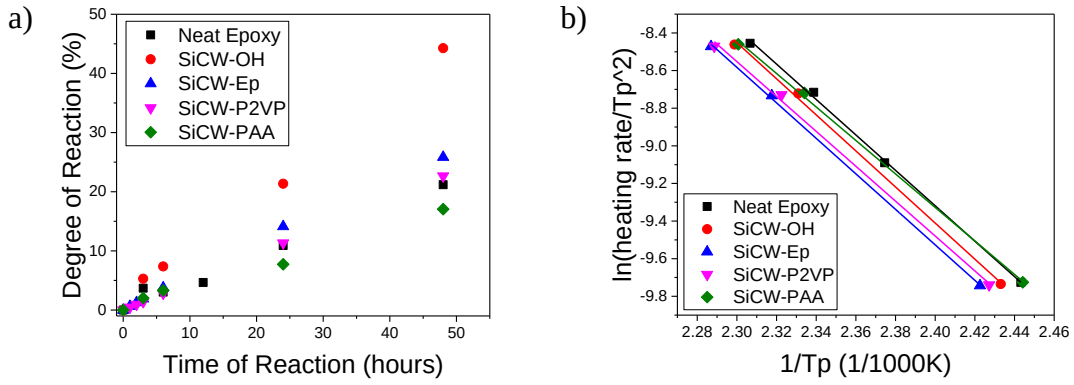

Figure 7.2: (a) the degree of curing versus the time of reaction at room temperature and (b) the Kissenger plot.

Kissinger model based Arrhenius equation (Equation 6.5), the E_a was determined using the dependencies shown in Figure 7.2b. The degree of curing after 48 hours of the reaction and E_a values are reported in Table 7.1.

Table 7.1: Parameters of epoxy curing calculated using DSC data.

Sample	E_a (J/mol)	α_{48hrs} (%)
neat epoxy	78.20	21.2
SiCW-OH	79.72	44.3
SiCW-Ep	78.45	25.0
SiCW-P2VP	77.90	22.7
SiCW-PAA	74.01	17.1

The results show no significant variations in the activation energy, except for the SiCW-PAA modification, which has a 4.2 J/mol difference from the neat epoxy (Table 7.1). The value for SiCW-PAAs is very close to the E_a for MagSiCWs (72.5 J/mol). This finding indicated that the chemical events occurring during the epoxy curing are similar for SiCW-PAAs and MagSiCWs. The obtained results revealed that the surface modifications significantly influence the rate of the curing. For instance, the epoxy with SiCW-OH was 44.3% cured after 48 hours of room-temperature curing. This is significantly higher rate than the one for the neat epoxy and the neat epoxy with SiCW-EP, showing 21.2 % and 25.0 % of curing for the same time of the reaction. However, these results do not reflect the details of chemical aspects of the curing reaction.

Studies of Epoxy Curing using ATR-FTIR

The effect of surface modification on the curing reaction chemical pathway was studied using ATR-FTIR. As the epoxy and anhydride consumption were the two main chemicals participating in the curing process, their functional groups were followed with IR

spectroscopy. Figure 7.3a shows how the concentration of epoxy functional groups (913 cm^{-1} peak) decreases with the time of the curing reaction. Figure 7.3b illustrates how the concentration of anhydride groups (1780 cm^{-1} peak) decreases with the reaction time.

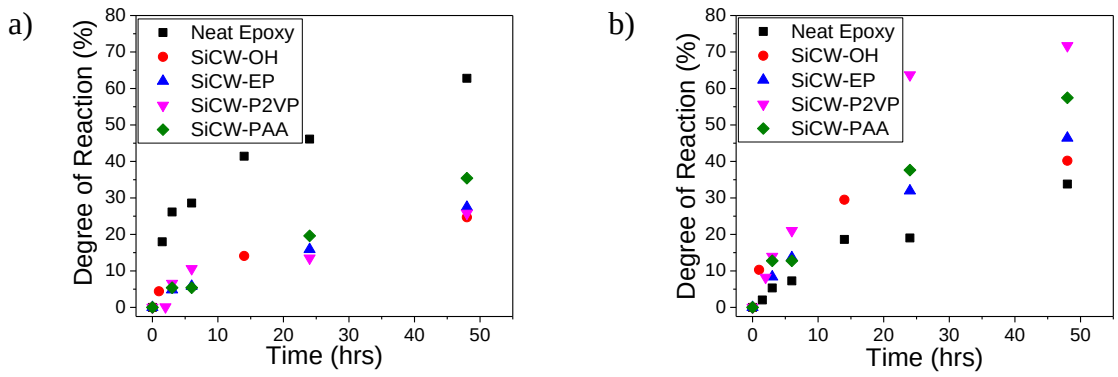

Figure 7.3: The degree or the reaction calculated based on consumption of: (a) epoxy groups, (b) anhydride groups.

Table 7.2 summarizes the data obtained from ATR-FTIR experiments after 48 hours of curing. One can see that during the curing of the neat epoxy, the rate of epoxy groups consumption is higher than the rate in the presence of SiCWs, including the MagSiCWs reported in Chapter 6. Among SiCWs the highest epoxy consumption rate is found for

Table 7.2: Consumption of epoxy and anhydride functional groups after 48 hours of curing at room temperature.

Sample	Epoxy Consumption (%)	Anhydride Consumption (%)
neat Epoxy	62.8	33.8
SiCW-OH	24.7	40.2
SiCW-EP	27.5	46.4
SiCW-P2VP	25.8	71.2
SiCW-PAA	35.4	54.4

SiCWs covered with PAA layer. We associate the observed result with high rate of epoxy-carboxylic group reaction. The anhydride groups are consumed at much different rates varying from 33.8–71.2 % per 48 hours for SiCWs with different surface modifications. The rate is the lowest for the unmodified epoxy.

The anhydride consumption showed unique signatures for different types of SiCWs. It can be observed that the SiCW-P2VP acted as a catalyst causing very fast consumption (71.4 %) of the anhydride groups. It is known that nitrogen-containing substances catalyze the reaction of anhydride with epoxy[24-25]. Hence, the basic nitrogen of the P2VP could have catalyzed the opening of the anhydride. At the same time, the epoxy consumption is not dramatically affected by the presence of SiCW-P2VP.

The ATR-FITR results were used to reveal the difference in chemical pathway of epoxy curing in the presence of SiCWs in comparison to the neat epoxy. This is shown in Figure 7.4 by plotting the degree of anhydride vs. the degree of epoxy consumed in the

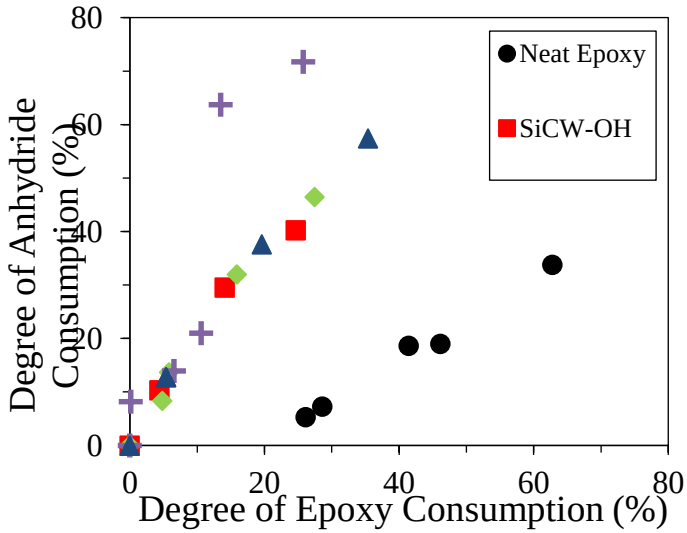

Figure 7.4: ATR-FTIR results for the epoxy curing reaction: (a) degree of the epoxy group consumption monitored by the 913 cm^{-1} peak, (b) degree of the anhydride group consumption monitored by the 1780 cm^{-1} peak.

curing reaction. Most of all, the epoxy polymerization in the presence of SiCW-P2VP was the most different from the neat epoxy and other composite materials, showing the rapid consumption of the anhydride with much less consumption of the epoxy groups. The other whiskers show nearly the same chemical pathway, within 2 % of each other at any given point. However, the overall rate of the curing was the highest for SiCWs-PAA and the slowest for SiCWs-OH. These results also different from the ones for MagSiCW epoxy composites. 48 hours into the reaction, the MagSiCWs epoxy composite had consumed ~75 % of the anhydride groups and ~50 % of the epoxy groups (Figure 6.6). This outpaces the consumption rate for the rest of the composite material. To conclude, the chemical composition of SiCWs definitely plays a significant role in the epoxy polymerization. It is suggested that to understand the processes involved additional studies are needed in the future.

7.3.2: Properties of the SiCW/Epoxy Composites

Thermo-Mechanical Characterization

The cured epoxy composite materials were tested employing DSC and DMA to study their thermal and mechanical properties. Figure 7.5 shows the storage modulus (E') dependence on temperature for the neat epoxy and composite materials obtained from the DMA measurements. Table 7.3 summarizes the results of the DMA experiments. It is obvious that the moduli of the composites at room temperature are very close and are approximately 60 % higher than the modulus of the neat epoxy material. On the other hand, the DMA-measured glass transition (T_g), defined by the peak of the loss modulus (E"), is observed to vary by 10 ^oC. The tan δ peak (the highest value of E"/E' ratio)

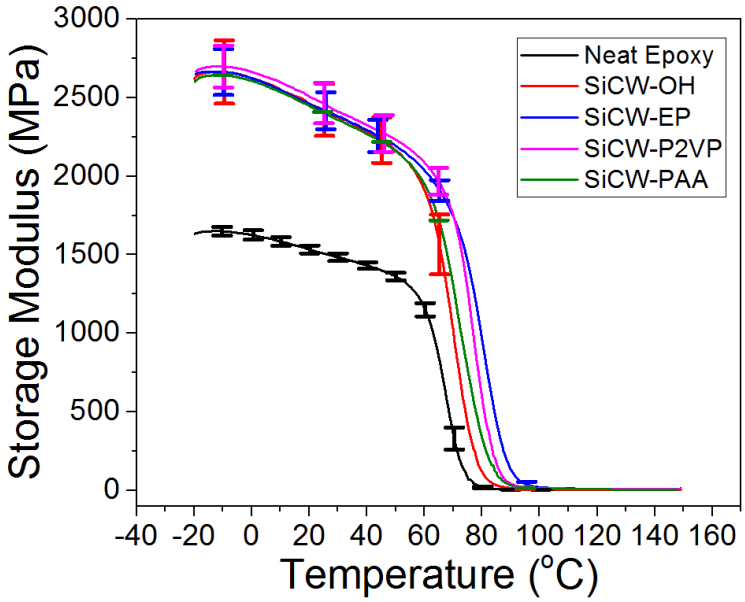

Figure 7.5: The temperature dependence of DMA storage modulus for different composite materials.

relates the mechanical performance to the energy dissipation of the system. In general, our results show that the variation in the surface chemistry of the SiCWs causes measurable changes in the thermomechanical properties of the composites.

Table 7.3: DMA results for the materials studied. (E_{Mc} is the storage modulus at 40 °C above the T_g and T is temperature).

Sample	E' @ RT (MPa)	E_{mc} (MPa)	E" max (MPa)	T of E" max (°C)	Tan δ max (E"/E')	T of tan δ max (°C)
neat epoxy	1521	3.5	189	69	2.01	77
SiCW-OH	2407	5.8	305	72	1.39	83
SiCW-Ep	2427	10.7	262	83	1.14	93
SiCW-P2VP	2440	10.5	323	80	1.38	90
SiCW-PAA	2412	7.3	256	76	1.25	87

The significant increase in the storage modulus of the composites indicates efficient shear load transfer from the epoxy matrix to high-modulus SiCWs. The shear

load transfer is possible because of good bonding of the matrix to the whisker's surface. It is necessary to point that all the samples reported in this chapter show improved mechanical properties if compared to the non-oriented and oriented MagSiCW/epoxy composites (Chapter 6). Additionally, the composites showed improvement in T_g values. The T_g was the highest for SiCW-EP and SiCW-P2VP. The lowest T_g was found for the SiCW-OH epoxy composites.

The highlighted material properties show increase in the T_g, denoted by the increase in the peak temperature of the loss modulus. Additionally, the decrease in the intensity of tan δ peak and the increase in the tan δ peak temperature are observed. In general, the change in the surface chemistry of the SiCWs did not dramatically affect the thermo-mechanical properties of the composite materials below T_g. However, variations in E' after T_g are found in the changes of the tan δ and the E_{Mc}. We associate the variation in the properties with the influence of SiCW's surface chemistry on the cross-linking density of the epoxy resin.

Thermal Characterization

DSC measurements were used in conjunction with the DMA results. We carried out two DSC runs for each material studied (Figure 7.6). The DCS curves for the first run (Figure 7.6a) show the presence of "double" T_g and enthalpic relaxations. Table 7.4 summarizes the DSC data. In general, we found that material's behavior in the T_g region is quite complex, and DCS data are not directly related to the thermal transitions determined by DMA. It appeared that the epoxy polymer chains behave differently in the vicinity of the whiskers. Indeed, the composite materials have one T_g near the neat epoxy

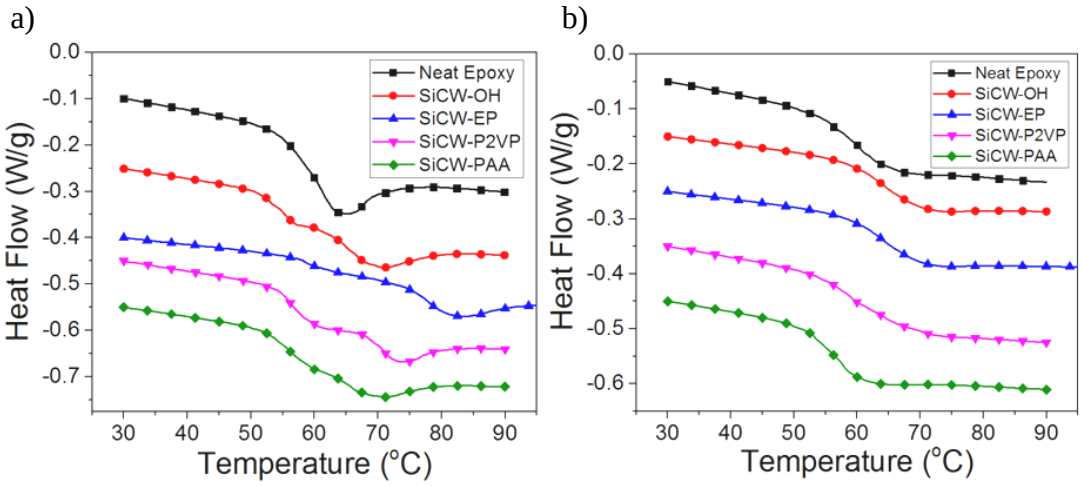

Figure 7.6: The DSC curves for the materials studied: (a) first run and (b) second run.

T_g and then a second T_g at a higher temperature. As T_g is dependent on the free volume, it is hypothesized that the surface groups change the packing of the materials near the surface of the whiskers. These effect can be connected to the various rates and mechanisms of polymerizations near the surface caused by surface functional groups participating in the epoxy curing. As a result, level of epoxy cross-linking is different at different locations of the composite.

Table 7.4: DSC results for the materials studied: T_{g1}-h1 and T_{g2}-h1 is the first and second T_gs from the first run; T_g-h2 is the T_g from the second run; ΔT_g-h2 is the subtraction of the offset from the onset of the T_g from the second run.

Sample	T_{g1}-h1 (°C)	T_{g2}-h1 (°C)	T_g-h2 (°C)	ΔT_g-h2 (°C)
Neat Epoxy	63.3	-	59.5	7.1
SiCW-OH	54.3	65.4	57.6	7.5
SiCW-Ep	58.7	76.3	63.0	10.0
SiCW-P2VP	56.2	71.1	58.7	11.3
SiCW-PAA	55.7	65.9	54.6	6.8

Table 7.4 is used to highlight the main points of the data presented in Figure 7.6. It shows the detected T_gs and the breadth of the transition (ΔT_g). When the epoxy materials are annealed well above T_g via heating in DSC up to 150 °C (first run), the

enthalpic relaxations are not present in the DSC curves of the second run. The materials also have a single T_g after the annealing. The breadth of the T_g transitions are quite similar for all materials and are on the level of 7-10 ^oC. In general, after the annealing we observed randomization of the epoxy network in the materials with T_gs located within ±5 degrees of the T_g of the neat epoxy. It is necessary to point that in DMA experiment the T_gs of composite materials are significantly higher than the one for the neat epoxy. We suggest that DMA experiment is more sensitive to anchoring of the network to the SiCWs surface.

7.3.3: Composite Microstructure Analysis

The microstructure of the composite materials to a significant degree determines properties of the materials . Thus, the filler spatial distribution within the composite was investigated using SEM. The epoxy matrix structure was obtained from the swelling and DMA experiments to estimate the polymers' cross-linking density.

Composite Microstructure Analysis using SEM

The microstructure of the composites was investigated using variable pressure SEM and carrying out swelling experiments. We were interested in determining how the composition of the interface influences the structure of the composite. The spacing between the whiskers and the number of the filler agglomerates per surface (cross-section) area were of the main interest. The images shown in Figure 7.7 are representative images characterizing dispersity and orientation the SiCWs in the composite materials. The orientation of the whiskers in the composites was determined to be random. The values of the filler interspacing and number of agglomerates are reported in Table 7.5.

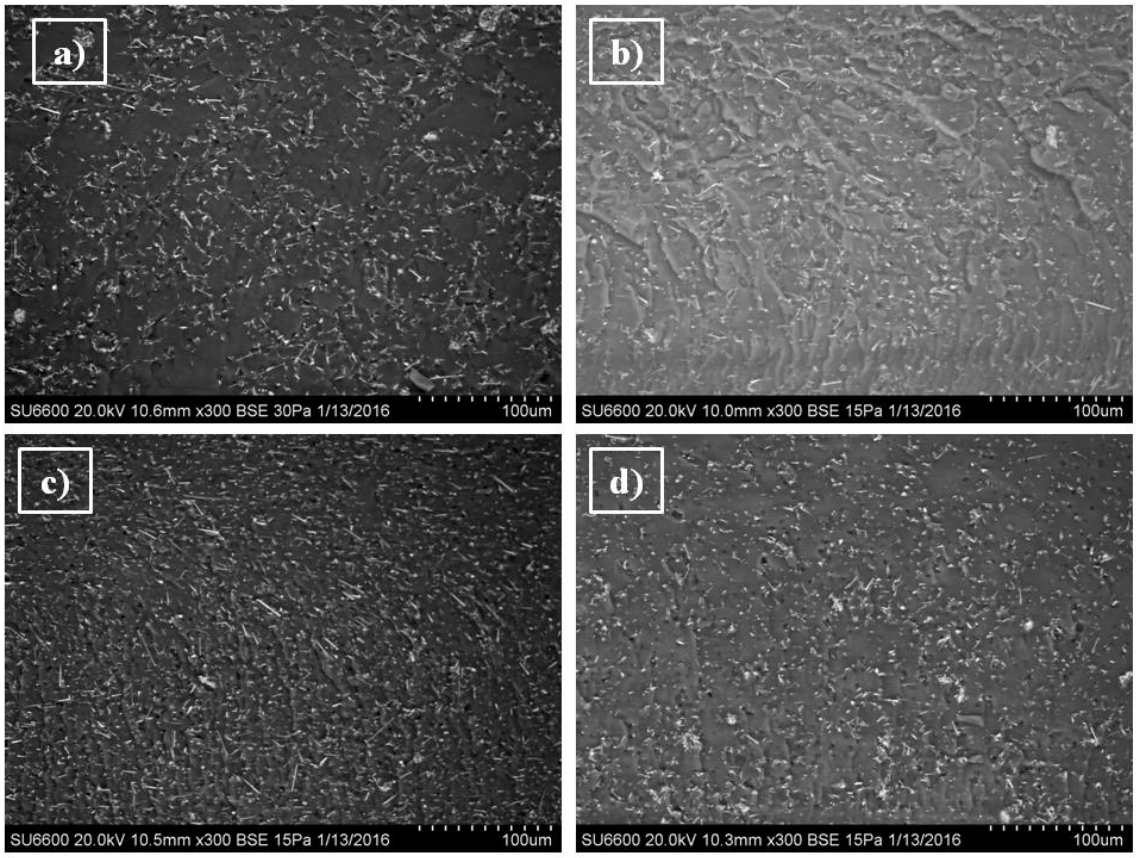

Figure 7.7: SEM images of the cross-section of: (a) SiCW-OH, (b) SiCW-EP, (c) SiCW-P2VP, (d) SiCW-PAA composite materials.

The results indicate that SiCW-P2VP has the highest level of packing along with the lowest amount of agglomerates. The microstructure of other composite materials studied is nearly the same. The whisker-to-whisker distance was run through a standard

Table 7.5: The microstructure data for the composites obtained from SEM images analysis.

Sample	Whisker-whisker distance (μm)	# of agglomerates/mm^2
SiCW-OH	11.5 ± 7.7	199.3 ± 41.8
SiCW-Ep	10.1 ± 19.2	86.1 ± 21.3
SiCW-P2VP	6.7 ± 4.0	34.4 ±11.3
SiCW-PAA	10.8 ± 5.3	115.6 ± 22.6

Student's t-test to determine whether there were any statistical differences between the samples. It was found that SiCW-EP, SiCW-PAA, and SiCW-OH are statistically similar. This suggests that they all share the same level of spacial distribution, which is high in comparison to SiCW-P2VP. We suggest that this is caused by the P2VP polymer layer that was "end grafted" to the surface of the fillers. The grafted polymer chains stretch from the surface, providing steric stabilization of the whiskers and preventing aggregation. At low filler concentration used in this work, the level of SiCWs dispersity does not have a significant effect on the composite properties. However, in future work with composites of higher concentration of the whiskers end-grafted P2VP should be used for the exterior whisker surface modification.

Relative Cross-Linking Density in the Neat Epoxy and Composite Materials

The solvent swelling data and E_{Mc} (storage modulus 40 ^{o}C above the T_g) were used to estimate the cross-linking density of the epoxy matrix in the composite materials. The methodology is the same as presented in Chapter 6. The obtained results from swelling experiments are presented in Table 7.6. Three to five samples were used for each of the data points.

Table 7.6: Results of the swelling experiments.

Sample	Neat Epoxy	SiCW-OH /Epoxy	SiCW-P2VP /Epoxy	SiCW-P2VP /Epoxy	SiCW-P2VP /Epoxy
m_d (g)	0.016±0.003	0.015±0.001	0.017±0.001	0.016±0.003	0.011±0.005
$m_{eq} - m_d$ (g)	0.006±0.001	0.007±0.001	0.006±0.0003	0.006±0.0003	0.005±0.001

Equation 6.4 was used to obtain the volume fraction of the polymer in the sample. Relative cross-linking density was calculated by Equation 6.3 [23]. In addition,

relative cross-linking density value was calculated using E_{Mc} from Table 7.3 and Equation 6.1[23].The results of the calculations are plotted in Figure 7.8.

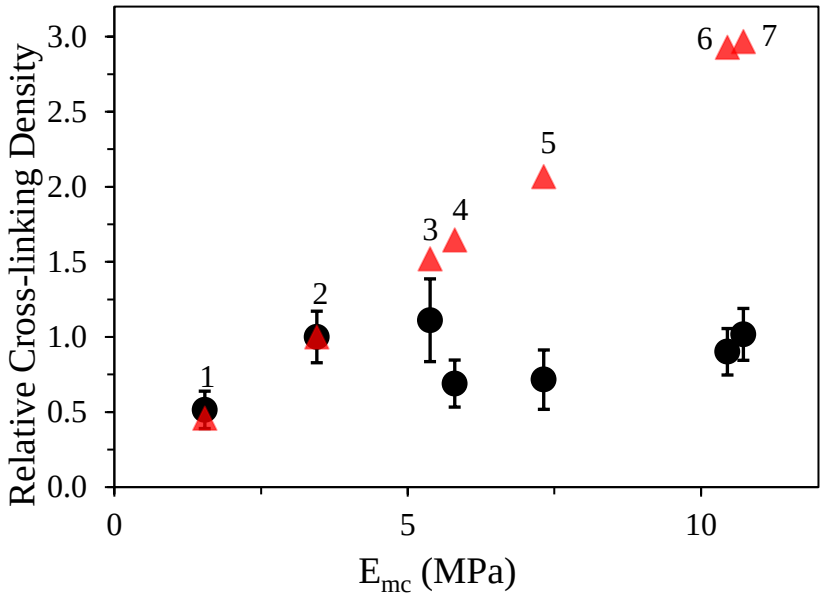

Figure 7.8: The graph of calculated values of relative cross-linking from DMA measurements (▲) and swelling data (●) vs E_{Mc}. The samples are signified from left to right as non-oriented (1), neat epoxy (2), oriented (3), SiCW-OH (4), SiCW-PAA (5), SiCW-P2VP (6), and SiCW-EP (7).

Figure 7.8 demonstrates the comparison of the swelling data to cross-linking density calculated from DMA results. The results show a certain mismatch in the mechanical and swelling cross-linking density estimations for the composites. The linear trend that follows the DMA data does not match the cross-linking density values obtained from the swelling experiment. The linear increase in DMA cross-linking data is caused by the distributed elastic stresses at the interfaces in the composites. The swelling data show that the cross-linking density of the matrix is approximately the same for all the composites. Thus, we suppose that the cross-linking density, for all the samples reported

in this chapter, is approximately the same as the neat epoxy. It appears that the most efficient stress transfer through interface at the temperatures above T_g restricting mobility of epoxy network is occurring in SiCW-P2VP and SiCW-Ep composites.

7.4: Conclusions

The following conclusions can be made from the study reported in Chapter 7:

- In terms of epoxy curing kinetics, the addition of SiCW-PAA to the epoxy resin decreases the activation energy of the curing, similar to the MagSiCWs.
- The other whiskers studied did not significantly change the E_a, when compared to the neat epoxy resin.
- The highest rate of epoxy polymerization reaction was observed for the unmodified (cleaned) SiCW-OH possessing hydroxyl groups on their surface. The curing process of the epoxy in the presence of the whiskers is characterized by the highest value of the pre-exponential factor in the Arrhenius equation.
- The IR spectroscopy results indicated that the chemical pathways for the epoxy resin curing are affected by the whiskers addition. Specifically, there is an accelerated consumption of DDSA hardener in the presence of the filler.
- The DMA results showed an increase in storage modulus at room temperature of ~60% for all composites in comparison with the neat epoxy material. These results indicated that all types of modified whiskers have good and quite similar adhesion to the matrix, which results in an effective stress transfer from the matrix to the filler.
- As the temperature of measurements increased, more differences in the modulus of the composite materials were observed. The highest value of T_g was found for SiCW-

Ep, while the lowest T_g was observed for the unmodified clean whiskers. In general, the T_g determined in DMA measurements for the composites was higher than that of the neat epoxy.

- The T_g values determined from the DSC measurements were the highest for SiCW-Ep. The lowest T_g was demonstrated by epoxy filled with SiCW-PAA. However, T_gs for the composite materials are within ±5 degrees of that of pure epoxy.
- Significant residual stresses were present in the neat epoxy material and in the nanocomposites, as indicated by the presence of the enthalpic relaxation. The stresses can be readily alleviated via thermal annealing and controlled cooling.
- The microstructure of the composites was found to be quite similar, with the exception of the composite containing SiCW-P2VP. The SiCW-P2VP composite had the highest level of packing and the lowest amount of agglomerates.
- The SiCW-P2VP's superior dispersibility did not translate to enhancement in the mechanical characteristics of the composite materials below T_g.
- This study indicated that the surface modification of the SiCW, in many aspects, significantly influences the formation and properties of the SiCW/epoxy composite materials.
- These results were used to identify the MagNP interphase on the MagSiCW as a problematic region within the MagSiCW/epoxy nanocomposite materials.

7.5: References

1. Yuan, Z. K.; Yu, J. H.; Rao, B. L.; Bai, H.; Jiang, N.; Gao, J.; Lu, S. R., Enhanced thermal properties of epoxy composites by using hyperbranched aromatic polyamide grafted silicon carbide whiskers. *Macromol Res* **2014,** *22* (4), 405-411.

2. Jancar, J.; Douglas, J. F.; Starr, F. W.; Kumar, S. K.; Cassagnau, P.; Lesser, A. J.; Sternstein, S. S.; Buehler, M. J., Current issues in research on structure-property relationships in polymer nanocomposites. *Polymer* **2010,** *51* (15), 3321-3343.

3. Winey, K. I.; Vaia, R. A., Polymer nanocomposites. *Mrs Bull* **2007,** *32* (4), 314-319.

4. Schmidt, G.; Malwitz, M. M., Properties of polymer-nanoparticle composites. *Curr Opin Colloid In* **2003,** *8* (1), 103-108.

5. Balazs, A. C.; Emrick, T.; Russell, T. P., Nanoparticle polymer composites: where two small worlds meet. *Science* **2006,** *314* (5802), 1107-10.

6. Putz, K. W.; Palmeri, M. J.; Cohn, R. B.; Andrews, R.; Brinson, L. C., Effect of cross-link density on interphase creation in polymer nanocomposites. *Macromolecules* **2008,** *41*, 6752-6756.

7. Lu, H. B.; Nutt, S., Restricted relaxation in polymer nanocomposites near the glass transition. *Macromolecules* **2003,** *36*, 4010-4016.

8. Rittigstein, P.; Torkelson, J. M., Polymer-nanoparticle interfacial interactions in polymer nanocomposites: Confinement effects on glass transition temperature and suppression of physical aging. *J Polym Sci Pol Phys* **2006,** *44* (20), 2935-2943.

9. Plueddemann, E. P., *Interfaces in polymer matrix composites,*. Composite materials, Academic Press: New York, 1974; Vol. 6, p 294.

10. Chawla, K. K., *Composite materials: Sceince and engineering*. 3rd ed.; Springer Science: 2012.

11. Tiwari, A.; Hihara, L. H. Nanoparticulate-enhanced coatings. US20120251807 A1, 2012.

12. Dawes, S. B.; Stempin, J. L.; Wexell, D. R. Multicomponent ceramic matrix composites. US5153152 A, 1992.

13. Han, S.; Chung, D. D. L., Strengthening and stiffening carbon fiber epoxy composites by halloysite nanotubes, carbon nanotubes and silicon carbide whiskers. *Appl Clay Sci* **2013,** *83-84* (83-84), 375-382.

14. Wang, W. X.; Takao, Y.; Matsubara, T.; Kim, H. S., Improvement of the interlaminar fracture toughness of composite laminates by whisker reinforced interlamination. *Composites Science and Technology* **2002,** *62* (6), 767-774.

15. Zhou, Y. X.; Hosur, M.; Jeelani, S.; Mallick, P. K., Fabrication and characterization of carbon fiber reinforced clay/epoxy composite. *J Mater Sci* **2012,** *47* (12), 5002-5012.

16. Luzinov, I.; Julthongpiput, D.; Tsukruk, V. V., Thermoplastic elastomer monolayers grafted to a functionalized silicon surface. *Macromolecules* **2000,** *33* (20), 7629-7638.

17. Luzinov, I.; Julthongpiput, D.; Malz, H.; Pionteck, J.; Tsukruk, V. V., Polystyrene layers grafted to epoxy-modified silicon surfaces. *Macromolecules* **2000,** *33* (3), 1043-1048.

18. Luzinov, I.; Julthongpiput, D.; Liebmann-Vinson, A.; Cregger, T.; Foster, M. D.; Tsukruk, V. V., Epoxy-terminated self-assembled monolayers: Molecular glues for polymer layers. *Langmuir* **2000,** *16* (2), 504-516.

19. Tsyalkovsky, V.; Klep, V.; Ramaratnam, K.; Lupitskyy, R.; Minko, S.; Luzinov, I., Fluorescent reactive core-shell composite nanoparticles with a high surface concentration of epoxy functionalities. *Chem Mater* **2008,** *20* (1), 317-325.

20. Tsyalkovsky, V.; Burtovyy, R.; Klep, V.; Lupitskyy, R.; Motornov, M.; Minko, S.; Luzinov, I., Fluorescent nanoparticles stabilized by poly(ethylene glycol) containing

shell for pH-triggered tunable aggregation in aqueous environment. *Langmuir* **2010,** *26* (13), 10684-92.

21. Zhou, X.; Goh, S. H.; Lee, S. Y.; Tan, K. L., XPS and FTIR studies of interactions in poly(carboxylic acid)/poly(vinylpyridine) complexes. *Polymer* **1989,** *39* (16), 3631-3640.

22. Harsch, M.; Karger-Kocsis, J.; Holst, M., Influence of fillers and additives on the cure kinetics of an epoxy/anhydride resin. *Eur Polym J* **2007,** *43* (4), 1168-1178.

23. Chen, J.-S.; Obera, C. K.; Poliks, M. D.; Zhang, Y.; Wiesner, U.; Cohenc, C., Controlled degradation of epoxy networks: analysis of crosslink density and glass transition temperature changes in thermally reworkable thermosets. *Polymer* **2004,** *45*, 1939-1950.

24. Jung, J. C.; Lee, S. K.; Lee, K. S.; Choi, K. Y., Chain-length effect of alkenyl succinic anhydride on thermal and mechanical-properties of the cured epoxy-resins. *Angewandte Makromolekulare Chemie* **1991,** *185*, 129-136.

25. Kolar, F.; Svitilova, J., Kinetics and mechanism of curing epoxy/anhydride systems. *Acta Geodyn Geomater* **2007,** *4* (3), 85-92.

CHAPTER EIGHT

THE REINFORCEMENT OF MagSiCWs

8.1: Introduction

The study reported in Chapter 7 resulted in the understanding that stress transfer at the MagSiCW-epoxy interface was not optimized. Specifically, the magnetic nanoparticle layer deposited on the surface of SiCWs causes a reduction in the modulus and T_g of the composite material in comparison to the composite incorporating whiskers without the nanoparticles. Hence, in order to enhance the mechanical properties of the material, a reinforcement of the magnetic interphase was explored aiming to create a higher level of shear stress transfer through matrix-whisker boundary[1]. To this end, we envisioned that an additional polymer encapsulation of the "fluffy" MagNPs layer would alleviate the interfacial weaknesses. In fact, pre-impregnation is often used on macroscale composites to ensure good wetting and infusion of complex fibrous materials with polymers[2]. In our case, the "fluffy" layer of magnetic nanoparticles can be considered a complex "fractal-like" structure, which is necessary to infiltrate with polymer to reinforce the interfacial structure. Specifically, the MagNPs layer requires a polymer with binding groups capable of covalently reacting with carboxylic acid groups of PAA covering the nanoparticles. Hence, for this purpose, we selected PGMA, which has the epoxy functional groups able to react with a plethora of different groups to create a covalently bound network[3-6]. As such, it was thought to be an efficient reinforcing agent.

The melt state "grafting to" method, a well-known and easily applied methodology for the application of PGMA to many different surfaces, was selected for

the PGMA anchoring[3]. The bulk state melt grafting would allow for highly dense packing of the macromolecules onto the surface. However, there is possible drawback, since the fillers could be "welded" together or create excessive bridging, as seen in Chapter 3 with the bridging of SiCWs with PGMA.

8.2: Experimental

8.2.1: Surface Modification of MagSiCWs with PGMA

The MagSiCWs were dispersed into methanol at 1.3 wt. %. Then, they were added dropwise to a sonicated 5 wt. % solution of PGMA in MEK. The resulting solution was roto-evaporated under nitrogen flow for 2.5 hours creating a composite film of MagSiCWs dispersed in PGMA. Then, the film was heated to 120 ^{o}C for 1 hour under nitrogen. The MagSiCWs were then redispersed in methanol and cleaned twice by magnetic separating, decanting and redispersing in a fresh portion of methanol. Figure 8.1 is a schematic representation of the methodology used to modify the MagSiCWs' surface with the PGMA (PGMA-MagSiCW).

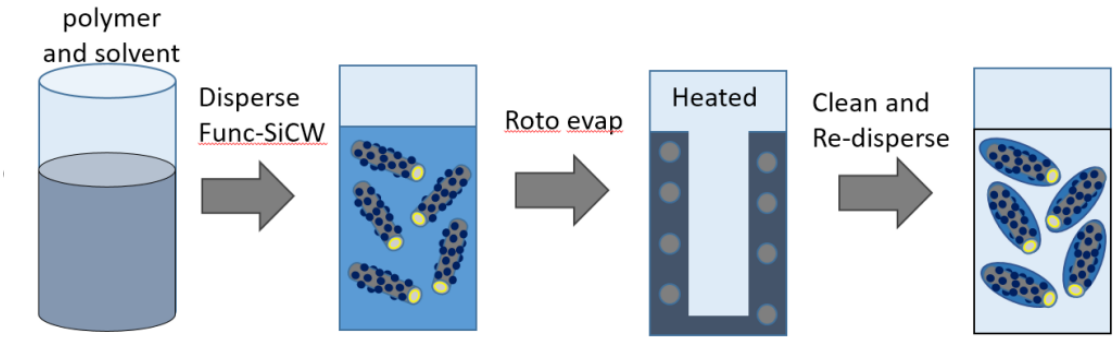

Figure 8.1: Schematic of methodology used for the surface modification of MagSiCWs with PGMA.

8.2.2: TGA Measurements

The PGMA-MagSiCWs samples (3-5 mg) were purged with dry air for 10 min. Then, they were heated in an air environment up to 600 ^{o}C at 20 ^{o}C/min.

8.2.3: Fabrication of Epoxy Composites

As reported in Chapters 6 and 7, the PGMA-MagSiCWs were dispersed in methanol and mixed with epoxy resin. After methanol was evaporated from the mixture, the hardener and catalyst were added. The epoxy:hardener:catalyst volume ratio was 1:1.37:0.07. To prepare the composite sample, the epoxy matrix/whiskers mixture was casted into a Teflon mold. The mixture was cured at room temperature for 48 hours, and then at 75 ^{o}C for 24 hours. According to DSC data, the time-temperature conditions were sufficient to fully cure the polymer matrix. The volume fraction of whiskers in the matrix was approximately 3 vol. %.

8.2.4: DMA Measurements

Tensile DMA testing was run at 2 ^{o}C/min from -20 ^{o}C to 150 ^{o}C using frequencies of 1, 2, and 5 Hz and applying 5 μm amplitude of oscillation. Each of the samples had approximately the same length, width, and thickness of 8.0 mm, 5.0 mm, and 0.34 mm.

8.2.5: DSC Measurements

The DSC measurements were conducted for samples of 3–5 mg. The DSC was run from -20 ^{o}C to 150 ^{o}C at the heating rate of 15 ^{o}C/min. Then, the sample was cooled down back to -20 ^{o}C at 15 ^{o}C/min and then heated for a second time up to 150 ^{o}C a at 15 ^{o}C/min.

8.2.6: SEM Imaging

The composite sample was immersed in liquid nitrogen and broken in longitudinal direction. Then, using carbon tape, the composite was attached to the face of an SEM disk propped up to see the longitudinal cross-section.

8.3: Results and Discussion

8.3.1: Identification of the Interphase

The interphase of the composite was thought to be a "fluffy" lower modulus region. Thus, the identified mechanically weak region in the composite is assigned to be the MagNP layer modifying the surface of the SiCWs (Figure 8.2). This weak interfacial

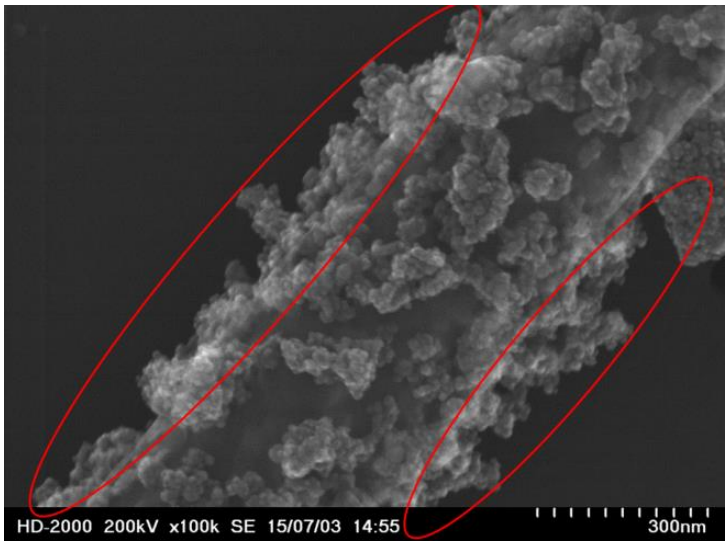

Figure 8.2: SEM image of the 1:5 MagSiCW with the magnetic layer (circled in red) identified as the low-stress transfer region.

region does not provide the optimal structure for stress transfer within the epoxy composite materials. Thus, the proposed reinforcement would create a more elastically efficient interphase within the composite. Hence, the melt state "grafting to" of PGMA was used to cement the attached MagNP layer to the SiCWs' surface.

8.3.2: Reinforcement of the MagSiCWs' Interphases

The morphology and structure of the PGMA-MagSiCWs were first studied using TEM (Figure 8.3).

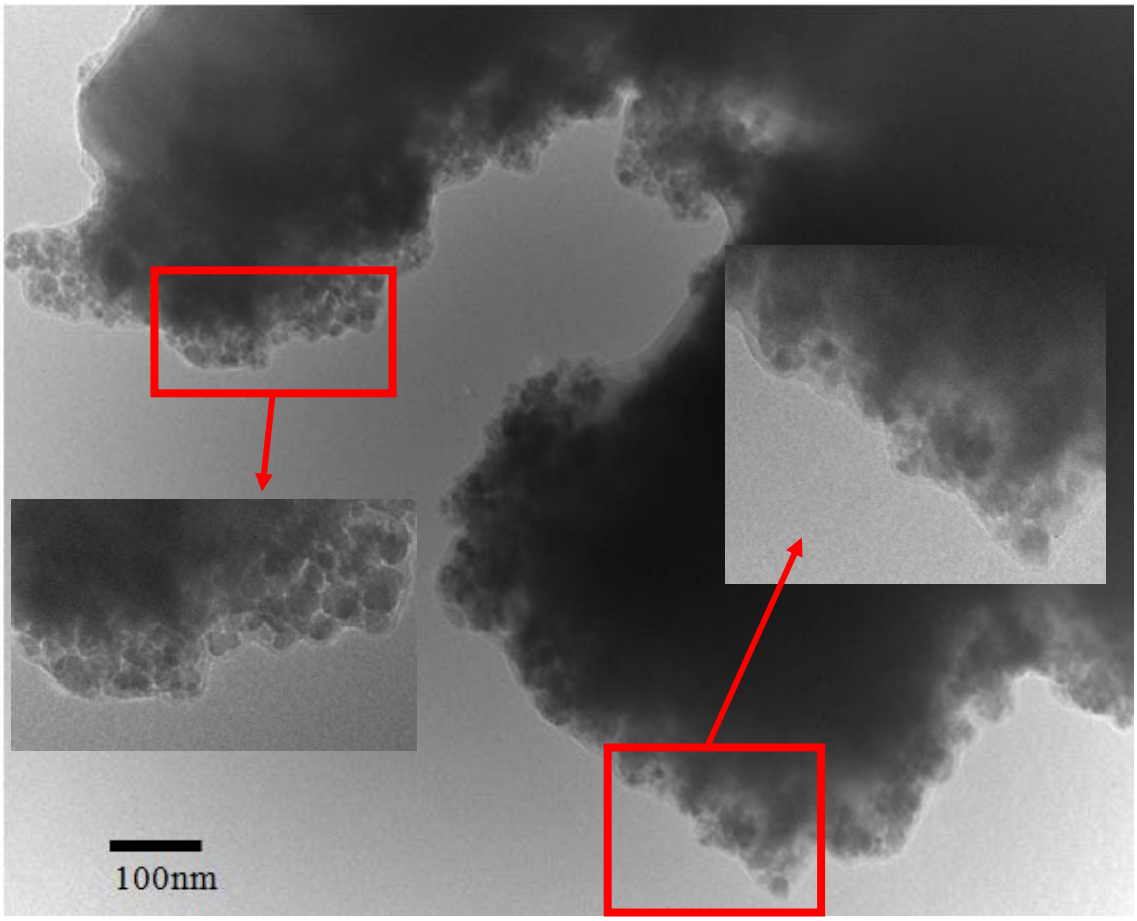

Figure 8.3: TEM image of the PGMA-MagSiCWs. (The red squares are the zoomed-in regions of the image).

A PGMA material can be clearly seen encapsulating the attached MagNPs. The film appears to be uniform along the surface, modifying the surface and the space between the nanoparticulates. However, it was difficult to evaluate the amount of PGMA anchored from the TEM images. Thus, TGA was used to determine the amount of the polymer anchored to the MagSiCWs (Figure 8.4). At 500 ^{o}C, the sample's weight

decreased by 24.4 %. Using Equation 3.5 and comparing the results to the already present polymer on the surface (8.0 wt. %), the thickness of the PGMA layer was calculated to be ~90 nm. This does not correlate well with the image analysis. We suggested that the excessive amount of PGMA is due to the bridging between SiCWs, which was also observed for the modification of bare SiCWs (Chapter 3) and/or impregnation of the ~100 nm MagNP surface layer. However, the PGMA-MagSiCWs were found to be magnetic and modified with the PGMA layer. Therefore, they were determined to be suitable of fabrication of the composite material.

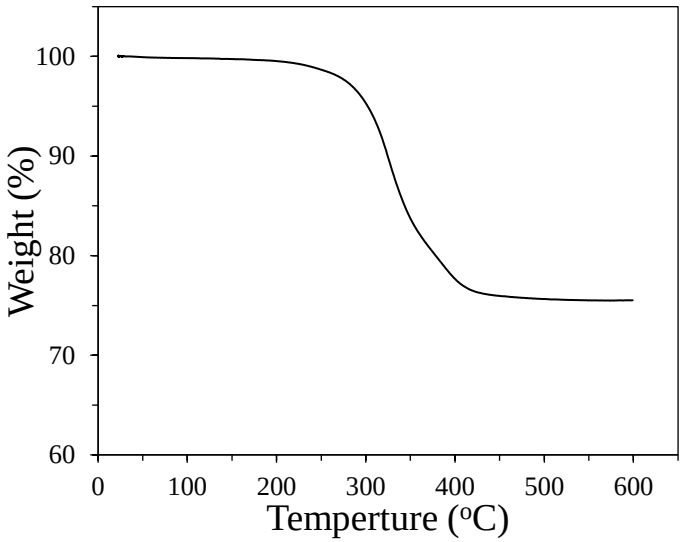

Figure 8.4: TGA curve of the MagSiCW modified with PGMA.

8.3.3: DMA Study of PGMA-MagSiCW/Epoxy Composites

The DMA testing was foreseen as a technique that could directly reveal the interfacial improvement of the MagSiCWs. In comparison to the neat epoxy, the MagSiCWs' epoxy composite without orientation had a higher modulus but a reduced T_g (Chapter 6). Thus, the enhancement of these properties would determine whether the

interphase improvement was achieved with the PGMA grafting. The PGMA-MagSiCWs were mixed with the epoxy resin and cured (no magnetic orientation was applied). Figure 8.5 demonstrates the thermo-mechanical properties of the obtained PGMA-MagSiCW epoxy composites in comparison to the neat epoxy and the non-oriented MagSiCWs epoxy composites.

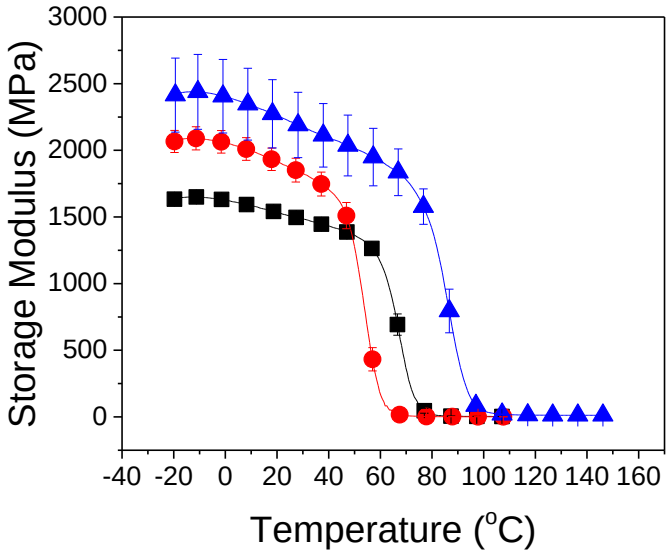

Figure 8.5: The temperature dependence of the storage modulus results for the PGMA-MagSiCW epoxy composites (▲), non-oriented MagSiCWs epoxy composite (●), and neat epoxy (■).

The DMA results are summarized in Table 8.1. The data indicate that the room temperature storage modulus for the PGMA-MagSiCWs/epoxy composite is ~20 % higher than that for the MagSiCW/epoxy material, 46 % greater than that for the neat epoxy and within a standard deviation of the other materials containing non-oriented SiCWs (Chapter 7). Additionally, the thermal properties have improved dramatically. The DMA T_g increased by 30°C comparing with the former MagSiCW, by 20°C

comparing with the neat epoxy, and it was approximately 10–20^{o}C higher than that for the other composites containing SiCWs.

Table 8.1: Thermo-mechanical properties of the PGMA-MagSiCW/epoxy composite compared with the neat epoxy and MagSiCWs non-oriented composite.

Sample	E' (@RT) (MPa)	E" Peak (MPa)	Peak Temp. (^{o}C)	Tan δ Peak (MPa)	Peak Temp. (^{o}C)
Neat Epoxy	1521	189	69	2.01	77
MagSiCW-No Orientation	1868	242	55	2.53	67
PGMA-MagSiCWs	2226	243	89	1.15	99

Table 8.1 shows that the peak temperatures of E" and tan δ of PGMA-MagSiCWs material are greater than those of the other samples. At the same time, the peak value of tan δ is much lower than that for the other materials. These results indicated an efficient stress transfer in the composite. The transfer appears to be better than the one in all the other composite samples except for the SiCW-Ep (1.14 MPa). The enhanced composite properties show that the reinforcement of the interfacial region can be done with PGMA, improving the thermo-mechanical properties of the composite material.

8.3.4: DSC Study of PGMA-MagSiCW/Epoxy Composites

The composite samples were investigated using DSC to identify the T_g of the materials in static conditions. Figure 8.6a and Table 8.2 shows T_g for the composites containing MagSiCWs and PGMA-MagSiCW along with the neat epoxy. The T_g of the PGMA-MagSiCW/epoxy composite was the highest (79.3 ^{o}C) with clear presence of enthalpic relaxation. The level of enthalpic relaxation observed for the PGMA reinforced whiskers was less prominent than that for the other presented samples.

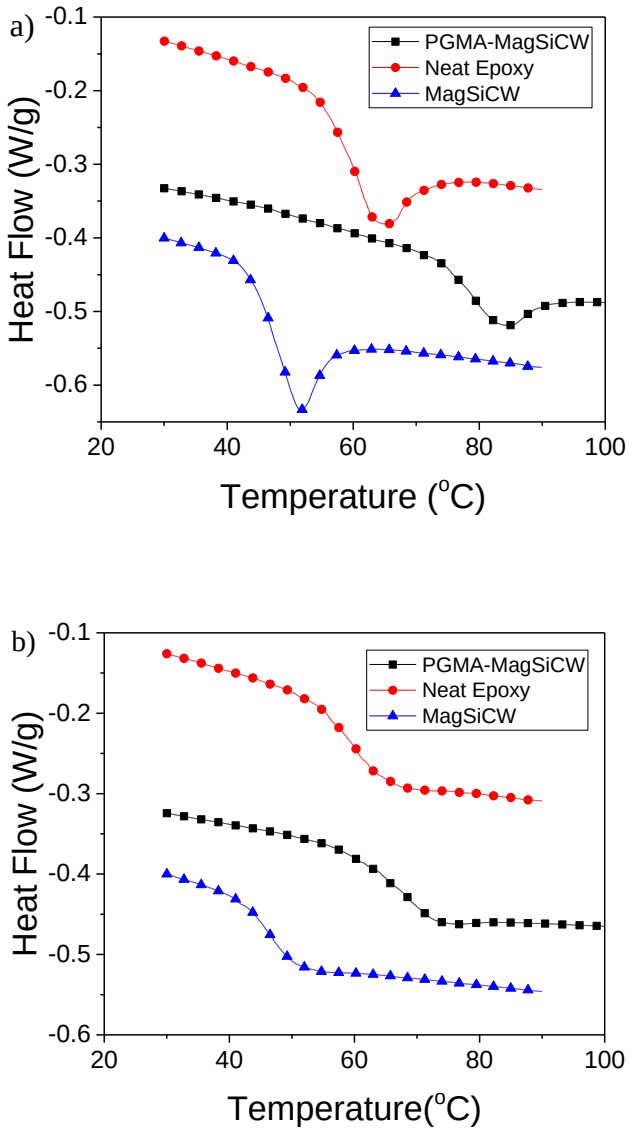

Figure 8.6: The DSC curves for the PGMA-MagSiCW/epoxy composite, MagSiCW/epoxy composite, and the neat epoxy samples: (a) first run and (b) second run.

Table 8.2: The selected thermal properties of the materials studied.

Sample	Tg-h1 (°C)	Tg-h2 (°C)
Neat Epoxy	63.3	59.5
Non-oriented SiCWs	50.4	47.0
PGMA-MagSiCWs	79.3	65.6

The newly fabricated material have improved thermal properties in comparison to the other composites and the neat epoxy. As the only parameter changing was the PGMA modification, the increased T_g could only be attributed to increases in the local cross-linking density of the epoxy bulk. In addition, the PGMA-reinforcing layer cemented the fluffy MagNP layer on the surface of the SiCWs, creating a greater rigidity of the interphase, which was manifested through the DMA measurements shown in Section 8.2.3.

8.3.5: Nanocomposites' Microstructure

The composite microstructure of the PGMA-MagSiCW/epoxy nanocomposite was observed with SEM (Figure 8.7). The imaged microstructures showed randomly oriented and evenly dispersed whiskers within the epoxy matrix. The PGMA-MagSiCWs were manually analyzed using Gwydion software using four images from three different samples to obtain the dispersity, concentration of aggregates per unit area, and the size of the aggregates (Table 8.3).

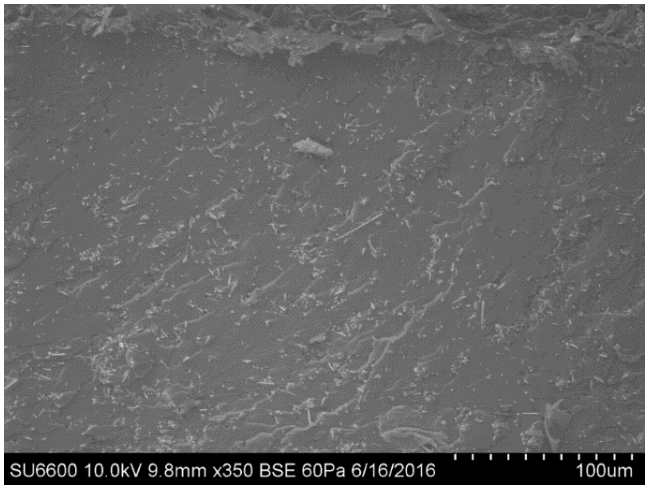

Figure 8.7: SEM image of the cross-section of the PGMA-MagSiCW/epoxy composite.

Table 8.3: Summary of the SEM image analysis.

Summary	Distance between fillers (μm)	# of agg./mm^2	Length of agg. (μm)	Width of agg. (μm)
Non-oriented MagSiCWs	10.9 ± 5.9	80 ± 3.0	10.6 ± 3.6	5.2 ± 3.6
PGMA-MagSiCWs	11.1 ± 7.7	247 ± 47	10.3 ± 3.1	4.8 ± 1.7

Table 8.3 shows that the dispersity of the components went down as the reinforced sample had significantly more aggregates. Specifically, the PGMA-MagSiCW/epoxy composite has the highest number of agglomerates per unit area of any of the composite materials prepared in this work. However, this did not significantly hinder the composite's properties. These results also show the aggregates were of low aspect ratio, ~2. Thus, we suggest that the aggregates originated from the bridging between the whiskers as a result of PGMA grafting. However, the concentration of aggregates was under the critical number for hindering the improvement in composite properties. Another result of the microstructure analysis was that there was no orientation in the composite film. The orientation of the PGMA-MagSiCWs in the composite was manually measured using Gwyddion. The results are shown in Figure 8.8.

The random distribution is similar to the previously studied non-oriented MagSiCW/epoxy composite materials. Thus, the composites have the same microstructure allowing for a direct comparison of properties.

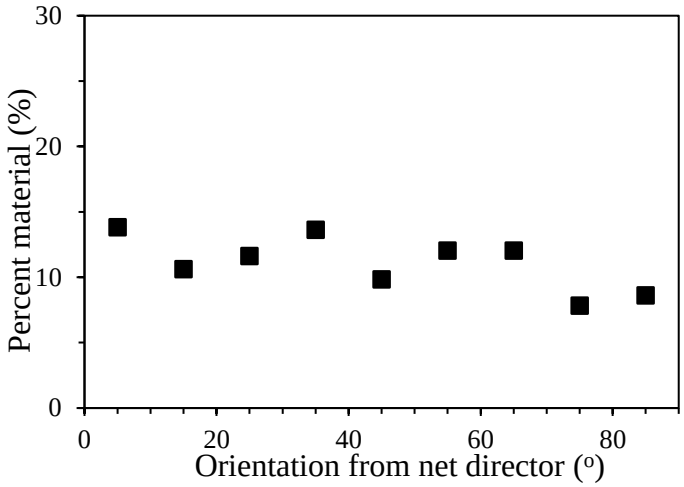

Figure 8.8: Histogram of the PGMA-MagSiCW fillers orientation in the epoxy matrix.

8.4: Conclusions

The following conclusions can be made as a result of the study reported in Chapter 8:

- The macromolecule reinforcement of the composite interfacial structure improved thermal and thermo-mechanical properties of the composite by structurally cementing the magnetic particulates on the surface of the SiCWs.
- The obtained composite had increased T_g and the modulus in comparison to its counterpart composite (with MagSiCWs) and the neat epoxy.
- The microstructure of the composite materials showed a higher concentration of agglomerates with a lower packing density of the dispersed filler along with a completely random distribution.
- The composite material containing PGMA-MagSiCWs increased thermal and mechanical properties indicated that the application of PGMA created a densely packed interphase with a greatly increased rigidity and cross-linking density.

8.5: References

1. Plueddemann, E. P., *Interfaces in polymer matrix composites,*. Composite materials, Academic Press: New York, 1974; Vol. 6, p 294.

2. Chawla, K. K., *Composite materials: Science and engineering*. 3rd ed.; Springer Science: New York, 2013.

3. Zdyrko, B.; Klep, V.; Luzinov, I., Synthesis and surface morphology of high-density poly(ethylene glycol) grafted layers. *Langmuir* **2003,** *19* (24), 10179-10187.

4. Yu, W. H.; Kang, E. T.; Neoh, K. G., Controlled grafting of well-defined epoxide polymers on hydrogen-terminated silicon substrates by surface-initiated ATRP at ambient temperature. *Langmuir* **2004,** *20* (19), 8294-8300.

5. Draper, J.; Luzinov, I.; Minko, S.; Tokarev, I.; Stamm, M., Mixed polymer brushes by sequential polymer addition: anchoring layer effect. *Langmuir* **2004,** *20* (10), 4064-4075.

6. Edmondson, S.; Huck, W. T. S., Controlled growth and subsequent chemical modification of poly(glycidyl methacrylate) brushes on silicon wafers. *J Mater Chem* **2004,** *14* (4), 730-734.

CHAPTER NINE

CONCLUSIONS

This chapter is devoted to concluding the body of work presented in this dissertation. The study of SiCW/epoxy composite materials resulted in a number of observations about the nanocomposites fabrication, their structure and properties. The following major conclusions can be drawn:

- The fabrication of magnetically active SiC whiskers is possible using polymer-to-polymer complexation of absorbed PAA and grafted P2VP at the interfaces of iron oxide nanoparticles and SiC whiskers, respectively.
- The magnetically active SiC whiskers can be effectively oriented within a curing epoxy matrix.
- The addition of the whiskers with and without orientation can dramatically improve the composite materials' properties. Additionally, the orientation of the whiskers has a significant positive effect on the composites' T_g.
- The magnetic layer was identified as a "fluffy" region negatively influencing the mechanical and thermal properties of the composite materials.
- The "fluffy" magnetic layer attached to the SiC whiskers can be structurally reinforced by the addition of PGMA utilizing the melt state "grafting to" technique.
- The reinforcement of the "fluffy" magnetic layer resulted in the further improvement of the nanocomposite's properties.

CHAPTER TEN

FUTURE WORK

Although, this body of work established a methodology for the fabrication of magnetically oriented SiCW/epoxy composite materials, there are still related scientific/engineering aspects that were not addressed and might be the subjects of the future work. Some of them are listed below:

- Preparation of SiCWs modified with monolayer of magnetic nanoparticles. Such modification could potentially reduce or eliminate the "fluffiness" of the interfacial region leading to the boost in mechanical and thermal properties. The experimental effort related to this aspect would involve:
    - wet synthesis of magnetic nanoparticles of a desired size;
    - study of surface modification of the nanoparticle with PAA of different molecular weights aiming to produce individually modified particles, but not aggregates;
    - development of an experimental procedure for the attachment of the particles to P2VP modified SiCWs with minimal inter-whisker bridging and particle multilayer formation.
- Fabrication of the newly prepared whisker/epoxy composites (with and without orientation) utilizing the methodologies developed in this work and studying their thermal and thermo-mechanical
- Study the dynamics of the orientation MagSiCW in epoxy resin and its dependence on the size and number of the nanoparticles comprising the magnetic monolayer;

- Fabrication and evaluation of properties of the composite materials with high volume fraction of the fillers including:
    - dynamics of the whiskers orientation in the situation of increasing whisker-whisker interaction at high loads;
    - influence of whiskers' surface chemistry on epoxy curing and evolution of epoxy matrix's properties at high concentration of the fillers;
    - relevancy of the theoretical models used for calculation of the mechanical properties of composite materials with directionally aligned nanofillers.
- Fabrication and evaluation of properties of multilayered composite materials with the filler oriented at different angle in each layer.

APPENDIX

MATERIALS AND INSTRUMENTATION

3.1: Materials

3.1.1: Nanoparticles

Absolute Ethyl Alcohol (99.5%):

Company Identification: Acros, Inc

CAS Number: 64-17-5

Nickel (III) Chloride Hexahydrate:

Company Identification: Acros, Inc

CAS Number: 1310-58-3

Potassium Hydroxide [KOH]:

Company Identification: EMD Millipore

CAS Number: 1310-58-3

Hydrazine Hydrate (78-82%) (iodometric):

Company Identification: Sigma Aldrich

CAS Number: 10217-52-4

Iron oxide nanoparticles (99.5%):

Company Identification: US Research Nanomaterials Inc.

CAS Number: 1317-61-9

3.1.2: Whiskers

Silicon Carbide Whiskers:

Company Identification: Advanced Composite Materials, LLC.

Component Identification: Silar SC-9M

3.1.3: Surface Modification

Silicon Wafer:

Company Identification: University Wafer

Component Identification: silicon crystal <100> 725-850nm (oxide layer)

Identification number: 1978

The wafers were used to study surface modification.

Hydrogen peroxide [H2O2]:

Company Identification: Acros Organics.

Component Identification: Hydrogen Peroxide (30% in Water) (Without Stabilizer), Reagent ACS.

CAS Number: 7722-84-1

Sulfuric acid 98% [H2SO4]:

Company Identification: Acros Organics.

Component Identification: Sulfuric Acid, Reagent ACS

CAS Number: 7664-93-9

Toluene:

Company Identification: Acros Organics

Component Identification: Toluene, Reagent ACS

CAS Number: 108-88-3

Methyl ethyl ketone [MEK]:

Company Identification: Acros Organics

Component Identification: 2-Butanone, 99+%

CAS Number: 78-93-3

Acetone:

Company Identification: VWR International LLC

Component Identification: Acetone, ACS

CAS Number: 67-64-1

Methanol:

Company Identification: VWR International LLC

Component Identification: Methanol, ACS

CAS Number: 67-56-1

Polyglycidyl methacrylate [PGMA] (Structure 3.1):

The PGMA (M_n=100,000 g/mole, PDI~2.7) was synthesized by radical polymerization and purified by multiple precipitations in ether following the procedure described elsewhere[1, 2]. It was used as the initial modifier in the grafting process for the silicon wafers and nanoparticulates.

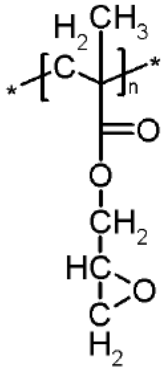

(S3.1)

(3-Glycideloxypropel)trimethoxysilane ≥98% [epoxy silane] (Structure 3.2):

(3-Glycideloxypropel)trimethoxysilane was ordered from Sigma Aldrich. It was dispersed in toluene and used for the initial polymer modification of model Si wafers and silicon carbide whiskers.

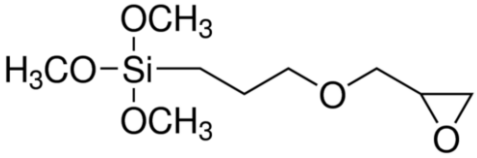

(S3.2)

Carboxy-terminated polyethylene glycol [PEG] (Structure 3.3):

Polyethylene glycol monomethyl ether (M_n=5000 g/mol) was obtained from Sigma-Aldrich and modified with succinic anhydride to form a carboxy-terminated derivative following procedure reported elsewhere [1]. The PEG molecule was used to study the polymer grafting to nickel model surfaces and nickel nanoparticles.

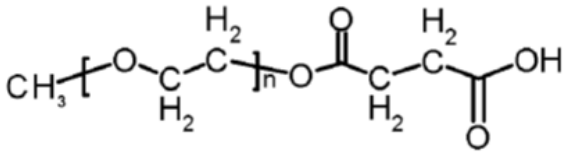

(S3.3)

Carboxy-terminated poly (2-vinyl pyridine) [P2VP] (Structure 3.4):

The carboxy-terminated poly (2-vinyl pyridine) (M_n=53000 g/mole, PDI=1.06) was purchased from Polymer Source Inc., Canada.

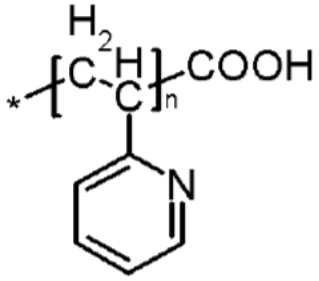

(S3.4)

Polyacrylic acid [PAA] (Structure 3.5):

The PAA (M_w=100,000g/mol) from Sigma-Aldrich was dispersed in water at 35 % and diluted with methanol to form a 2-5% solution of PAA in solution. This solution was

used for modification of model surfaces by dip-coating from solution and iron oxide nanoparticles by adsorption.

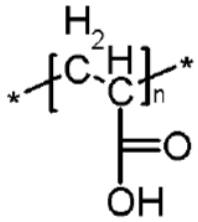

(S3.5)

3.1.4: Composite Fabrication

PEO (Structure 3.6):

Polyethylene oxide (M_n=1000000 g/mol) was obtained from Sigma-Aldrich.

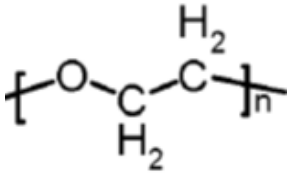

(S3.6)

Methanol:

Company Identification: VWR International LLC

Component Identity: Methanol, ACS

CAS Number: 67-56-1

Araldite 6005 epoxy resin:

Company Identification: Electron Mcroscopy Science (EMS).

Component Identification: 4-(1,1-Dimethylene) phenoxymethyl Ooxirane; Phenol, 4,4-(1-methylethylidene bis polymer with (chloromethyl) oxirane

CAS Number:3101-60-8

Dodecyl Succinic Anhydride [DDSA]:

Company Identification: Electron Microscopy Science (EMS).

Z-Benzyl dimethylamine [BDMA]:

Company Identification: Electron Microscopy Science (EMS).

Teflon plates:

Company Identification: Fluoro-Plastics

Size: 1" x 3" x 1/8"

Double Sided Scotch Tape:

Company Identification: Scotch tape

Size: ~1mm thickness

3.2: Instrumentation

3.2.1: Model Surface Morphology

Atomic Force Microscopy [AFM]:

Company Identification: Digital Instruments, Inc.

Component Identification: Dimension 3100 microscope

Ellipsometry:

Company Identification: InOmTech,Inc.

Component Identification: COMPEL automatic Ellipsometer (70° angle of incidence)

3.2.2: Nano-Particulates Morphology

Scanning Electron Microscopy [SEM]:

Company Identification: Hitachi

Component Identification: HD2000

Transmission Electron Microscopy [TEM]:

Company Identification: Hitachi

Component Identification: 7600

TEM Grids:

Company Identification: Electron Microscopy Science

Component Identification: FCF-200-Cu (Formvar carbon film on 200 mesh copper grids)

3.2.3: Composite Microstructure

Scanning Electron Microscopy [SEM]:

Company Identification: Hitachi

Component Identification: SU6600

3.2.4: Optical Characterization

Laser profilometer:

Company Identification: Olympus

Component Identification: LEXT

High Resolution Optical Microscopy:

Company Identification: Olympus

Component Identification: MVX10

3.2.5: Magnetic Characterization

Magnetometer:

Company Identification: Princeton Measurements Coperation

Component Identification: MicroMag Magnetometer

Model: 2900-02C

3.2.6: Thermo-Mechanical Characterization

Dynamic Mechanical Analysis [DMA]:

Company Identification: TA Instruments

Component Identification: DMA Q800

Set up: Tensile Testing

3.2.7: Thermal Characterization:

Differential Scanning Calorimeter:

Company Identification: TA Instruments

Component Identification: DSC Q1000

Thermal Gravimetric Analysis:

Company Identification: TA Instruments

Component Identification: TGA Q5000:

3.2.8: Chemical Characterization

IR Spectroscopy:

Company Identification: Nicolet

Component Identification: Magna-IR Spectrometer 550

REFERENCES:

1. B. Zdyrko, V. Klep, and I. Luzinov, *Synthesis and surface morphology of high-density poly(ethylene glycol) grafted layers.* Langmuir, 2003. **19**(24): p. 10179-10187.

2. B. Zdyrko, V. Klep, and I. Luzinov, *Macromolecular anchoring layers for polymer grafting: comparative study*. Polymer 2006, 2006. **47**(1): p. 272-279.